NTNU – Trondheim
Norwegian University of
Science and Technology

Effect of Plastic Deformation and Microstructure on Hydrogen Diffusion in Steel

Malin Sofie Berglund Hope

Preface

This report is the result of a Master's thesis project at the Norwegian University of Science and Technology, with specialization in materials. The experimental work in this thesis was executed from January to May 2015. Some of the equipment used for the experimental part of this thesis was produced between October and November 2014 as a part of my pre-master project. This pre-master project has provided a solid knowledge foundation for this thesis.

There are many people I would like to give my acknowledgements to. First of all, I would like to thank my main supervisor at NTNU, Prof. Afrooz Barnoush, for all the great help and support along the way. Prof. Roy Johnsen, my co-supervisor at NTNU, has also given great guidance throughout this work. Vigdis Olden, my supervisor from SINTEF and also the project lead in the ROP project, deserves a big thank you for giving me the opportunity to conduct this work.

My acknowledgements also goes to Bendik Simonsen. He has contributed a lot to this work by developing a software for the mathematical modelling of hydrogen diffusion, and allowing me to use it in my thesis to produce more and better results.

For help in the laboratory, there are a lot of people I want to thank. Nils-Inge Nilsen and Ann-Karin Kvernbråten have helped me find all the necessary equipment needed to execute the experimental work, and have also helped me in keeping it functioning through the whole testing period. Tarlan Hajilou has provided much needed help, especially in the SEM. The crew in the glassblower workshop have been vital for the production and maintenance of the glass parts of the equipment. Glass can easily break, which unfortunately was discovered during this work when parts of the equipment were shattered, but with their expertise and quick help the problem was fixed and the apparatus up and running again in no time. Børge Holen and the crew in the realization workshop have been a great help by cutting the test samples to correct size.

To the rest of my fellow students – your good humor and supportive words and actions has been a motivation boost through this whole period.

Trondheim, June 2015

Malin Sofie Berglund Hope

THE NORWEGIAN UNIVERSITY
OF SCIENCE AND TECHNOLOGY
DEPARTMENT OF ENGINEERING DESIGN
AND MATERIALS

MASTER THESIS SPRING 2015
FOR
STUD.TECHN. MALIN BERGLUND HOPE

Effect of plastic deformation and microstructure on hydrogen diffusion in steel

Within this project the candidate will use the experimental setup she developed during her project work to study the effect of different amounts of plastic deformation and different microstructures on hydrogen diffusivity in pipeline steels. Prior to this task the experimental setup should be calibrated by performing permeation tests on a simple ferritic Fe 3 wt.%Si samples. Tests will be performed at different temperatures and current transients will be used to calculate the diffusion coefficient. Once the experimental setup calibrated permeation tests will be performed on X65 pipeline steel with different percentage of cold working and simulated microstructure of the HAZ.

Relevant literature will be provided by the supervisors.

This project will be linked to the ROP research project financed by the Norwegian Research Council (NRF) executed by SINTEF.

Formal requirements:

Three weeks after start of the thesis work, an A3 sheet illustrating the work is to be handed in. A template for this presentation is available on the IPM's web site under the menu "Masteroppgave" (http://www.ntnu.no/ipm/masteroppgave). This sheet should be updated one week before the master's thesis is submitted.

Risk assessment of experimental activities shall always be performed. Experimental work defined in the problem description shall be planed and risk assessed up-front and within 3 weeks after receiving the problem text. Any specific experimental activities which are not properly covered by the general risk assessment shall be particularly assessed before performing the experimental work. Risk assessments should be signed by the supervisor and copies shall be included in the appendix of the thesis.
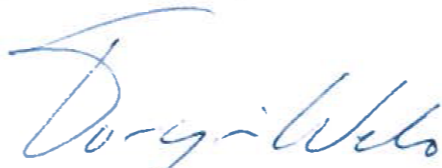
The thesis should include the signed problem text, and be written as a research report with summary both in English and Norwegian, conclusion, literature references, table of contents, etc. During preparation of the text, the candidate should make efforts to create a well arranged and well written report. To ease the evaluation of the thesis, it is important to cross-reference text, tables and figures. For evaluation of the work a thorough discussion of results is appreciated.

The thesis shall be submitted electronically via DAIM, NTNU's system for Digital Archiving and Submission of Master's theses.

Contact persons:
At the department: Afrooz Barnoush and Roy Johnsen
From the industry: Vigdis Olden, SINTEF

Torgeir Welo
Head of Division

Afrooz Barnoush
Professor/Supervisor

NTNU
Norges teknisk-
naturvitenskapelige universitet
Institutt for produktutvikling
og materialer

Summary

This work has been part of the ROP (Repair Contingency of Pipelines) project executed by SINTEF, where Vigdis Olden is project lead. The main content of this report is the execution of hydrogen permeation tests on Fe3wt.%Si and API X70 high strength steel.

The permeation tests were performed according to the ASTM Standard Practice for Evaluation of Hydrogen Uptake, Permeation, and Transport in Metals by an Electrochemical Technique [1], and the apparatus used for testing was designed and produced during a previous project work [2]. The tests were performed at temperatures of 30°C, 50°C and 75°C, and compared to previous results. The Fe3wt.%Si samples were tested as received, while the X70 steel samples were tested in the form of as received base metal (BM1), pre-strained base metal (BM2) and heat affected zone (HAZ1). BM1 and HAZ1 had 0% pre-strain, while BM2 had 1% pre-strain. The HAZ samples underwent heat treatment to obtain a coarse grain structure, which occur in the zone close to welds. All the samples were tested without palladium (Pd) coating on the anodic/exit side. The main analyzing methods utilized were the t_{lag} method as recommended by the ASTM standard [1], and also a more complex diffusion model including trapping parameters developed by Iino [3-5] by using a curve fitting software developed by Simonsen [6]. The latter one is referred to as the trapping model.

The trapping model gave higher values for the effective hydrogen diffusion coefficient, $D_{eff,}$ than the t_{lag} method. According to the trapping model, the D_{eff} for Fe3wt.%Si varied from $1,69 \cdot 10^{-10}$ to $1,75 \cdot 10^{-9}$ $m^2 s^{-1}$. For the X70 steel samples, the obtained D_{eff} values were higher. For X70 BM1, the D_{eff} according to the trapping model varied from $8,47 \cdot 10^{-10}$ to $4,77 \cdot 10^{-9}$ $m^2 s^{-1}$. For X70 HAZ1, D_{eff} varied from from $5,00 \cdot 10^{-10}$ to $3,39 \cdot 10^{-9}$ $m^2 s^{-1}$, while for X70 BM2 it varied from $8,21 \cdot 10^{-10}$ to $1,59 \cdot 10^{-9}$ $m^2 s^{-1}$. Fe3wt.%Si, X70 BM1 and X70 HAZ1 were tested at a temperature range of 30˚C-75˚C, while X70 BM2 was tested only at 30˚C.

Fe3wt.%Si showed a lower D_{eff} than all the X70 steel samples. According to microstructural investigations, this was an unexpected event. However, the theory that grain boundaries may act as fast paths for hydrogen diffusion presented in the literature may have been an explanation due to the smaller grains and many grain boundaries in the X70 steel compared to Fe3wt.%Si. X70 BM2 showed a higher diffusion coefficient than X70 BM1 at 30˚C, meaning the D_{eff} increased with increased pre-strain level in this thesis. This was not in accordance with previous results and literature. X70 HAZ1 showed a lower D_{eff} than X70 BM1, which was in accordance with previous results.

The sub-surface concentration C_0 was quite constant for the different materials, except for X70 HAZ1. For Fe3wt.%Si, X70 BM1 and X70 BM2, it varied from $1,89 \cdot 10^{-3}$ to $2,03 \cdot 10^{-2}$ *ppm W* based on the D_{eff} values from the trapping model. For X70 HAZ1, it varied from $9,12 \cdot 10^{-3}$ to

$2,45 \cdot 10^{-2}$ *ppm W*. This suggested that C_0 was unaffected by pre-strain level, but affected by the heat affected zone (HAZ) for X70 steel.

Fe3wt.%Si showed a higher density of reversible traps, N_r, and a lower reversible trap binding energy, E_b, than X70 steel in general. X70 BM1 showed a slightly higher N_r than HAZ1, which was not in accordance with previous results. E_b was slightly higher for X70 HAZ1 compared to BM1, which, on the contrary, was in accordance with previous results. E_b and N_r for Fe3wt.%Si were 17,56 *kJ mol^{-1}* and $2,12 \cdot 10^{22}$ *sites cm^{-3}*, respectively. For X70 BM1, E_b and N_r had values of 26,56 *kJ mol^{-1}* and $1,29 \cdot 10^{20}$ *sites cm^{-3}*, and for HAZ1 the obtained values were 28,12 *kJ mol^{-1}* and $1,15 \cdot 10^{20}$ *sites cm^{-3}*. X70 BM2 was only tested at 30˚C because of limited amount of time, meaning E_b and N_r could not be obtained.

When comparing to previous results, a lower steady state permeation current I_{ss} measured on the anodic side and charging transients less steep than Fick's curve was noticed for all or many of the tests executed in this thesis. These events were an indication of a surface controlled diffusion situation, which was suspected to have been the case in this thesis. Surface examinations of both the anodic/exit and cathodic/charging side of the samples after testing revealed a slight oxide layer formation, carbon contamination, pitting on the anodic side and also etching of the surface on the cathodic side.

Sammendrag

Dette arbeidet er utført som en del av prosjektet ROP (Repair Contingency of Pipelines) utført av SINTEF, hvor Vigdis Olden er prosjektleder. Hovedinnholdet i denne avhandlingen er hydrogendiffusjonsmålinger utført på Fe3wt.%Si og X70 stål.

Diffusjonsmålingene ble utført i henhold til den internasjonale standarden for hydrogendiffusjonsmålinger av ASTM [1], og utstyret som ble brukt i testingen ble designet og produsert i et tidligere prosjektarbeid [2]. Testene ble utført ved temperaturene 30˚C, 50˚C og 75˚C. Resultatene fra testene ble sammenlignet med tidligere resultater. Fe3wt.%Si-prøvene ble testet «as received» uten videre behandling annet enn overflatepreparering. Prøvene av X70 stål ble testet i form av «as received» base-metall (BM1), plastisk deformert base-metall (BM2) og varmepåvirket sone (heat affected zone, HAZ1). BM1 og HAZ1 var ikke plastisk deformert, mens BM2 var deformert til 1% tøyning. HAZ-prøvene gjennomgikk varmebehandling for å oppnå den grove kornstrukturen som finnes i nærheten av sveiser. Alle prøvene ble testet uten Pd-belegg på den anodiske/utgangs- siden. Hovedmetoden for analyse var t_{lag} metoden anbefalt i ASTM standarden [1], i tillegg til en mer kompleks modell hvor parametre for hydrogenfeller (traps) var inkludert. Denne modellen ble utviklet av Iino [3-5]. Analysen ble utført ved hjelp av en software for kurvetilpasning utviklet av Simonsen [6]. Sistnevnte metode vil videre bli referert til som trapping-modellen.

Trapping-modellen resulterte i en høyere effektiv diffusjonskoeffisient, D_{eff}, enn t_{lag} metoden. Trapping-modellen resulterte i D_{eff}-verdier på $1{,}69 \cdot 10^{-10}$ til $1{,}75 \cdot 10^{-9}$ $m^2\,s^{-1}$ for Fe3wt.%Si. Verdiene for D_{eff} funnet for X70 stål var høyere. For X70 BM1 lå D_{eff} på $8{,}47 \cdot 10^{-10}$ til $4{,}77 \cdot 10^{-9}$ $m^2\,s^{-1}$, for HAZ1 på $5{,}00 \cdot 10^{-10}$ til $3{,}39 \cdot 10^{-9}$ $m^2\,s^{-1}$ og for BM2 på $8{,}21 \cdot 10^{-10}$ til $1{,}59 \cdot 10^{-9}$ $m^2\,s^{-1}$. Både Fe3wt.%Si, X70 BM1 og X70 HAZ1 ble testet ved både 30˚C, 50˚C og 75˚C, mens X70 BM2 kun ble testet på 30˚C.

D_{eff} for Fe3wt.%Si var lavere enn D_{eff} for samtlige prøver av X70 stål. Med tanke på materialenes mikrostruktur var dette uventet. Imidlertid eksisterer det en teori om at hydrogendiffusjonen øker i korngrenser. Dette kan ha vært en sannsynlig forklaring, i og med at X70 stål har mindre korn og derfor mer korngrenser enn Fe3wt.%Si. D_{eff} for X70 BM2 var høyere enn for BM1 ved 30˚C, noe som betyr at D_{eff} økte med økende plastisk deformasjon. I forhold til tidligere rapporterte resultater var dette uventet. På den andre siden var D_{eff} for X70 BM1 høyere enn for HAZ1, noe som er i tråd med tidligere rapporterte resultater.

Den utregnede overflatekonsentrasjonen, C_0, varierte forholdsvis lite for de forskjellige materialene utenom for X70 HAZ1. For Fe3wt.%Si, X70 BM1 og X70 BM2 varierte C_0 fra $1{,}89 \cdot 10^{-3}$ til $2{,}03 \cdot 10^{-2}$ *ppm W* basert på D_{eff} fra trapping-modellen. For X70 HAZ1 varierte C_0

fra $9,12 \cdot 10^{-3}$ til $2,45 \cdot 10^{-2}$ *ppm W*. Dette betydde at C_0 ikke ble påvirket av plastisk deformasjon, men at den ble påvirket av den varmepåvirkede sonen (HAZ) for X70 stål.

Når det gjelder tettheten av reversible feller (traps), N_r, og deres bindingsenergi, E_b, viste det seg at N_r var høyere for Fe3wt.%Si enn for X70 stål, med lavere E_b. X70 BM1 hadde så vidt høyere N_r enn HAZ1, noe som var uventet i forhold til tidligere rapporterte resultater. E_b for fellene var høyere for X70 HAZ1 enn for BM1, noe som bekrefter tidligere resultater. E_b og N_r hadde verdiene 17,56 *kJ mol^{-1}* og $2,12 \cdot 10^{22}$ *sites cm^{-3}* for Fe3wt.%Si. For X70 BM1 lå verdiene for E_b og N_r på 26,56 *kJ mol^{-1}* og $1,29 \cdot 10^{20}$ *sites cm^{-3}*, mens de for HAZ1 lå på 28,12 *kJ mol^{-1}* og $1,15 \cdot 10^{20}$ *sites cm^{-3}*. X70 BM2 ble kun testet på 30˚C på grunn av begrenset tid, noe som førte til at E_b og N_r ikke kunne bli utregnet.

Ved sammenligninger med tidligere resultater ble det oppdaget at den stabile diffusjonsstrømmen I_{ss} målt på den anodiske siden var lavere i resultatene fra denne rapporten. Omtrent alle transienter var i tillegg mindre bratte enn Fick's kurve. Disse hendelsene indikerte at overflatefenomener muligens styrte diffusjonen. Undersøkelser av både den katodiske/lade-siden og anodiske/utgangs-siden siden av prøvebitene ble gjennomført. Oksidlag og karbonforurensing ble oppdaget, i tillegg til grop-korrosjon på den anodiske siden og etsing/materialfjerning på den katodiske siden.

Contents

Nomenclature

AF   Acicular ferrite
AIDE   Adsorption-induced dislocation emission
B   Bainite
BCC   Body centered cubic
BCT   Body centered tetragonal
BM   Base metal
CP   Cathodic protection
DP   Degenerated pearlite
EDS   Energy Dispersive Spectroscopy
FCC   Face centered cubic
FCT   Finish cooling temperature
FE   Finite element
H_2   Hydrogen molecule
H_2S   Hydrogen Sulphide
HAZ   Heat affected zone
HCP   Hexagonal close packed
HE   Hydrogen embrittlement
HEDE   Hydrogen enhanced decohesion
HELP   Hydrogen enhanced localized plasticity
HIC   Hydrogen induced cracking
HSC   Hydrogen stress cracking
OCP   Open circuit potential
OM   Optical microscope
PCTFE   PolyChloroTetraFluorEthene
Pd   Palladium
POM   PolyOxyMethylene
SCT   Start cooling tremperature
SEM   Scanning Electron Microscope
TMCP   Thermo mechanical control process
XPS   X-ray Photoelectron Spectroscopy

List of symbols

Wt.%	Weight percent
i_p	Protection current density [A m^{-2}]
i_{corr}	Corrosion current density [A m^{-2}]
E_p	Protection potential [V]
E_{corr}	Corrosion potential [V]
I_{ss}	Steady-state anodic current [A]
i_c	Cathodic current density [A m^{-2}]
J_{ss}	Steady-state flux [mol m^2 s^{-1}]
J(t)	Time-dependent flux [mol m^{-2} s^{-1}]
L	Sample thickness [m]
C	Concentration [ppm W]
C_0	Sub-surface concentration [ppm W]
D_{eff}	Effective diffusion coefficient [m^2 s^{-1}]
D_l	Lattice diffusion coefficient [m^2 s^{-1}]
t_{lag}	Time to reach 63% of the normalized permeation flux J(t)/J$_{ss}$ [s]
F	Faraday's constant (96485 C mol^{-1})
T	Absolute temperature [K]
R	Gas constant (8,314 J mol^{-1} K^{-1})
N_r, N	Number of reversible trapping sites [sites cm^{-3}]
Ni	Number of irreversible trapping sites [sites cm^{-3}]
E_b	Binding energy for reversible traps [kJ mol^{-1}]
E_l	Energy for lattice activation [kJ mol^{-1}]
$D_{eff,traps}$	Effective diffusion coefficient when reversible traps are present [m^2 s^{-1}]
k_r	Number of atoms captured in reversible traps in a volume ∂V in one second
p_r	Probability that a hydrogen atom gets released from a reversible trap in one second
θ_r	Fraction of occupied reversible traps
θ_i	Fraction of occupied irreversible traps
λ, μ, κ	Non-dimensional variables used to calculate trapping parameters
$\mathcal{E}_p$	Plastic strain [%]
N_T	Number of trapping sites [sites cm^{-3}]

Chapter 1

Introduction

As part of the ROP project conducted by SINTEF, this work mainly seeks to investigate some of the hydrogen diffusion properties in API X65 high strength steel, a material often used as subsea pipelines for the transportation of oil and gas in the industry today. The material that will be used in the experimental part of this work is API X70 high strength steel, as it resembles X65 steel and is assumed to show similar results. Prior to the testing of this material, the equipment will be calibrated by testing on a pure ferritic Fe3wt.%Si material.

Pipelines consisting of X65/X70 steel normally have a cladding or lining consisting of a corrosion resistant alloy on the inside. As there is no repair contingency available for pipelines like this today, one of the main goals with the ROP project is to build knowledge about subsea hyperbaric welding (welding at elevated pressures). In addition, understanding and being able to assess degradation mechanisms, is highly important.

Hydrogen diffusion and trapping in steel can lead to hydrogen embrittlement (HE), an occurring problem in the industry of subsea equipment. HE involves the material losing its ductility and obtaining a brittle behavior. When this happens, the material can experience sudden fractures below yield strength which is not accounted for [7, 8]. The mechanisms for this are not fully understood yet, which makes experimental testing in this area essential for establishing a knowledge basis.

Hydrogen atoms are soluble in steel, meaning they will diffuse through the metal lattice. When the hydrogen atoms diffuse through the metal lattice, they might get trapped before they diffuse their way through. Typical trapping locations are dislocations, inclusions, precipitate particles, grain boundaries and phase boundaries. A material with many traps will mean a material with high concentration of hydrogen atoms [1, 9, 10].

The number of traps is an important finding for FE-modelling of equipment, as the real behavior of the material will be better accounted for than if the hydrogen effect is not considered. Therefore, it is also important to investigate the correlation between plastic strain and number of traps, considering the plastic strain will affect the number of traps. As heat affected zones (HAZ) might also be present in both strained and un-strained components, this must also be taken account of when finding the correlation between plastic strain and number of traps. The plan is therefore to test samples both with and without pre-strain, and also heat treated samples both with and without pre-strain to simulate the coarse grains that will be present in the HAZ microstructure.

To investigate this, hydrogen permeation measurements will be performed throughout this work. When calibrating the equipment on the Fe3wt.%Si samples, further investigation of the effect of microstructure on hydrogen diffusion will be possible. The X70 steel has a much more complex microstructure than the ferritic Fe3wt.%Si samples.

New testing apparatus was designed during a previous project work [2] and produced with the possibility to run tests producing more reliable results by controlling the temperature and eliminating temperature variations better than with existing equipment.

Chapter 2

Theory

2.1   Hydrogen embrittlement (HE)

HE is a problem when it comes to offshore structures as it causes costly repairs and may also cause leakage of oil and gas. The fractures caused by this mechanism, which can happen below yield strength, are sudden and difficult to foresee as the material obtains a brittle behavior.

For a material to suffer from HE, it has to be susceptible to hydrogen. The susceptibility increases for materials experiencing high strain levels and also for materials with a high yield strength [7, 8].

In general, there are three main factors governing the hydrogen diffusion in a material, as shown in Figure 1. The first factor is the atomic hydrogen present on the material surface which forms due to different scenarios, as described in Section 2.2. In other words: the amount of available hydrogen on the surface that might diffuse into the material. The second factor is the microstructure of the material. The microstructure, both primary and secondary phases, which include non-metallic inclusions and precipitates, affect both the hydrogen diffusion and trapping. The microstructure generally present in X70 steel will be further described in Section 2.8.4, and the trapping phenomenon in Section 2.6. A third factor which also needs to be accounted for is the driving force for hydrogen diffusion. This can be a result of loading, residual stresses etc., also enhancing the susceptibility of hydrogen diffusing into the metal. HE is therefore a result of these three criterions [7, 11]. Figure 1 illustrates the HE criterions.

Two common failure mechanisms related to HE are hydrogen stress cracking (HSC) and hydrogen induced cracking (HIC) [12]. The main difference is that HSC requires either residual or externally applied stress to occur, which HIC does not. HSC occurs as a result of atomic hydrogen diffusing into the material in combination with tensile stress. HIC occurs because atomic hydrogen recombines into hydrogen gas, H_2, inside the trap sites in the metal lattice. The pressure from these molecules leads to the metal cracking [12].

4
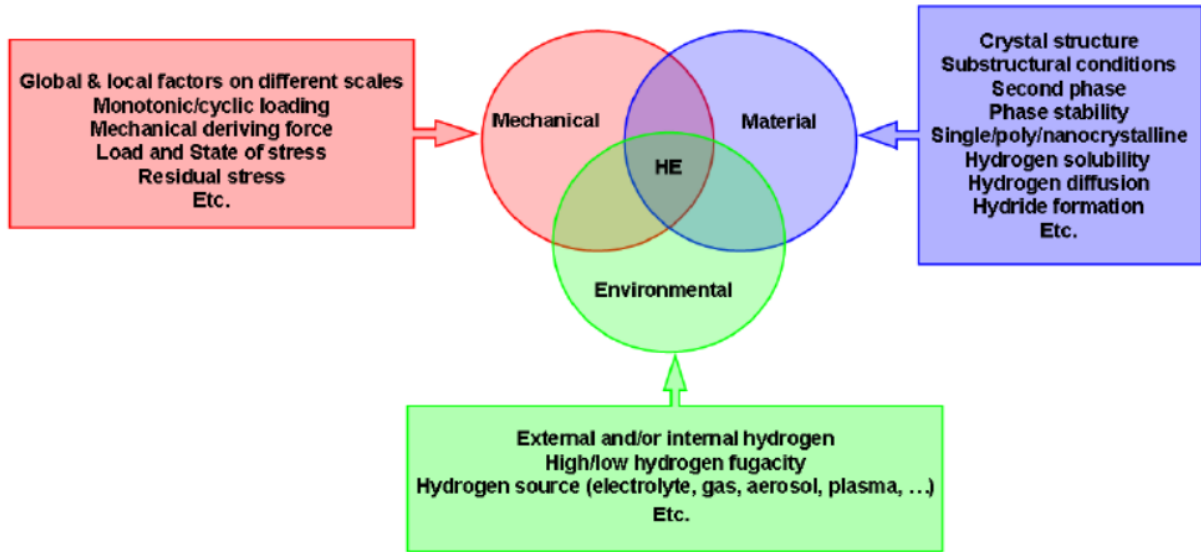
Figure 1: Criterions to be fulfilled in order for HE to occur. Obtained from [11].

2.1.2   Hydrogen embrittlement mechanisms

Today, there are three theories that dominate and have achieved (most) acceptance, even though the mechanisms of HE are not fully understood yet. These three are Hydrogen Enhanced Localized Plasticity (HELP), Hydrogen Enhanced Decohesion (HEDE) and Adsorption-Induced Dislocation Emission (AIDE). A combination of these mechanisms is often assumed to occur, with the fracture mode deciding which mechanism will be the dominating one. These three scenarios are applicable in cases where hydrides do not form [13]. HELP belongs in the group of plasticity models, HEDE is a decohesion model and AIDE an adsorption model as their names imply [3].

2.2   Sources of hydrogen

2.2.1   Cathodic protection (CP)

As a byproduct of corrosion, the hydrogen production depends on the availability of hydrogen ions, H^+. In other words, it depends on pH. In areas of low pH, the corrosion of iron and steel as a result of hydrogen reduction can take place [8]. A more common source of hydrogen in seawater is cathodic protection (CP), which may increase the hydrogen production at the cathode in the system [14].

CP is often used to protect constructions, especially offshore, against corrosion. The principle is quite straight forward; whatever needs protection is forced to act as the cathode in the system. At the cathode, the reduction reaction will occur, while the oxidation happens at the anode.

CP can be applied in one of two ways.

  a) By use of sacrificial anodes
  b) By use of an impressed current

The principle, no matter which one of the two ways (a or b) the CP is applied, is that the electrode potential of the material to be protected is pushed down in the immune area. The material will then act as a cathode, with no oxidation happening. In that way, corrosion is avoided [8]. Figure 2 shows this in a graphic way, illustrating how the potential is being pushed from the corrosion potential, E_{corr}, to the protection potential, E_p, which represents the immune area.
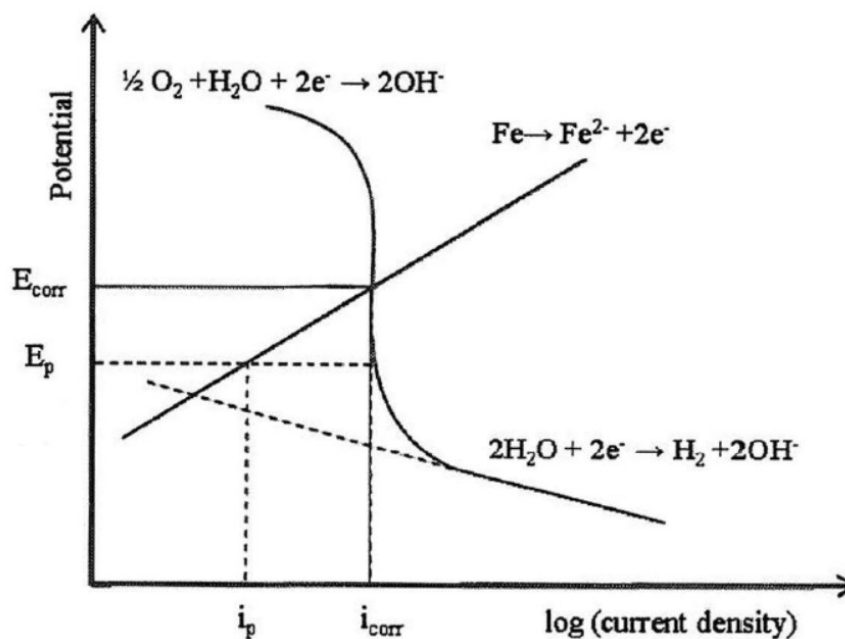
Figure 2: Current density vs. electrode potential; the principle of CP. Obtained from [15].

The main problem with this protection system is the low electrode potential achieved. To protect subsea components, the potential is normally pushed down to at least -800mV vs Ag/AgCl, which represents an accepted protection potential where the corrosion rate of iron will be so low that it's insignificant. Shortly after the CP system has been installed, the potential may be as low as -900 to -1000mV vs Ag/AgCl. By use of an impressed current, the potential will most likely drop even lower, close to the impressed current anode [8]. Normally, the oxygen reduction reaction is the dominant cathodic reaction in aqueous solutions, but at these lower potentials, a reaction called the water reduction reaction becomes dominant. In other

words, hydrogen is being produced, and we have the possibility of hydrogen entering the material [8].

Oxygen reduction:

$$O_2 + 2H_2O + 4e^- \rightarrow 4(OH)^- \qquad \textit{In alkaline solution} \qquad (2.1)$$

$$O_2 + 4H^+ + 4e^- \rightarrow 2H_2O \qquad \textit{In acidic solution} \qquad (2.2)$$

Water reduction:

$$2H_2O + 2e^- \rightarrow 2(OH)^- + 2H_{ads} \qquad \textit{In alkaline solution} \qquad (2.3)$$

$$2H_3O^+ + 2e^- \rightarrow 2H_2O + 2H_{ads} \qquad \textit{In acidic solution} \qquad (2.4)$$
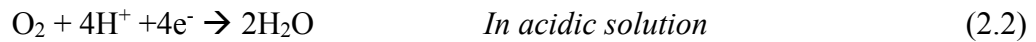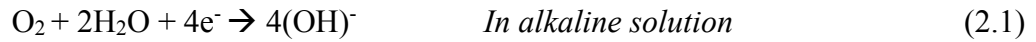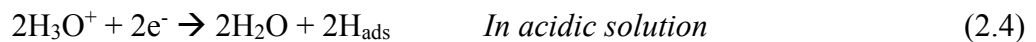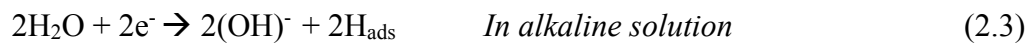
In acidic solutions where no oxidant agents, like oxygen, are present, the reduction of hydrogen ions is the dominating reduction reaction [8, 16, 17].

$$2H^+ + 2e^- \rightarrow 2H_{ads} \qquad \textit{In acidic solution} \qquad (2.5)$$
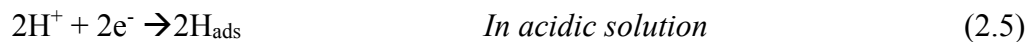
The hydrogen adsorbed on the surface can then form hydrogen gas, or in worst case, absorb/diffuse into the material as atomic hydrogen [16].

$$2H_{ads} \rightarrow H_2 \text{ (gas)} \qquad \textit{Production of hydrogen gas} \qquad (2.6)$$

$$2H_{ads} \rightarrow 2H_{abs} \qquad \textit{Hydrogen entering the material} \qquad (2.7)$$
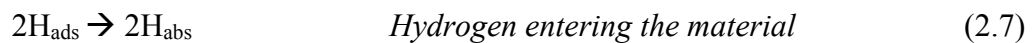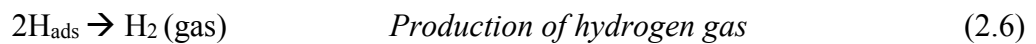
2.2.2 H_2S

Dealing with oil and gas, there is a possibility that H_2S will be present in the transported media, meaning the environment is sour. H_2S will dissolve in water, and effectively hinder the recombination of hydrogen atoms into gas molecules. It acts as a poisoning media. This will lead to more hydrogen atoms with the possibility of diffusing into the metal [18].

When H_2S dissolves in water, it results in an acid. If pH > 6, the acid will dissolve into hydrogen ions and sulphur ions [8, 18]:

$$H_2S \rightarrow H^+ + HS^- \qquad (2.8)$$
$$2HS^- \rightarrow 2H^+ + S^{2-} \qquad (2.9)$$
$$2H^+ + 2e^- \rightarrow 2H_{ads} / H_2 \text{ (gas)} \qquad (2.10)$$

There are many theories of what the reaction model for hydrogen adsorption due to H_2S and its poisoning effect looks like. In 1976, Kawashima et al [19] proposed a model for acidic environments where the concentration of HS^- is low compared to the concentration of H_2S:

$$H_2S + e^- \rightarrow H_2S_{ads}^- \tag{2.11}$$

$$H^+ \rightarrow H_{ads}^+ \tag{2.12}$$

$$H_2S_{ads}^- + H_{ads}^+ \rightarrow H_2S{\sim}H_{ads}\,(\text{unstable}) \tag{2.13}$$

$$H_2S{\sim}H_{ads} \rightarrow H_2S_{ads} + H_{ads} \tag{2.14}$$

2.2.3   Manufacturing operations

Different manufacturing operations can also lead to hydrogen entry into the material if the material is susceptible. The problem with these operations is that the hydrogen enters the material during the operation, but is not always able to escape afterwards. Some operations such as pickling, electroplating etc. therefore require a final baking heat treatment in order to expel the hydrogen as hydrogen atoms becomes more mobile at higher temperatures and therefore diffuses easily [20, 21] .

Welding, in particular, will induce residual stresses in the material. These residual stresses, in addition to stress and strain concentrations in notches, will cause hydrogen to accumulate locally [9]. This was verified by Wang et al [22], who discovered that the solubility of hydrogen was higher in the heat affected zone than in the base metal. The solubility in welds was discovered to be even higher than in the heat affected zone, pointing towards a higher level of residual stresses and hence a higher level of hydrogen inside the material due to the welding.

2.3   The diffusion mechanism – hydrogen diffusion

Diffusion is defined as the phenomenon where material transport happens by atomic movement. For diffusion in metals, there are two models that dominate even though several have been proposed, namely vacancy diffusion and interstitial diffusion. For vacancy diffusion to happen, a vacancy is needed in the metal lattice. The diffusing atom and the vacancy simply switch positions, as illustrated in Figure 3. In the case of interstitial diffusion, the diffusing atom moves from one interstitial position to another in the metal lattice. This is the main mechanism when the diffusing atoms are sufficiently small, as they have to be to fit into the positions and be able to make interstitial jumps [7].
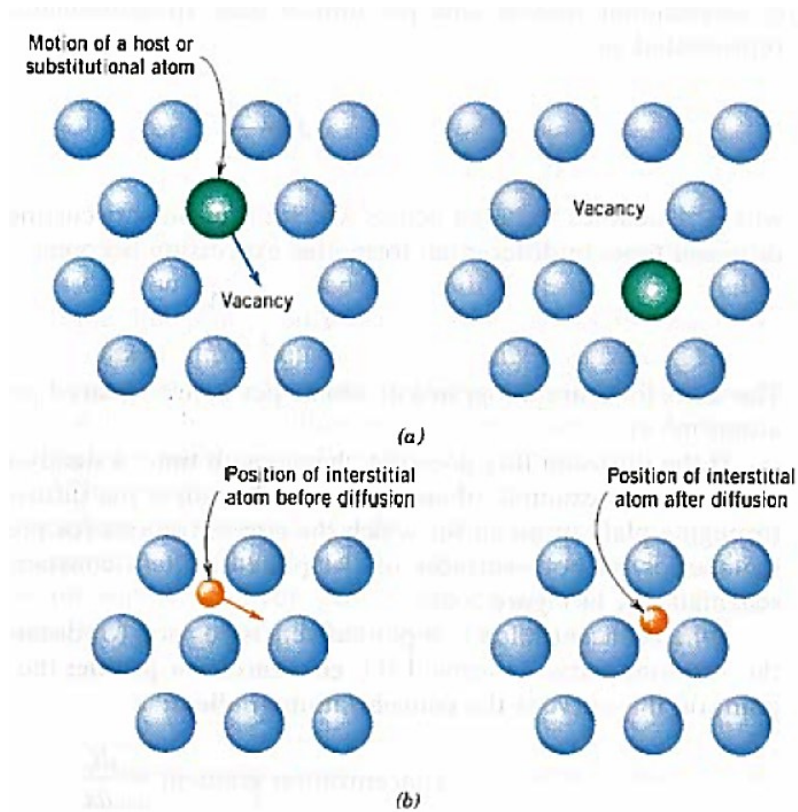
Figure 3: Illustration of (a) vacancy diffusion and (b) interstitial diffusion. Obtained from [7].

The main mechanism when it comes to hydrogen diffusion in steel is interstitial jumps in the metal lattice, as these atoms are small enough to fit inside the interstitial positions. As pointed out by Olden et al [9], different lattice structures result in different diffusion rates and different solubility of hydrogen. The X70 steel contains different microstructures, and therefore also different lattice structures, which will affect diffusion rate and solubility in different ways. The different structures are illustrated in Figure 4. In Section 2.8.4, results obtained by Park et al [23] showing which microstructures that are normally present in the X70 steel are presented.

Figure 4: Illustration of the different lattice structures. Obtained from [24].

The base centered cubic structure (BCC), which is ferritic, shows high diffusion rate and low solubility because of the open lattice structure. The face centered cubic (FCC), which is austenitic, has a closer packed lattice structure. It will therefore show low diffusion rate and high solubility as a result of this. Compared to ferrite, austenite will work as a reservoir for hydrogen. The martensitic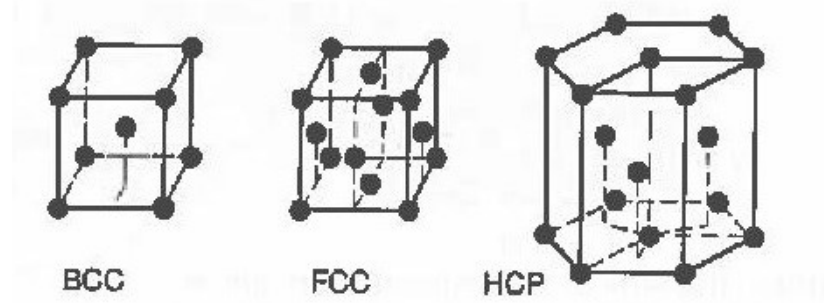 structure can contain both body centered tetragonal (BCT) and hexagonal close packed (HCP) lattice structures. The main constituent of these is BCT, but HCP has proven to increase with increasing carbon content in the steel. Both of these are closer packed than BCC, meaning they will show lower diffusion rate and higher solubility. The different structures and their diffusion and solubility properties are listed in Table 1. When it comes to how close the structures are packed, BCT and HCP will fall in between BCC and FCC [9].

Table 1: Different lattice structures resulting in different diffusion rate and solubility [9].

	BCC (ferrite)	BCT, HCP (martensite)	FCC (austenite)
DIFFUSION RATE	High	Medium	Low
SOLUBILITY	Low	Medium	High

At low temperatures, including ambient temperature, the tetrahedral sites are believed to be the main occupation sites for the hydrogen. Per unit cell, there are only half as many octahedral as tetrahedral sites. The number of lattice sites, N_l, is therefore normally based on the fact that the atoms occupy tetrahedral sites in the lattice. For tetrahedral sites, $N_l=5,23 \times 10^{23}$ *sites cm^{-3}* [10].

In order to describe the hydrogen diffusion, Fick's laws of diffusion are applicable. Fick's first law of diffusion was first proposed by Fick in 1855 [25, 26], and yields according to equation 2.15:

$$J_{ss} = -D_l \frac{\partial c}{\partial x}$$ (2.15)

This describes atom flow down the concentration gradient, meaning from areas of high concentration to areas of low concentration. The concentration gradient will be the driving force for the diffusion [7]. J_{ss}, D_l and C are the steady-state hydrogen flux, diffusion coefficient for lattice diffusion and hydrogen concentration, respectively. However, this is only applicable for steady-state diffusion. As soon as steady-state conditions no longer can be established, Fick's second law according to equation 2.16 has to be used instead [25, 26].

Fick's second law yields:

$$\frac{\partial c}{\partial t} = D_l \frac{\partial^2 c}{\partial x^2} \tag{2.16}$$

Fick's second law is the basis for plotting Fick's curve, which is a theoretical permeation transient for lattice diffusion in materials. The boundary conditions $C=C_0$ at x=0 (entry side of sample) and C=0 at x=L (exit side) are applicable. C_0, also called the sub-surface concentration, is constant at the entry side of the sample. At the exit side of the sample, this concentration is zero. The hydrogen flow as a function of time can then be derived. Equation 2.17 represents the Laplace solution, while equation 2.18 represents the Fourier solution of Fick's second law [1, 16, 17]. These equations provide a mathematical model of the hydrogen flux through the sample, but does not include any parameters that addresses the trapping phenomenon. The trapping phenomenon will be explained in Section 2.6. Fick's curve is shown in Figure 9 in a plot of $J(t)/J_{ss}$ vs. tD_l/L^2. These parameters will be further described in Section 2.5.1. The two equations should produce similar results, given a sufficient value of n is used. According to the ASTM international standard [1], a value of n=6 is recommended.

$$\frac{J(t)}{J_{ss}} = \frac{2}{\sqrt{\left(\pi\left(\frac{tD_l}{L^2}\right)\right)}} \sum_{n=0}^{\infty} exp\left\{-\frac{(2n+1)^2}{4\frac{tD_l}{L^2}}\right\} \tag{2.17}$$

$$\frac{J(t)}{J_{ss}} = 1 + 2\sum_{n=0}^{\infty}\left\{(-1)^2 exp\left(-n^2\pi^2\frac{tD_l}{L^2}\right)\right\} \tag{2.18}$$

2.4 Hydrogen permeation technique

To evaluate the hydrogen uptake, permeation and transport in metal samples, a special technique called Hydrogen permeation technique is the standard method. This method was developed by Devanathan and Stachurski and published in 1962, and is basically a method for measuring the hydrogen flux through a specimen [27]. The standard practice is now described in the ASTM standards [1]. The intention of the measurements is to establish the hydrogen diffusion coefficient and sub-surface hydrogen concentration. One requirement for a test of this

nature to be successful is that the activity on the surface of the metal sample has to remain constant throughout the testing [1]. This is further discussed in Section 3.3.4.

The basic idea behind this technique is to locate the testing sample between a cathodic, hydrogen charging cell and an anodic, oxidizing cell. Both cells are filled with an appropriate electrolyte. On the cathodic charging side, hydrogen atoms are generated on the specimen surface by charging galvanostatically with a potentiostat. The hydrogen atoms generated may then absorb into the specimen. On the anodic oxidizing side, the hydrogen that has been transported through the specimen will be oxidized by anodically polarizing this side with a potentiostat, which means that each hydrogen atom will free one electron. The immediate oxidation should result in a hydrogen concentration approximately equal to zero on this surface. The total oxidation current, which compromises the current from the transported hydrogen and the background current, can then be measured. The background current is further described in Section 3.4. The permeation current is equal to the current from the transported hydrogen [1]. Figure 5 and Figure 6 illustrates the hydrogen diffusion process and diffusion cell, respectively.
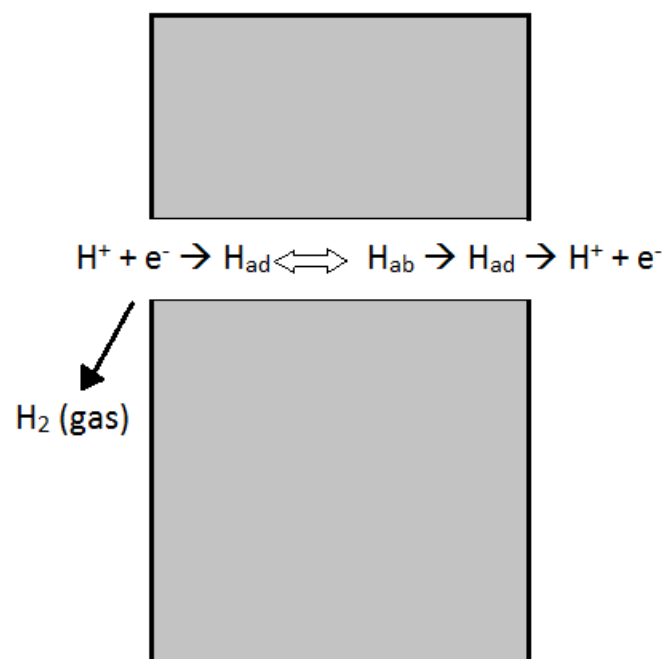
Figure 5: Simple illustration of the hydrogen diffusion process through a sample. Inspired by [15].
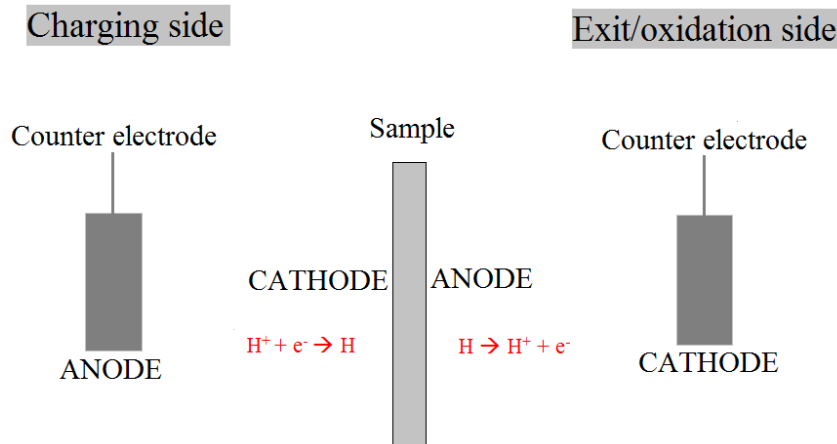
Figure 6: Simple illustration of the diffusion cell.

2.5   Determination of parameters – t_{lag} method

2.5.1   Effective diffusivity; diffusion coefficient

The effective diffusion coefficient can be found in three different ways; based on the break-through time t_b, the elapsed time t_{lag} or the by slope method [1]. The method chosen for this work is the method based on the elapsed time, the t_{lag} method, which has been the chosen method for analyzing the results in numerous experiments described in the literature [15, 23, 28-30]. The equations for calculating the different parameters for this method are described in the ASTM standards [1].

The time-dependent permeation flux J(t) can be found according to equation 2.19:

$$J(t) = \frac{I(t)/A}{F} \qquad (2.19)$$

Where I(t) is the time-dependent anodic current, A is the area of the sample and F is Faraday's constant (F=9.6487 x 10^4 Cmol^{-1}).

The steady-state permeation flux J_{ss} can be found according to equation 2.20:

$$J_{ss} = \frac{Iss/A}{F} \qquad (2.20)$$

Where I_{ss} is the steady-state anodic current.

The diffusion coefficient can then easily be found by help of equation 2.21 [31]:

$$D_{eff} = \frac{L^2}{Mt_{lag}}$$ (2.21)

Where L is the thickness of the sample. This coefficient has units [m^2 s^{-1}] if L is given in [m] and t_{lag} in [s]. The constant M is dependent on the time t that corresponds to a certain point chosen on the ideal Fick's curve. This correlation is shown in Table 2.

Table 2: The correlation between the normalized flux J(t)/J$_{ss}$ and the normalized time tD$_l$/L^2. Obtained from [31].

J(t)/J$_{ss}$	1%	10%	30%	40%	63%	80%	90%
tD$_l$/L^2	0,04	0,06	0,10	0,12	0,17	0,23	0,30
M=1/(tD$_l$/L^2)	25,4	15,1	10,0	8,3	5,9	4,3	3,3

As stated by the ASTM standard for hydrogen permeation measurements [1], the relation between the t_{lag} and the constant M is described by equation 2.22, meaning M=6. This value is found by extrapolating, and it has been shown that t_{lag} can be found at the point where J(t)/J$_{ss}$=0,63 [3, 27], as shown in Figure 7.
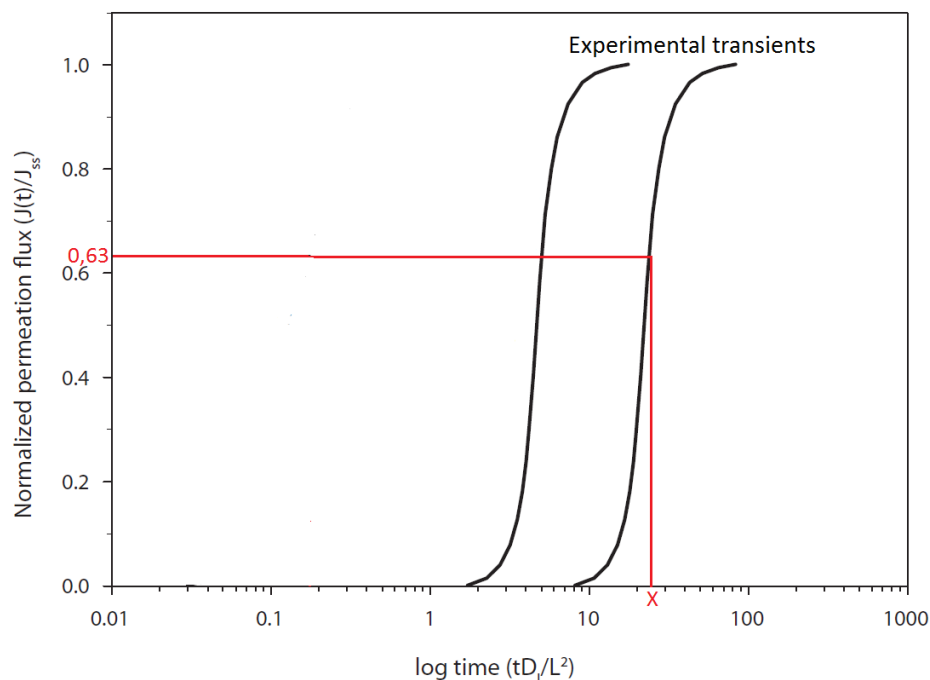

Figure 7: Graph illustrating the point where J(t)/Jss=0,63. t_{lag} is found at point x. Adapted from [28].

14

This gives the equation for the effective diffusion coefficient calculated from the point where $J(t)/J_{ss}=0,63$ (63% of J_{ss}), which according to equation 2.22 yields [1]:

$$D_{eff} = \frac{L^2}{6t_{lag}} \qquad (2.22)$$

The diffusion coefficient is independent of the concentration of hydrogen atoms in the sample. This can easily be seen from equation 2.22, where no parameters involving hydrogen concentration is involved. Therefore, the distribution of diffusible atomic hydrogen inside the sample can be illustrated by a gradient which is linear [3].

The diffusion coefficient is however dependent of temperature, which will be further outlined in Section 2.8.3. This correlation is described by the Arrhenius equation, equation 2.23 [15, 32]:

$$D_{eff} = D_0 \exp\left(\frac{-E_l}{RT}\right) \qquad (2.23)$$

D_0 is a pre-exponential factor, and E_l is the activation energy for lattice diffusion. R=8,314 mol^{-1}K^{-1} (gas constant) and T is the absolute temperature in Kelvin (K).

2.5.2   Sub-surface hydrogen concentration

The sub-surface hydrogen concentration C_0 can be found according to equation 2.24 [1]:

$$J_{ss} = \frac{I_{ss}/A}{F} = \frac{D_l C_0}{L} \rightarrow C_0 = \frac{(I_{ss}/A)L}{FD_l} \qquad (2.24)$$

D_l is determined by equation 2.25:

$$D_l = 7,23 \times 10^{-4} \exp\left(\frac{-Q}{RT}\right) cm^2 s^{-1} \qquad (2.25)$$

Where the lattice activation energy Q=5,69 *kJ mol^{-1}* (the energy needed for hydrogen atoms to make a jump between two lattice sites). This diffusion coefficient was obtained by Kiuchi et al [33], and is applicable for ferritic lattice diffusion .

The sub-surface hydrogen concentration C_0 is a measure of the concentration of hydrogen on the charging side of the material. It is assumed that C_0 remains constant during the testing, as mentioned in Section 2.3.

As the samples will contain traps, D_l is not applicable for the calculation of the sub-surface hydrogen concentration. The diffusion will not be pure lattice diffusion [15]. Therefore, D_{eff} is used in further calculations. The expression for C_0 then turns into equation 2.26 [1]:

$$C_0 = \frac{(I_{ss}/A)L}{FD_{eff}}$$ (2.26)

The unit for C_0 is [ppm W], meaning [mg H_{abs}/kg $_{steel}$]. Using atomic weight H=1,0079g mol^{-1} and ρ_{steel}=7,9g cm^{-3}, the transformation factor according to equation 2.27:

[ppm W]=127528 x [mol H_{abs}/cm^3] ~ 0,128 x [mol H_{abs}/m^3] (2.27)

is valid.

At steady state conditions, the amount of diffusible atomic hydrogen in the sample can be expressed by equation 2.28 as a charge, $q_{average}$ [31]:

$$q_{average} = \frac{C_0 L}{2}$$ (2.28)

The parameters described in Section 2.5.1 and 2.5.2 were calculated both manually and by using a software developed by Simonsen [6] for the experimental data obtained in this work.

2.6   Trapping

Different sites in the steel, so called trapping sites, will delay the hydrogen diffusion through the specimen. Different features such as dislocations, inclusions, precipitate particles, grain boundaries and phase boundaries may cause the hydrogen getting trapped in the steel by acting as trapping sites [9]. The increase in binding energy compared to the binding energy for lattice sites determines that a site will act as a source of hydrogen, i.e. a trap [10]. Based on the binding energy for the traps compared to the migration energy for hydrogen in the metal lattice, they can be divided into reversible and irreversible traps [1].

A trap being reversible means that the hydrogen is able to escape, i.e. the trapping can be reversed. The binding energy is lower than the migration energy, and the atoms will therefore be able to escape. Tempering is enough to overcome this binding energy and release the hydrogen from the reversible trapping sites. A trap being irreversible means that the hydrogen is not able to escape even with tempering as the binding energy is too high [1, 10].

If the metal is close to free of defects and therefore has a low density of trap sites, the hydrogen diffusion is controlled only by lattice diffusion. This can also happen if the traps have already been filled, and the hydrogen charging continues. Figure 8 shows in a graphic way that the concentration of hydrogen in lattice sites as well as in irreversible trap sites is assumed constant

16

throughout the sample thickness. The concentration of hydrogen in reversible trap sites, however, varies with the sample thickness [10].
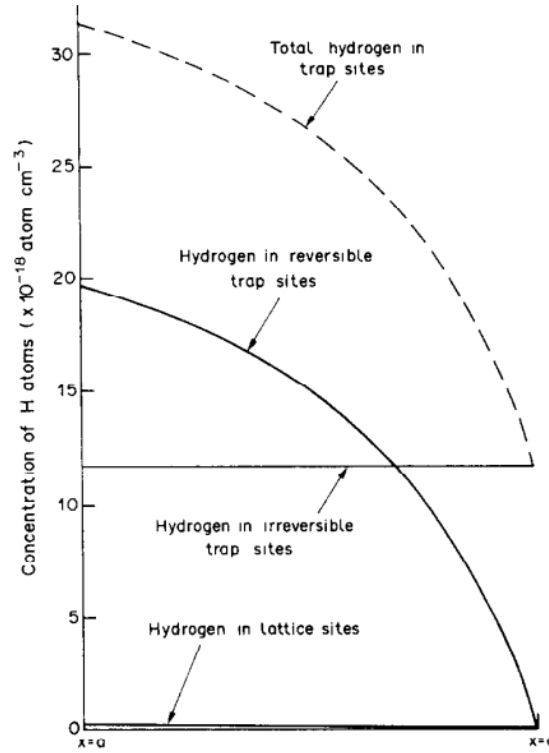
Figure 8: Concentration of hydrogen atoms through the sample thickness. x=a is at the entry side (a=L=thickness of the sample). Obtained from [10].

The diffusion coefficient $D_{eff,trap}$ when reversible traps are present can be calculated according to equation 2.29 [15, 32]:

$$D_{eff,trap} = \frac{D}{1+\frac{N_r k_r}{p_r}}$$
(2.29)

where k_r is the capture rate and p_r the release rate for each reversible trap. N_r is the number of reversible traps.

Taking the Arrhenius equation, equation 2.23, the energy for binding E_b and energy for lattice activation E_l into consideration, the expression changes to equation 2.30:

$$D_{eff,trap} = D \frac{N_l}{N_r} exp \left(\frac{-E_b}{RT}\right) = D_0 \frac{N_l}{N_r} exp \left(\frac{-(E_b+E_l)}{RT}\right)$$
(2.30)

Note that the diffusion coefficients calculated in Chapter 4 are calculated based on the elapsed time, t_{lag}, equation 2.22. For the full derivation of equation 2.29 and 2.30, please refer to Oriani [32] and Smirnova [15].

When permeation tests are performed, the irreversible traps are assumed to be filled during the first hydrogen charging cycle. A charging cycle is also referred to as a transient, consisting of both a charge and discharge transient. Therefore, in order to separate the effect of the irreversible and reversible trapping, the conditions have to be kept constant and more than one transient measured [31]. Normally, a total number of three transients is sufficient. The break-through time for the first transients will most likely be higher compared to transients measured later on. This means that the time for the hydrogen to diffuse all the way through the material is higher because it takes time for traps to get filled, and this can be seen by noticing that the first transient will be displaced to the right compared to the subsequent ones as shown in Figure 9 [1, 10]. Another less common consequence of trapping, causing a "double plateau" trend in the transients, was discovered in the experimental work of this thesis described in Chapter 4. This behavior has been reported earlier by Iino and Fallahmohammadi [4, 31].

When plotting the results in a normalized permeation flux $(J(t)/J_{ss})$ vs. dimensionless time (tD_l/L^2) graph, as shown in Figure 9, and a plot of Fick's curve is included in the graph, the steepness of the transient plot compared to Fick's curve can tell us something about the nature of the transient. If the transient plot is steeper than Fick's curve, calculations based on the elapsed time, t_{lag}, can be done as the trap occupancy is significant. If it is less steep, it can be because of unsteady surface conditions [15] [1].
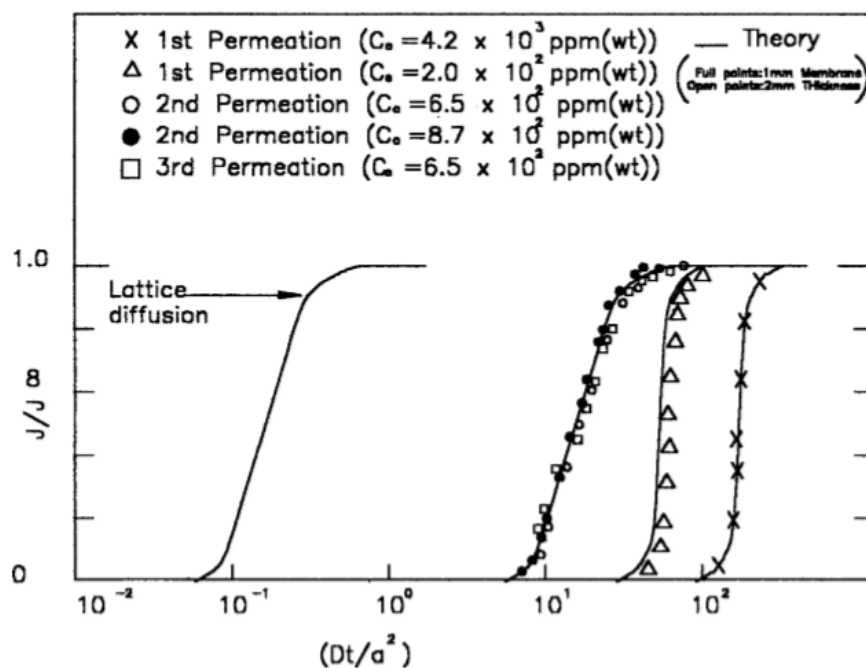

Figure 9: Theoretical transient (Fick's curve) to the left, experimental transients to the right. Increased break-through time can easily be detected by noticing that the first transient is displaced to the right. Obtained from [1].

2.7   Determination of parameters – curve fitting

2.7.1   Charging transient

To examine the validity of the D_{eff} calculated by the time-lag method, a possibility is to insert the D_{eff} calculated at 63% of J_{ss} into the solution of Fick's second law with the same boundary conditions as described in Section 2.3, namely C=0 at the exit/anodic side and $C=C_0$ at the charging/cathodic side. This has earlier been done by Fallahmohammadi et al [31]. Equation 2.31 shows the Fourier solution of Fick's second law where the D_{eff} is added to the equation.

$$\frac{J(t)}{J_{ss}} = 1 + 2\sum_{n=1}^{\infty}\left\{(-1)^2 exp(-n^2\pi^2\frac{tD_{eff}}{L^2})\right\} \tag{2.31}$$

A value of n=6 is sufficient for plotting this theoretical curve [1]. By plotting this together with the experimental permeation transient, the degree of overlap between the theoretical model and the experimental results can be assessed. Figure 10 shows a plot of the experimental and the theoretical charging transient. The greater degree of overlap, the more accurate D_{eff} is.

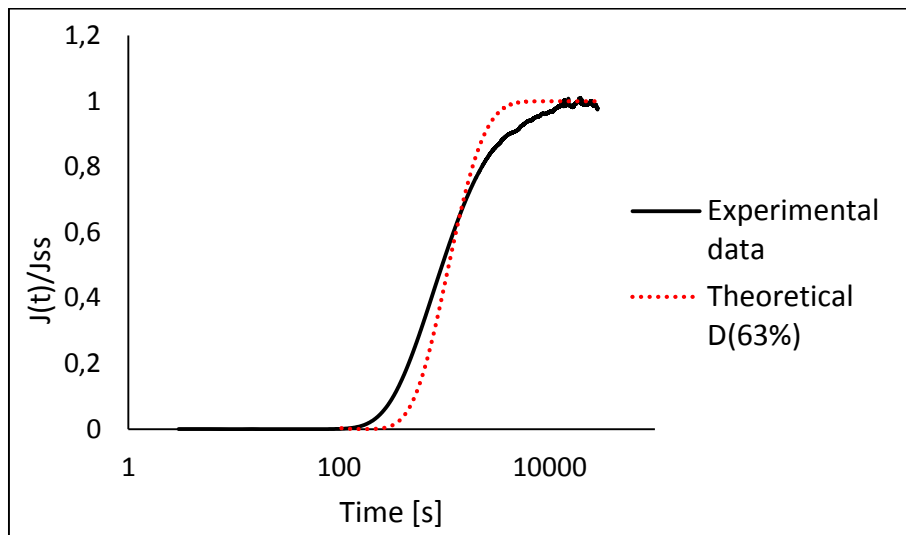Figure 10: The experimental data and the theoretical Fick's curve calculated with the D_{eff} found from the t_{lag} method.

By reversing the process and performing a simple curve fitting using the least squares method, one can find the value of D_{eff} which gives the greatest degree of overlap possible. This was done in the software developed by Simonsen [6] for the experimental data obtained in this work. The

software executed the curve fitting procedure and extracted the D_{eff} from the fit. However, as mentioned in Section 2.3, Fick's laws does not include any parameters for trapping. Therefore, when changing the D_{eff} in the theoretical model, the only thing happening with the theoretical curve is a displacement in time. In other words, the curve fitting based on Fick's second law alone will never give a perfect fit as long as traps are presents. To make a more realistic model of the hydrogen diffusion, the adding of parameters addressing trapping to the model is essential.

Iino has proposed a model for hydrogen diffusion including parameters for both reversible and irreversible trapping sites [3-5]. The experimental results presented in this work obtained according to this method was also done using the software developed by Simonsen [6]. Based on this model, the software provides the curve fitting of the model to the experimental data, enabling the extraction of the diffusion coefficient, D_{eff}, and different parameters addressing trapping.

The model is based on the equations developed by McNabb and Foster [3, 34, 35], equation 2.32 and 2.33, which only takes account of the reversible trapping sites.

$$\frac{\partial c}{\partial t} + N \frac{\partial \theta}{\partial t} = \nabla(D\nabla c) \tag{2.32}$$

$$\frac{\partial \theta}{\partial t} = kc(1 - \theta) - p\theta \tag{2.33}$$

C=hydrogen concentration as a function of time and position, N=reversible trap density, θ=fraction of occupied traps, p_r=probability that a hydrogen atom gets released from a reversible trap in one second and k=number of atoms captured in reversible traps in a volume ∂V in one second.

Iino added parameters to describe irreversible trapping sites to the equation. The resulting equations in non-dimensional form yields according to equation 2.34 and 2.35 [3-5]:

$$\frac{\partial u}{\partial \tau} + \frac{\partial w}{\partial \tau} + \frac{\partial v}{\partial \tau} = \nabla^2 u \tag{2.34}$$

$$\frac{\partial v}{\partial \tau} = \kappa u(1 - \theta_i) \tag{2.35}$$

Where equation 2.36-2.42 describes the different fitting parameters:

$$w = N_i \frac{\theta_i}{C_0}; \kappa = N_i k_i \frac{L^2}{D}; u = \frac{c}{C_0}; v = C_0 k_r \frac{L^2}{D}; \tau = D\frac{t}{L^2}; \lambda = N_r k_r \frac{L^2}{D}; \mu = p_r \frac{L^2}{D} \quad \text{(2-36-2.42)}$$

i=irreversible traps, r=reversible traps

The equation for hydrogen flux through the anodic/exit side of a sample can then be described by equation 2.43 and 2.44 [3-5]:

$$j(0,\tau) = \frac{\sqrt{\kappa}}{sinh\sqrt{\kappa}} + \sum_{n=1}^{\infty} \frac{2n^2\pi^2}{s_n^{-}\left[1+\frac{\lambda\mu}{(s_n^{-}-\mu^2)}\right]} e^{-s_n^{-}\tau} + \sum_{n=1}^{\infty}(-1)^n \frac{2n^2\pi^2}{s_n^{+}\left[1+\frac{\lambda\mu}{(s_n^{+}-\mu^2)}\right]} \quad (2.43)$$

Where

$$s = -s_n^{\pm} = -\frac{1}{2}\left[n^2\pi^2 + \kappa + \lambda + \mu \pm \sqrt{(n^2\pi^2 + \kappa + \lambda - \mu)^2 + 4\lambda\mu}\right] \quad (2.44)$$

In Figure 11, permeation transients constructed after equation 2.43 for diffusion in a material with both reversible and irreversible traps are shown. The irreversible trapping effects that affect the first transients result in an increased break-through time. For transient number four, a "double plateau" behaviour can be seen, which in this model is assumed to be a cause of the reversible trapping effects. The curve increases at a high rate, then flattens out a moment before it starts increasing at a high rate again. Sufficiently small values of μ causes this behaviour [3]. The curve marked "Fourier" represents the Fourier solution of Fick's second law, Fick's curve.
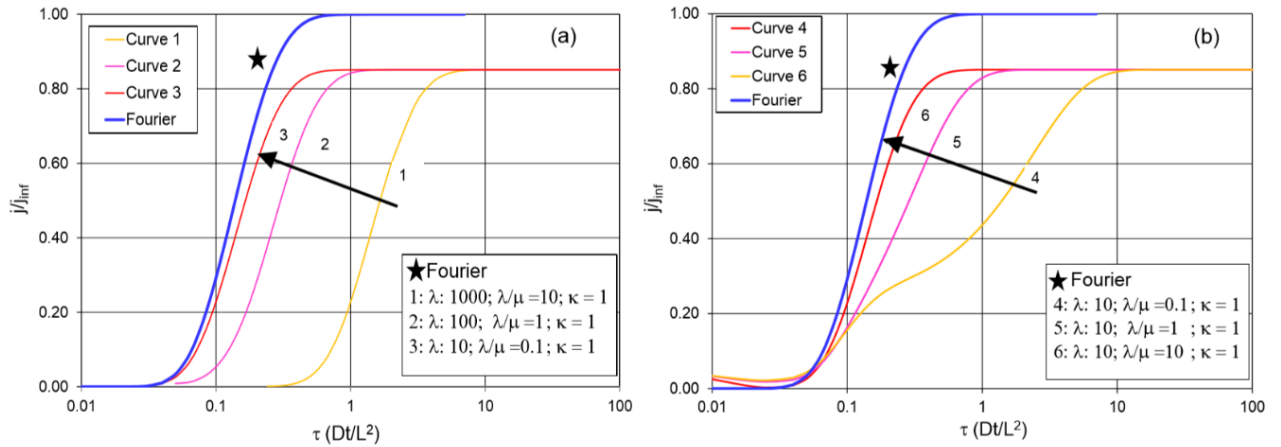
Figure 11: Permeation transients for diffusion in a material with both reversible and irreversible traps. Obtained from [3].

2.7.2   Discharge transient

When finding the diffusion coefficient of the material, the discharge transient is also of interest as this can be used to determine D_{eff} as well. The basis for the simple modelling of this transient is based on the Fourier solution of Fick's second law [3, 31, 36]. In other words, no trapping is taken account of. Equation 2.45 describes the model for fast discharge where the hydrogen is assumed to be able to exit from both the anodic and cathodic side of the sample. If the hydrogen atoms are only able to escape from the anodic side, a model for slow should be used [3]. The

boundary conditions of this model states that C=0 at the exit/anodic side and C=0 at the charging/cathodic side.

$$\frac{J(t)}{J_{ss}} = 1 - \left(1 + 2\sum_{n=1}^{\infty}\left\{(-1)^2 exp(-n^2\pi^2\frac{tD_{eff}}{L^2})\right\}\right) \tag{2.45}$$

First of all, by plotting this theoretical curve by inserting the D_{eff} calculated by the t_{lag} method for the charging transient, the compliance between the charge and discharge transients can be assessed. By reversing the process, i.e. extracting the D_{eff} from fitting the theoretical curve to the experimental one by achieving the highest degree of overlap, a more correct assessment of the compliance between the D_{eff} from the charge and discharge transients can be performed. During the discharge transient, the hydrogen occupied in lattice sites as well as in reversible trapping sites is released. A conclusion to the works by Zakroczymski and Fallahmohammadi [3, 36], is that hydrogen in the lattice sites gets released before the reversibly trapped hydrogen. This is plausible considering the traps show a higher binding energy than lattice sites [10]. Therefore, when fitting the theoretical model to the discharge curve, the first part of the curve will be in best compliance with the theoretical model and describe the lattice diffusion in the best possible way. This is illustrated in Figure 12. The fitting of the model to the experimental curve was done manually to achieve the best possible fit in the beginning of the experimental discharge transient. For curves that follow Fick's second law, the prediction says that the charge and discharge transient should intersect at J(t)/Jss=0,5, meaning that they share the same diffusion coefficient [3].
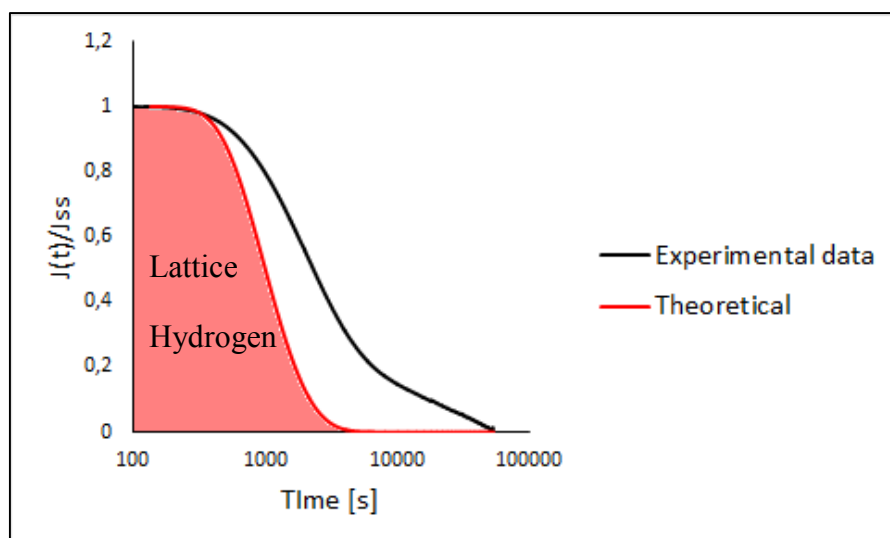

Figure 12: The experimental data and the theoretical Fick's curve calculated with the D_{eff} to give the best possible fit. Inspired by [3].

For an idealistic diffusion situation without trapping, it is assumed that 1/3 of the diffusible hydrogen atoms exits through the exit/anodic side while 2/3 exits through the charging/cathodic side after the hydrogen charging on the charging/cathodic side has been interrupted [3].

2.7.3   Partial charge and discharge transients

The method of partial charge and discharge, as suggested by Zakroczymski [36], also gives a basis for analysing the diffusion properties of the material. The idea behind this is to overcome the trapping effects by first filling the traps through a normal charging transient, and then increase the charging of the hydrogen even more to push the permeation current to a higher, steady state level. Surface processes experienced in the very first charging transient of a hydrogen free material are also assumed to be overcome. The part of the permeation curve obtained after the push in hydrogen charging will be the foundation for the partial charge analysis. By lowering the charging of the hydrogen to the original level, a partial discharge transient is initiated. When the original steady state level again is achieved, the charging of hydrogen can be interrupted and the normal discharge transient will be initiated [36] . This procedure is further described in Section 3.4.2. Figure 13 illustrates the partial charge and discharge transients.

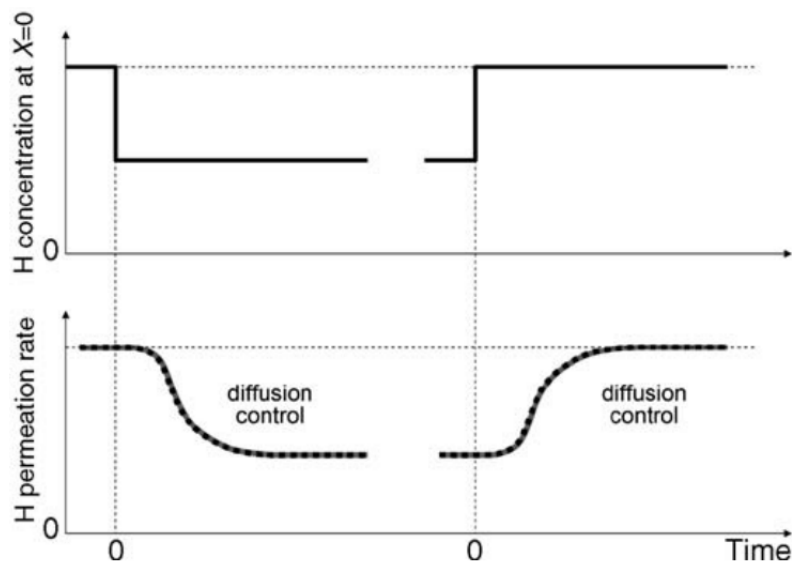Figure 13: Partial charge and discharge transients. The sub-surface concentration C_0 at the entry side is constant, meaning neither surface processes nor trapping affect the transient. Obtained from [36].

The equations used to model the theoretical curve for the partial charge and discharge transients are the same as for the standard charge and discharge transients, namely equation 2.31 and 2.45.

As the traps are assumed to be filled prior to the partial charge transient and lattice diffusion the dominating mechanism, they should provide an adequate model for the diffusion. The partial charge and discharge transient are therefore assumed to intersect closer to $J(t)/J_{ss}=0,5$ than the standard charge and discharge transients will, meaning they will both follow Fick's second law to a greater extent and represent lattice diffusion [3]. In other words, this method suggests that analysis with only one unknown parameter, D_{eff}, is sufficient.

2.8   Influencing parameters on hydrogen diffusion

2.8.1   Steel grades

High strength steels can be produced with different steel grades. When it comes to the production process for high strength steels, thermomechanical control process (TMCP) rolling, which emerged in the 70's, is used up to X70 with the aim of refining the grains to increase the strength. For X80, thermomechanical rolling followed by accelerated cooling is the appropriate production process. The carbon content for this steel has been reduced compared to the lower grades, which gives it better weldability. Higher grades have also been accomplished. The X100 is produced by microalloying with molybdenum, nickel and copper [14]. One of the reasons why X70 is a commonly used pipeline steel even though higher grades exist, is because increased strength does not prevent buckling [37]. Buckling is one of the main concerns when it comes to pipelines, especially during pipelaying by reeling.

The higher steel grade, i.e. the higher strength and hardness, the greater is the possibility of HE as the material becomes more and more susceptible to hydrogen. Therefore, high steel grades are advantageous because of the toughness, but their susceptibility to HE is a big drawback. As concluded by Hardie et al [38], the control of cathodic protection systems is more important for higher strength grades as they are more susceptible to HE, meaning it is more important to avoid such low electrode potentials that hydrogen reduction becomes the main reduction reaction as mentioned in Section 2.2.1.

2.8.2   Plastic deformation

Tensile stress can have different influences on the diffusion rate depending on whether the material is in the elastic deformation zone or the plastic deformation zone. If the material undergoes elastic deformation, the diffusion rate and permeation flux is assumed to increase because of the expanded lattice. If the material undergoes plastic deformation, on the other hand, the dislocations will act as trapping sites, and therefore the hydrogen diffusion rate will go down and break-through time increase as more hydrogen gets trapped [18].

If the percent of plastic strain ε_p is known, the trap density N_T can be found by the equation 2.46 [28, 39]:

$$logN_T = 23.26 - 2.33\exp(-5.5\varepsilon_p) \qquad (2.46)$$

2.8.3   Temperature

It has been shown, several times, that increased temperature has proven to increase the permeation current. In other words, the diffusion coefficient will increase [20]. The correlation between hydrogen diffusion and temperature is described by equation 2.23, the Arrhenius equation. When the diffusion coefficient is obtained for a material at minimum three different temperatures, the diffusion coefficient can be plotted against the inverse of the temperature. This allows the Arrhenius line to be estimated with regression, and the reversible trap density N_r and binding energy E_b can be estimated [15, 28].

2.8.4   Microstructure

As described in Section 2.3, different microstructures result in different diffusion rate and solubility.

To obtain the microstructure of X65 high strength steel, as done by Park et al [23], the specimen must be examined with an optical microscope (OM), and a scanning electron microscope (SEM). The results of the investigation done by Park et al [23] showed that all X65 specimens manufactured by TMCP rolling had a primary phase consisting of elongated Ferrite (F), while the second phase varied depending on the start cooling temperature (SCT) and finish cooling temperature (FCT), as shown in Figure 14.
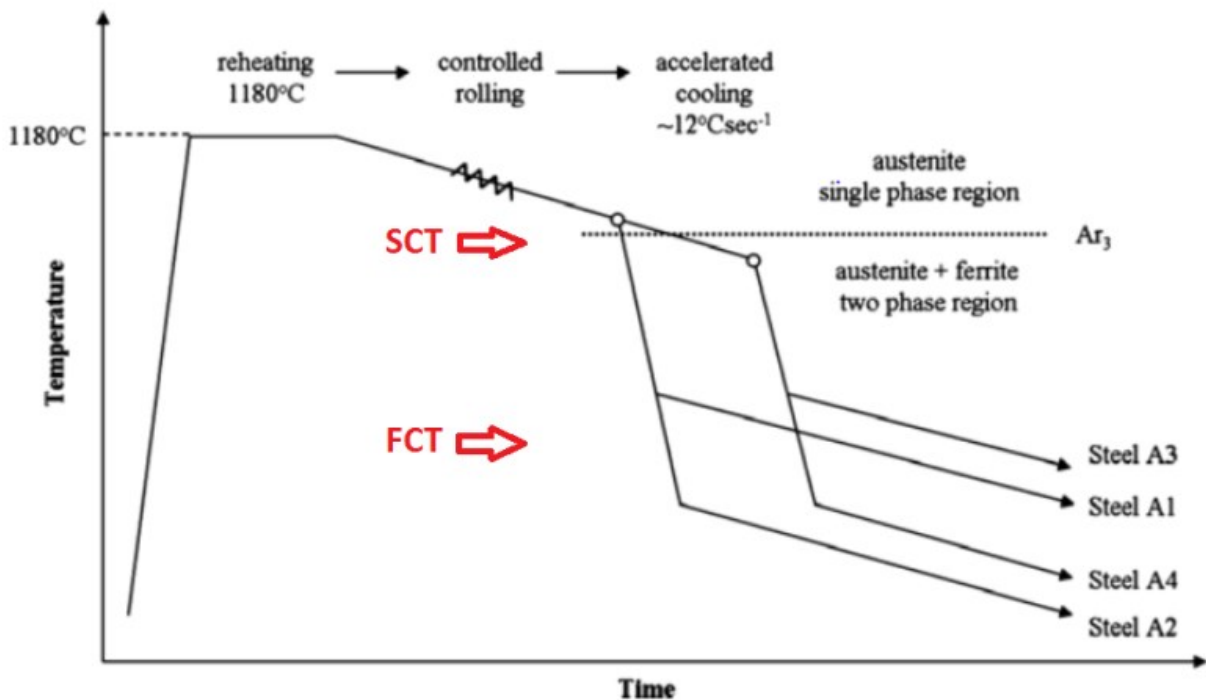
Figure 14: TMCP rolling process with resulting microstructures. Adapted from [23].

The second phases for samples A1-A4 varied between degenerated pearlite (DP), acicular ferrite (AF) and bainite (B). The resulting microstructures are shown in Figure 15. Martensite/Austenite (M/A) constituents were also found, and the amount was found to increase with decreasing FCT (at constant SCT).

As a conclusion to their testing, Park et al [23] suggested that the second microstructure phase also affects the diffusion properties of the steel. The different phases were ranked based on their hydrogen diffusivity (D_{eff}), solubility (C_0) and permeability ($J_{ss}L$) in addition to the amount of hydrogen trapped in irreversible trapping sites. Acicular Ferrite showed low diffusivity and high solubility, which is assumed to be synonymous with high trapping efficiency. The Martensite/Austenite constituents were also found to have a high trapping efficiency, and the conclusion was that Acicular Ferrite and Martensite/Austenite constituents will act as reversible trapping sites for the hydrogen atoms. In Section 4.3,1, the microstructural investigation of the X70 steel and Fe3wt.%Si samples used in this work will be described.
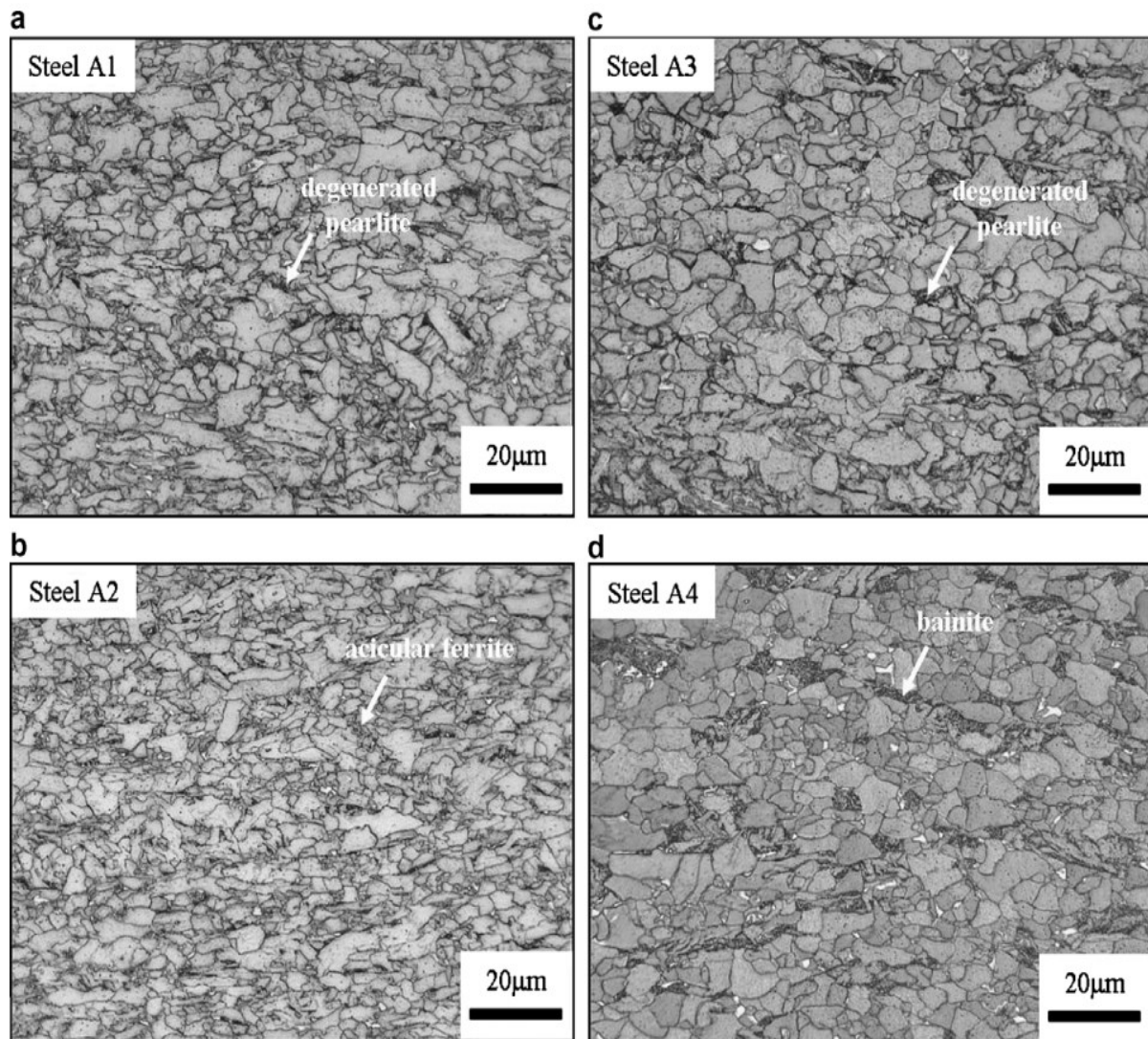
Figure 15: Resulting microstructures from different SCT and FCT. Obtained from [23]. The second phase Degenerated Pearlite for Steel A1 and A3, Acicular Ferrite for Steel A2 and Bainite for Steel A4.

Chapter 3

Experimental

3.1   Apparatus

To conduct the permeation measurements, permeation cells designed and produced during an earlier project work [2] were used. The cells were made out of glass with the possibility to seal all openings, so that the whole setup could be submerged into a water bath of steady temperature. This was achieved by threading the openings and sealing with caps and gaskets. The possibility of controlling the temperature was a way of minimizing scatter in the results, as just a minimal temperature variation could affect the results a lot. The experimental setup consisted of two cells, one for the cathodic side and one for the anodic side. The testing sample was located between the two cells, and sealed with a part made out of Kel-F (PCTFE, PolyChlorotriFluoroEthylene) and POM (PolyOxyMethylene), also designed and produced during the earlier project work. A model of the setup is shown in Figure 16. Viton O-rings were used on both sides of the testing sample to ensure complete sealing. The sealing mechanism is shown in Figure 18 and Figure 19.
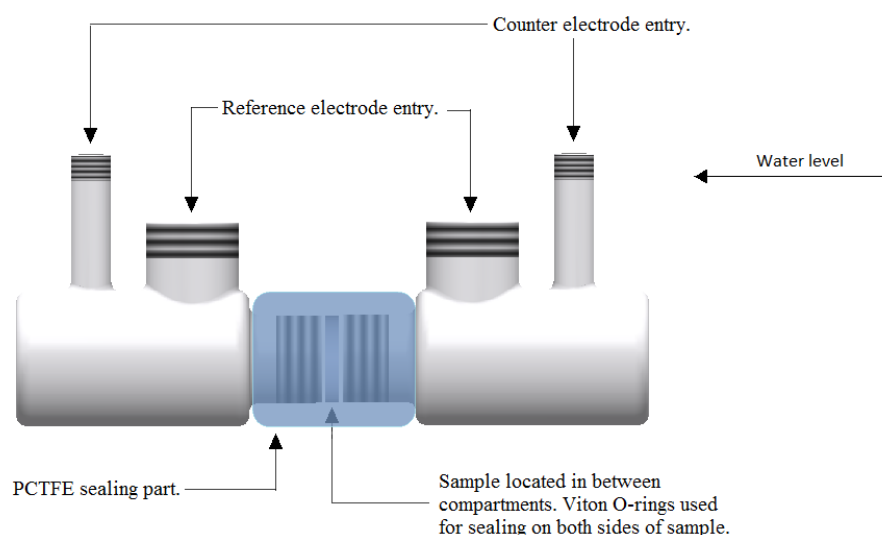

Figure 16: 3D-model of the produced cell.

To get the reference electrodes as close to the sample as possible, a Luggin-capillary for each reference electrode was also produced. Instead of having the capillaries open in the end to have direct flow of the electrolyte through the opening, they were produced with a tip made out of

cured Aluminium oxide (Al_2O_3). This ensured flow of ions without being dependent on liquid flow through the capillaries.

For the counter electrode openings, thin Silicon gaskets were used for sealing inside the caps. The counter electrodes consisted of Pt-wires. These openings were made so high they would reach above the water surface when submerged, meaning water from the bath leaking in through these openings was no threat. For the capillary openings, the sealing inside the caps were made out of Teflon and Silicon. These had to seal good enough to avoid liquid from the bath leaking in, since these openings were made lower and would be submerged. The capillaries, which were L-shaped, would not have fitted if the openings had been higher. A picture of the entire setup inside the water bath shown in Figure 17. The water bath was placed inside a Faraday cage to minimize noise in the results.
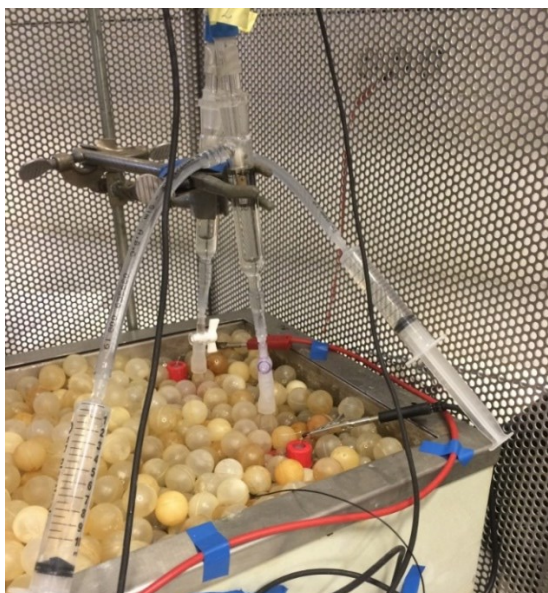

Figure 17: Experimental setup. Counter electrode openings reach above the water surface.
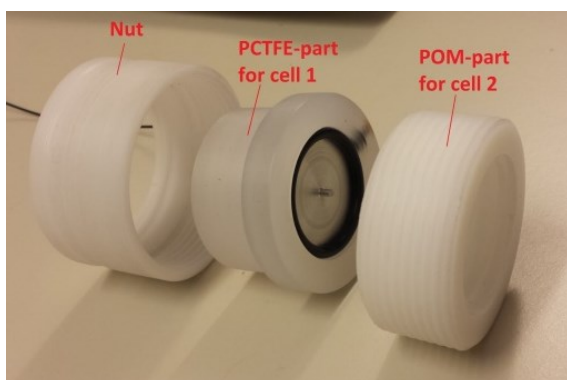

Figure 18: Sealing part components.

Figure 19: Completely assembled sealing part.

3.2   Electrolyte

Instead of using an aqueous solution where the solubility of oxygen is high, an electrolyte based on glycerin ($C_3H_8O_3$) and borax ($Na_2B_4O_7 \cdot 10H_2O$) was used. It was diluted with distilled water to obtain the desired viscosity and conductivity, and this was used inside the cells as well as inside the capillaries to ensure contact with the reference electrodes. The measured pH of the solution was approximately 7.

3.3   Testing samples

The testing throughout this work was done on pure ferritic Fe 3wt.% Si samples and X70 high strength steel samples which contain a more complex microstructure. The examination of the X65 microstructure done by Park et al. [23] is described in Section 2.8.4, and the investigation of both materials used in this work using SEM is described in Section 4.3.1. The exposed area of the samples in the cell was 4,4 *cm²*.

3.3.1   Fe 3wt.% Si

The first material to be tested during this work was Fe 3wt.% Si. This material is a single phase ferritic, BCC, crystal which resembles pure iron when it comes to electrochemical behaviour [11]. The effect of the ferritic microstructure on the hydrogen diffusion properties is described in Section 2.3. The composition of the material is shown in Table 3.

Table 3: Composition of Fe3wt.%Si. Obtained from [11].

Element	C	Si	Mn	P	S	Cr	Ni	Mo
Weight%	0,003	2,383	0,202	0,013	0,012	0,033	0,048	0,015
	Cu	Al	Ti	Nb	V	B	Zr	Ce
	0,020	0,365	0,005	0,020	0,002	0,0008	0,005	0,009

3.3.2   X70 high strength steel

The second material to be tested during this project with regards to hydrogen properties was X70 high strength steel received in the form of a hot rolled plate. The term X70 refers to the yield strength of the material, namely 70ksi (~485MPa). The properties and a more detailed description of X70 structural steel can be found in Appendix D. This material contains a complex microstructure, which will be further investigated in Section 4.3.1. The composition of the material is shown in Table 4. A result of the TMCP rolling production process is that the ferrite grain size is reduced significantly [40]. This results in a finer grain structure for the as received X70 steel samples than for the Fe3wt.%Si samples.

Table 4: Composition of X70 high strength steel. Obtained from the material certificate shown in Appendix D.

Element	C	Si	Mn	P	Ni	S
Weight%	0,047	0,098	1,74	0,008	0,243	0,0006
	Cr	Mo	Cu	V	Ti	N
	0,047	0,042	0,215	0,001	0,01	0,0025

3.3.4   Preparation of samples

To fit inside the cell, the samples were mechanically cut to a circular shape with diameter Ø29mm and thickness 1 mm for the Fe3wt.%Si samples and 2 mm for the X70 steel samples. To prepare the surface, mechanical grinding and polishing were utilized. First, the samples were grinded down to a 4000 grit finish, and then polished down to 1µm finish. To know the exact thickness, the average thickness of ten measurements on the sample was found. The Fe 3wt.% Si samples had a thin polymer layer on when received, which had to be removed by grinding before the surface could be readily prepared.

When using an aqueous solution inside the permeation cells, the samples normally has to be coated with a layer of palladium (Pd) on the anodic side of the sample as done by Smirnova and Hauge [15, 28] among others with the intention of avoiding the formation of an oxide film and enhancing the oxidation of the hydrogen atoms. If an oxide film forms and the sample gets passivated, this will work as a barrier for the diffusing hydrogen atoms. This was discovered experimentally by Manolatos et al [41], and is illustrated in Figure 20. This reduction of hydrogen flux is assumed to be caused by the recombination of molecular hydrogen or a buildup of hydrogen atoms at the exit side, as the oxidation process has proven to be slower on an iron

surface than on a Pd surface. The last case will mean that the concentration on the exit side is no longer zero, which is the assumption for diffusion analyses based on Fick's second law [41].
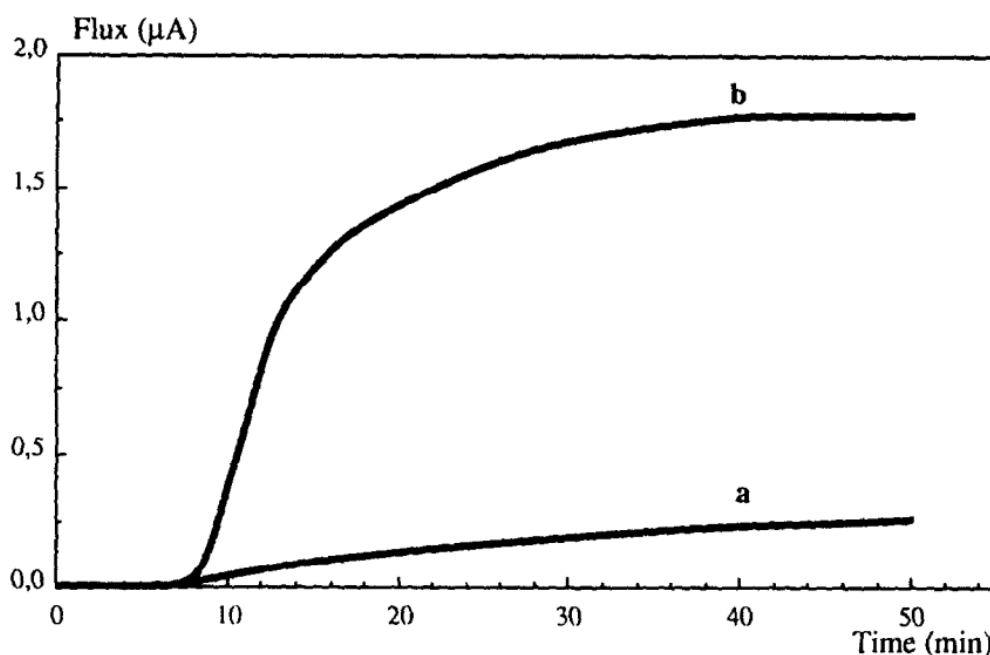
Figure 20: Hydrogen permeation current vs time measured without Pd (a) and with Pd (b) in 0,1N NaOH solution. It is evident that the passivation of the material when no Pd coating is applied severely lowers the permeation current. Obtained from [41].

However, due to the electrolyte used in this experimental work and its low solubility of oxygen, the formation of an oxide layer on the anodic side was not assumed to occur to an extent where it would affect the hydrogen permeation process. The anodic/oxidation side of the samples used in this work was therefore not coated with Pd, only grinded and polished to obtain similar surface condition as on the cathodic side.

3.4   Experimental procedure

After preparing the sample to be tested, it had to be mounted between the compartments in the cell. Electrical connection to the sample, which was the working electrode of the system, was ensured by a tiny screw going into the Kel-F sealing part. When tightened, the screw was in contact with the sample. The screw was connected to a wire, which made it easy to connect to the potentiostats. The POM nut was tightened manually to hold the two cells close together after the O-rings had been placed for sealing.

After the sample was in place and sealed, both compartments were filled with electrolyte (approximately 120 ml in each cell). This cell size is therefore in accordance with the ASTM standard [1] where it is stated that a ratio of volume of electrolyte to sample area of 20 *ml cm⁻²* is required. The counter electrodes were installed using a Pt-wire on each side coiled into a spring, and the reference electrodes were connected through capillaries mounted close to the sample. The setup was then submerged into a water bath which was covered with evaporation balls. The temperature in the water bath was set and given time to stabilize before proceeding. The Open Circuit Potential (OCP) was measured on each side. When achieving a steady state OCP, after approximately 1-2 hours, the testing could begin. First of all, a potentiodynamic sweep was executed on the anodic side, which gave nice polarization curves where e.g. the passive region could be identified. Since the two potentiostats were connected to the same working electrode (testing sample), it was important that the potentiostats could operate in floating condition.

In order to let out all diffusible hydrogen already present in the sample before startup, polarization of 0V vs Hg/Hg_2SO_4 was applied on the anodic side. This corresponds to approximately +450mV vs Ag/AgCl, and represents the passive area of both testing materials. The polarization curves for Fe3wt.%Si and X70 BM1 are shown in Appendix A. The applied anodic potential was kept constant throughout the test. After a steady state current was achieved on the anodic side (~24 hours), also known as the passive/background current, the first transient could be initiated. When finding the permeation current later on, the background current had to be accounted for.

3.4.1   Standard charge and discharge

When obtaining the transients in the standard way, the charging conditions were set and held constant until the total oxidation current on the anodic side of the system reached a steady state level.

To start the first transient, a constant charging current density of $-150\mu A\ cm^{-2}$ was impressed on the cathodic side. This value was determined during earlier project work [2] by pushing the charging current density as high as possible without hydrogen recombining into molecules and bubbles emerging in the cathodic cell. However, during the present work, the cathodic charging current density was also pushed to lower values to investigate the changes in the test results. This will be described in Section 4.1.3. The charging current density was applied until the measured current on the anodic side reached a new, steady state level. This level was a measure of the total oxidation current, which comprised both the background and the permeation current.

After achieving the total oxidation current, the discharge transient was initiated. This could be done in two ways. Method 1 involved reducing the cathodic charging current density to zero, i.e. applying nothing on the cathodic side, while the anodic polarization on the anodic side was kept constant at 0V vs Hg/Hg$_2$SO$_4$. The OCP on the cathodic side was continuously measured during the discharge transient, to make sure it attained and kept a steady level. The cathodic charging current density was kept at zero until the anodic background current again reached a steady state level and the diffusible hydrogen had diffused out. The first out of three total transients, consisting of both charge and discharge, was then finished. The subsequent transients were executed in the exact same way. This method has been utilized by several authors [3, 16, 17]. The second method, Method 2, involved polarizing anodically on both sides during discharge, not only on the anodic side. This has earlier been done by Smirnova, Hauge and Zakroczymski [15, 28, 36] among others. The method involved applying polarization of 0V vs. Hg/Hg$_2$SO$_4$ on the charging side during the discharge transient instead of applying nothing. This potential was kept constant on both sides until the background current was achieved on the anodic side. The latter transients were then performed in the same way. Method 1 will further be referred to as single anodic polarization between transients, while Method 2 will be referred to as double anodic polarization between transients.

3.4.2   Partial charge and discharge

In order to get a better picture of the real lattice diffusion in the material, an interesting thing to try was partial charge and discharge [31, 36]. This involved keeping the cathodic charging current density constant at -150$\mu A\ cm^{-2}$ until the total oxidation current had reached a steady state level, and then follow up by increasing the charging current density to -200$\mu A\ cm^{-2}$ instead of stopping the charging. This allowed the total oxidation current to reach a new steady state level. The part of the transient that was obtained after the charging current density was increased could then be analyzed. When initiating the partial discharge transient, the charging current density was reduced to -150$\mu A\ cm^{-2}$ again. The oxidation current was given time to stabilize at this charging level, meaning that some of the diffusible hydrogen was let out. The charging current density was then interrupted to let the rest of the diffusible hydrogen out and obtain the background current.

The values for the cathodic charging current densities are referred to as absolute values throughout this thesis, meaning that a charging current density of -200$\mu A\ cm^{-2}$ will be referred to as a higher charging current density than -150$\mu A\ cm^{-2}$.

3.5 Limitations

An immersion heater circulated the water in addition to heating it to obtain a steady temperature in the whole bath. However, this proved to be hard to accomplish for 25°C. When setting the heating device to this specific temperature, the temperature increased over time instead of remaining steady. This was probably because the device in itself produced some heat only by circulating the water, which caused the temperature to increase to some extent. This was not a problem for higher temperatures, as the heating produced only by circulating then became insignificant. The lowest temperature for testing was therefore 30°C, in order for the tests to be conducted at steady temperatures.

Originally, the plan was to run the tests at temperatures above 100°C. However, when examining the boiling point of the electrolyte, it was discovered that it started boiling at approximately 106°C. Therefore, the temperature never got pushed higher than 75°C.

Chapter 4

Results

In this chapter, the results from the testing on the different samples are shown. The software application for Iino's diffusion model [3-5] developed by Simonsen [6] was utilized for the data from the charging transients and compared to the results obtained by the standard t_{lag} method. Iino's diffusion model will further be referred to as the trapping model. For the discharge transients obtained according to Method 2, curve fitting of the model based on the Fourier solution of Fick's second law was utilized, in order to see if the D_{eff} found from the t_{lag} method for the charging transients could be verified for the discharge transients as well. This model will further be referred to as the discharge model.

The fit of the trapping model to the experimental data turned out to be hard in the cases where huge fluctuations (noise) were present in the experimental transients. The fitting software offered a possibility to remove noise, but in the most severe cases the fit of the model to the data became inaccurate after filtering away huge amounts of noise, or simply if the noise was too severe to be removed. Inaccurate fits of the model to the data are marked "poor fit" throughout this chapter. In Appendix C, the examples of a good and a poor fit are shown. The dimensionless fitting parameter κ was set to be constant in the software, meaning data on the irreversible trapping effects according to equation 2.37 will not be provided. The value of k_r [cm^3 sites^{-1} s^{-1}] was found in the literature for X65 steel [3]. This enabled the determination of N_r based on the dimensionless fitting parameter λ according to equation 2.41 for the X70 steel samples, which was interesting for comparative purposes. The value for λ is therefore only shown in the X70 steel results, Section 4.2.1-4.2.3. The value for p_r based on the dimensionless fitting parameter μ according to equation 2.42 was not calculated in this chapter due to lacking basis for comparison. Therefore, the value for μ is not shown for either of the materials.

The D_{eff} from the best fit of the Fourier solution Fick's second law, Fick's model, to the charging transients is not shown in this chapter, only the D_{eff} calculated by the t_{lag} method. The results from the t_{lag} method turned out to show a fairly similar accuracy. The discharge transients shown in Section 4.1.2 in this chapter are from between charging transient 1 and 2 and between transient 2 and 3 for each test.

For the X70 BM1 (0% strain) sample tested at 75°C, partial charge and discharge was also utilized.

For determining the Arrhenius lines shown in this chapter, the values for D_{eff} found from the trapping model for the standard charging transients were used as they were assumed to represent

36

a more reliable result. The calculated values based on the Arrhenius line determined by the D_{eff} from the t_{lag} method are shown in Chapter 5 and Chapter 6 for comparative purposes. The calculated N_r values based on equation 2.41 for the X70 high strength steel samples are shown in this chapter, but as they deviated a lot from the Arrhenius results, they were not taken into further consideration.

Due to a limited amount of time, X70 BM2 (1% strain) was only tested at one temperature. Also, a full microstructural investigation of all the samples unfortunately turned out to be too time consuming.

4.1   Fe 3wt.% Si

The first material to be tested was the pure ferritic material Fe-3wt.%Si. This was tested at three different temperatures with the main purpose of calibrating the equipment. For this purpose the diffusion coefficient D_{eff} and sub-surface hydrogen concentration C_0 were calculated, and the Arrhenius line was estimated by regression to determine N_r, the number of reversible traps, and the binding energy for the reversible traps E_b. As the temperature was increased, drastical changes happened to the results. The permeation current I_{ss} and diffusion coefficient D_{eff} increased, which is in accordance with the Arrhenius equation 2.23. The corrosion potential/OCP of the system decreased when the temperature was increased. For many of the recorded charging transients, the measured permeation current decreased after a maximum current had been achieved.

The testing was executed according to both Method 1: single anodic polarization between transients, and Method 2: double anodic polarization between transients. The discharge model was applied for Method 2. The boundary conditions of the model, namely C=0 at both sides of the sample, was then assumed to be fulfilled during discharge due to the immediate oxidation of hydrogen atoms on both sides as they were both under anodic polarization.

In addition, a range of different cathodic charging current densities was applied to examine the effect on the results. A total of two different samples were used throughout this testing, meaning that each sample was used for several tests in a row before taking it out of the cell. The samples are numbered 1 and 2.

4.1.1 Method 1: Single anodic polarization between transients

Before discovering the limitations of the heating device, the first test was executed at 25°C. The main problem turned out to be that the permeation current never stabilized, it increased continuously. As it was discovered that the permeation current increased significantly with increasing temperature, the reason for the constant increase in current might have been that the temperature increased slightly because of the heaters lacking ability to keep the temperature steady at 25°C. The results obtained at this temperature were therefore discarded, meaning that the very first charging transient obtained on this sample is not reported in this section. In other words, none of the transients reported on this sample are assumed to show signs of irreversible trapping. The results from the t_{lag} method are shown in Table 5. The resulting charging transients plotted in a normalized flux vs. dimensionless time plot together with Fick's curve for lattice diffusion are shown in Figure 21, Figure 22 and Figure 23.

Table 5: Results for Fe 3wt.% Si when polarizing only on the anodic side between transients. I_{ss} denotes the anodic steady state permeation current. D_{eff} from charge transient calculated using equation 2.22 and C_0 calculated using equation 2.26, based on D_{eff} from equation 2.22.

Sample no.	Trans. No.	i_c [μA cm^{-2}]	t_{lag} [s]	I_{ss} [μA]	D_{eff} [m^2 s^{-1}] [Charge - t_{lag}]	C_0 [ppm W]
1	1, 30°C	-150	4569	0,26	$3,77 \cdot 10^{-11}$	$2,17 \cdot 10^{-2}$
1	2, 30°C	-150	4326	0,23	$3,98 \cdot 10^{-11}$	$1,75 \cdot 10^{-2}$
1	3, 30°C	-150	4152	0,21	$4,14 \cdot 10^{-11}$	$1,58 \cdot 10^{-2}$
1	1, 50°C	-150	2856	0,31	$6,02 \cdot 10^{-11}$	$1,59 \cdot 10^{-2}$
1	2, 50°C	-150	2700	0,29	$6,37 \cdot 10^{-11}$	$1,40 \cdot 10^{-2}$
1	3, 50°C	-150	2226	0,48	$7,73 \cdot 10^{-11}$	$1,88 \cdot 10^{-2}$
1	1, 75°C	-150	1317	1,71	$1,31 \cdot 10^{-10}$	$3,99 \cdot 10^{-2}$
1	2, 75°C	-150	1749	1,68	$9,84 \cdot 10^{-11}$	$5,20 \cdot 10^{-2}$
1	3, 75°C	-150	1995	1,75	$8,62 \cdot 10^{-11}$	$6,18 \cdot 10^{-2}$

The parameters determined by the trapping model are shown in Table 6.

Table 6: D_{eff} found by curve fitting of equation 2.43, the trapping model. C_0 calculated using equation 2.26 based on D_{eff} from trapping model.

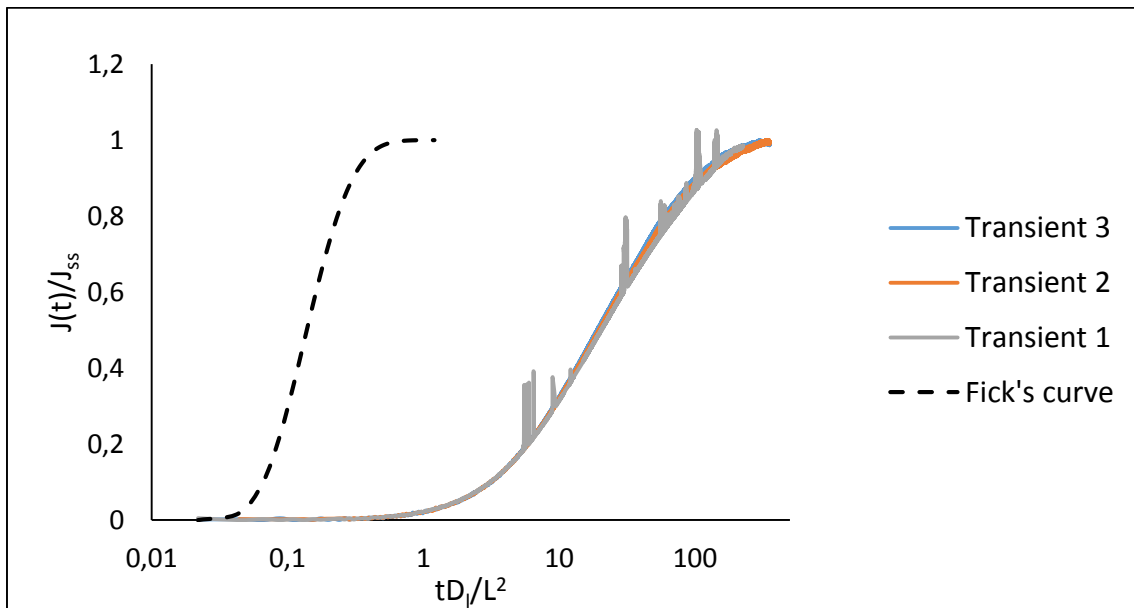| Sample no.	Trans. no.	D_{eff} [m^2 s^{-1}] [Charge – Iino]	C_0 [ppm W]
1	1, 30°C	$1{,}76 \cdot 10^{-10}$	$4{,}65 \cdot 10^{-3}$
1	2, 30°C	$1{,}69 \cdot 10^{-10}$	$4{,}13 \cdot 10^{-3}$
1	3, 30°C	$1{,}76 \cdot 10^{-10}$	$3{,}71 \cdot 10^{-3}$
2	1, 50°C	$2{,}97 \cdot 10^{-10}$	$3{,}23 \cdot 10^{-3}$
2	2, 50°C	$3{,}33 \cdot 10^{-10}$	$2{,}67 \cdot 10^{-3}$
2	3, 50°C	Poor fit	-
3	1, 75°C	$6{,}94 \cdot 10^{-10}$	$7{,}51 \cdot 10^{-3}$
3	2, 75°C	$5{,}71 \cdot 10^{-10}$	$8{,}96 \cdot 10^{-3}$
3	3, 75°C	$4{,}75 \cdot 10^{-10}$	$1{,}12 \cdot 10^{-2}$

Figure 21: Normalized permeation flux for charging transients at 30°C. Single anodic polarization between transients.
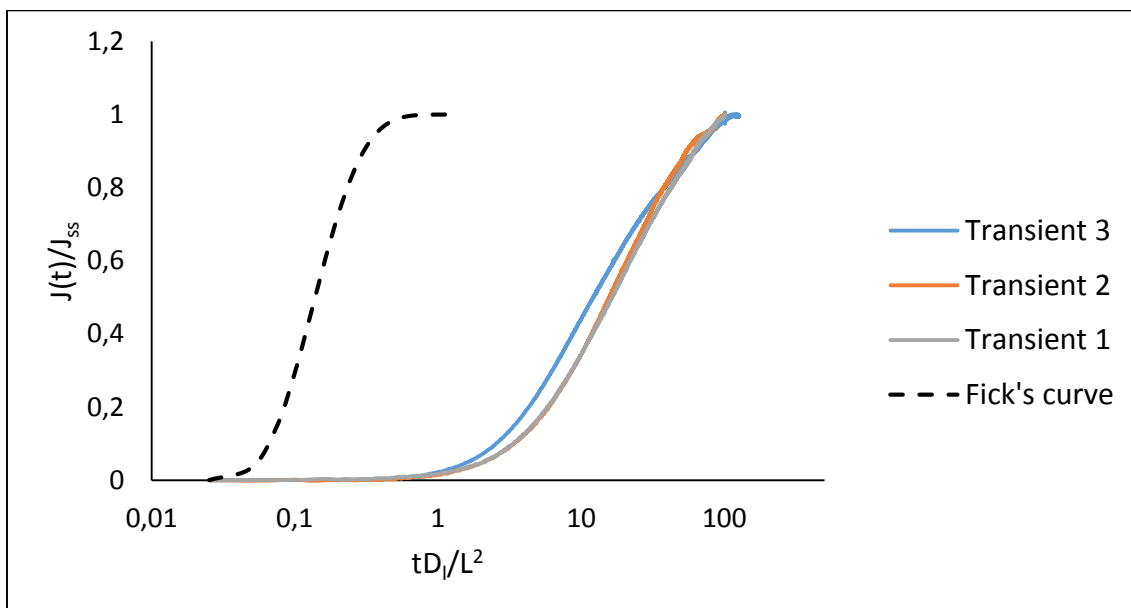
Figure 22: Normalized permeation flux for charging transients at 50˚C. Single anodic
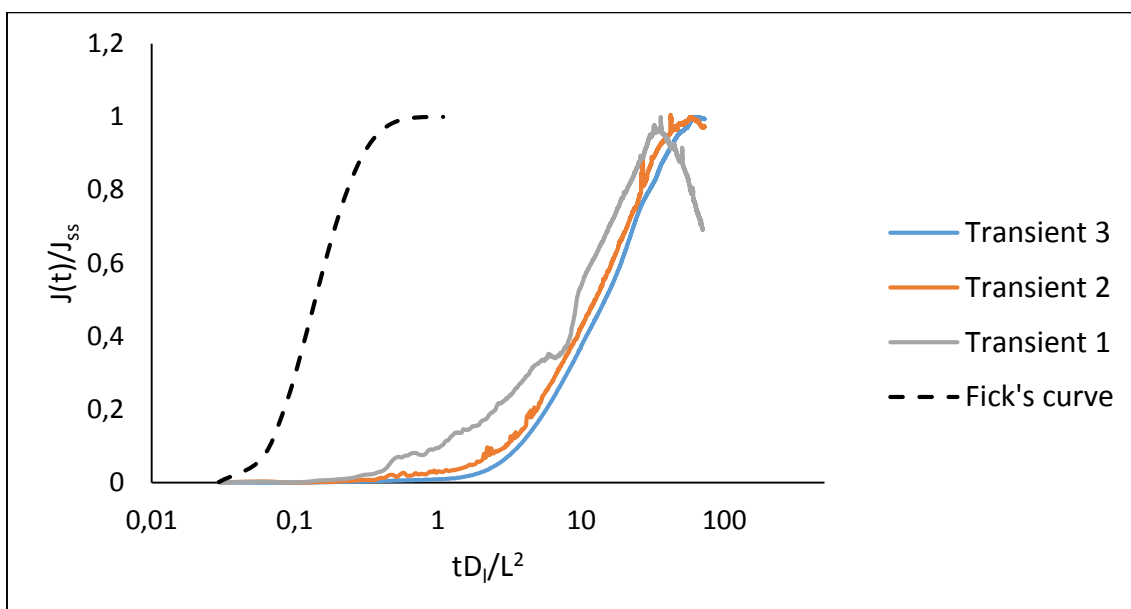polarization between transients.

Figure 23: Normalized permeation flux for charging transients at 75˚C. Single anodic
polarization between transients.

The transients obtained look fairly similar, which is plausible given the fact that the same sample was used throughout the testing and the effects of irreversible trapping was assumed to be absent. When looking at the fit of the Fourier solution of Fick's second law and the trapping model to the charging transients, it was clear that the trapping model gave the better fit. The curve fitting of Fick's second law gave a result quite similar to the result from the t_{lag} method, which is why only the result from the t_{lag} method is reported in this chapter. This is illustrated in Figure 24.
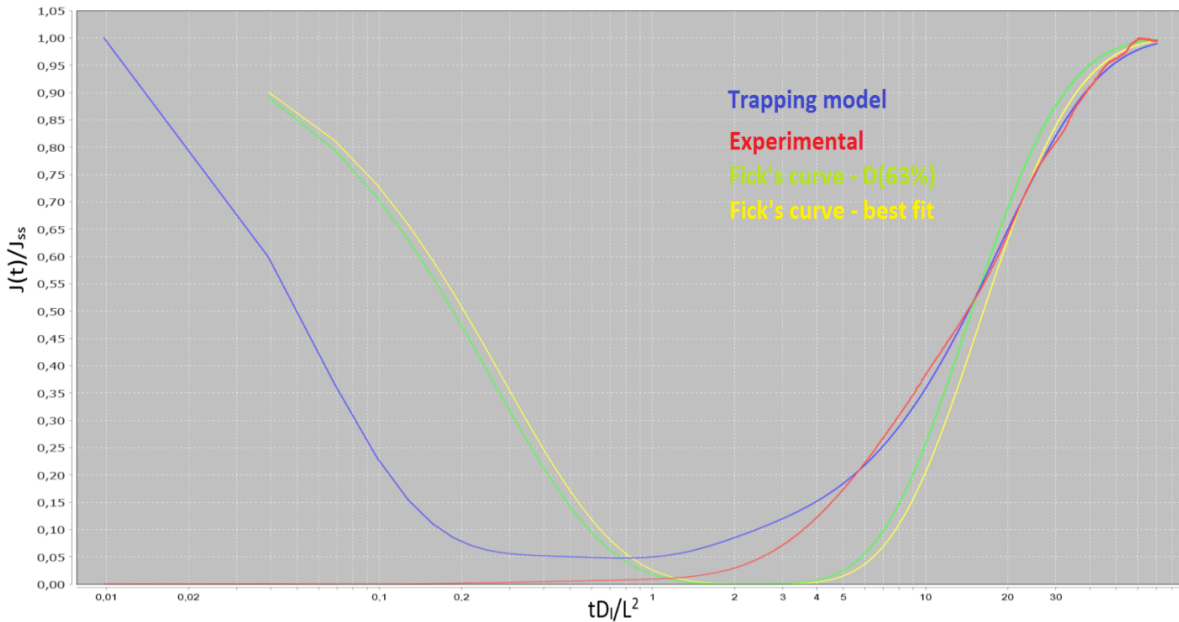

Figure 24: Trapping model (blue line) fits well with the experimental transient (red line). The yellow line represents the best possible fit of Fick's curve to the experimental curve, while the green line represents Fick's curve for the D_{eff} calculated by the t_{lag} method. Graph obtained from the software developed by Simonsen [6].

To estimate the number of reversible traps, N_r, and binding energy, E_b, for the material, the D_{eff} from the charging transients was plotted against the inverse of the absolute temperature multiplied by a factor of 1000, (1000/T). By regression, an exponential line was fitted to the scatter plot [15, 28]. The D_{eff} from all three transients at each temperature could be used to determine the Arrhenius line because of the absence of irreversible trapping effects as mentioned above. The upper line in Figure 25 represents the D_{eff} values determined by the trapping model, while the lower line represents the D_{eff} values determined by the t_{lag} method. The line representing the trapping model was the basis for the calculations of N_r and E_b, given that the trapping model gave more accurate results as shown in Figure 24.
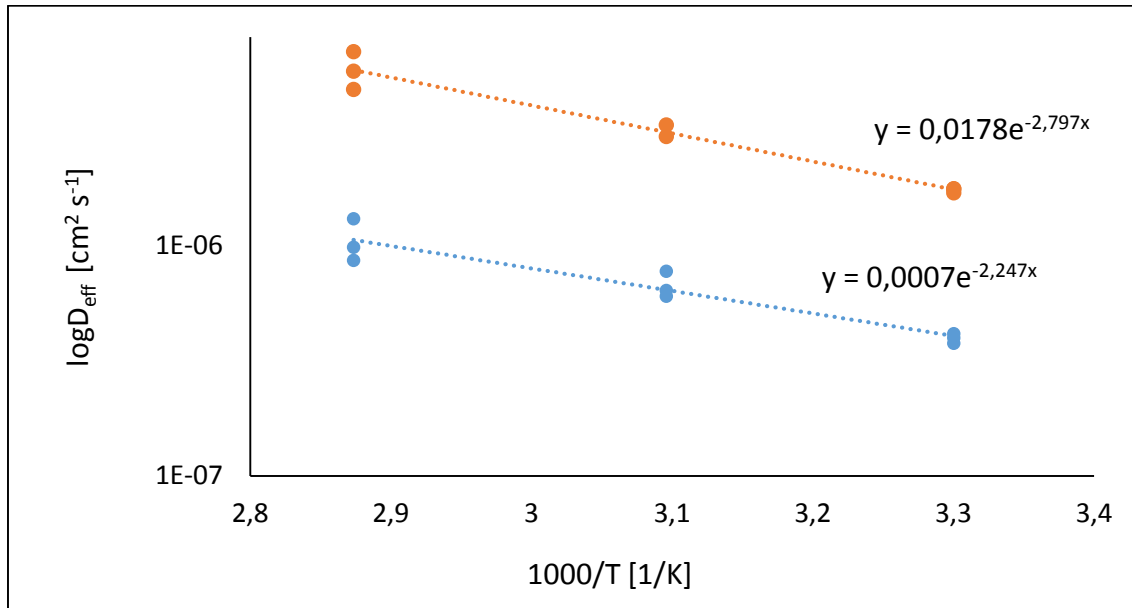
Figure 25: Scatter plot of D_{eff} vs. (1000/T). Regression used for estimating the Arrhenius line.

The equation for the line estimated by regression was fitted into equation 2.23 in order for the lattice activation energy, E_l, to be derived.

$$D_{eff} = D_0\exp(\frac{-E_l}{RT}) \qquad (2.23)$$

This gives a lattice activation energy, E_l, of 23,25 $kJ\ mol^{-1}$. Equation 2.23 then changes to:

$$D = 0,0178\exp(\frac{-23,25kJmol^{-1}}{RT}) \qquad (4.1)$$

By fitting this into equation 2.30, the density of reversible traps, N_r, can be found.

$$D_0\frac{N_l}{N_r} = 0,0178 \qquad (4.2)$$

$$Nr = \frac{7,23\ x\ 10^{-4}\ x\ 5,23\ x\ 10^{23}}{0,0178} = 2,12\ x\ 10^{22}\ sites\ cm^{-3}$$

The binding energy for the reversible is found by subtracting the energy needed for hydrogen atoms to make a jump between two lattice sites in a ferritic lattice:

$$E_b = 23,25\ kJmol^{-1} - 5,69\ kJmol^{-1} = 17,56\ kJ\ mol^{-1} \qquad (4.3)$$

4.1.2 Method 2: Double anodic polarization between transients

When testing according to Method 2, the results changed to some extent. The background current achieved between the transients was lower than for the testing done according to Method 1. The steady state permeation current I_{ss} generally got higher, and the t_{lag} decreased. This resulted in D_{eff} increasing slightly. The sub-surface concentration C_0 was relatively unaffected. The testing was still done on the same sample, i.e. it was not taken out of the cell between the tests. The application of an anodic potential on the cathodic side of the sample during discharge enabled the measurement of the discharge current on this side as well as on the anodic side. The discharge current measured on the cathodic side decreased much faster than the current measured on the anodic side for all the tests reported in this section independent of temperature, in addition to the current on the cathodic side being much higher when initiating the discharge. This led to inaccurate fits of the discharge model to the discharge curve on the cathodic side, which is why only the D_{eff} obtained from the discharge transient on the anodic side is shown. The discharge transients are shown in Appendix B in a plot of normalized current vs. time due to the huge difference in current in the beginning of the discharge. The results from the t_{lag} method and discharge model are shown in Table 7. The resulting charging transients plotted in a normalized flux vs. dimensionless time plot together with Fick's curve for lattice diffusion are shown in Figure 26, Figure 27 and Figure 28.

Table 7: Results for Fe 3wt.% Si when polarizing on both sides between transients. I_{ss} denotes the anodic steady state permeation current. D_{eff} from charge transient calculated using equation 2.22 and C_0 calculated using equation 2.26, based on D_{eff} from equation 2.22. D_{eff} from discharge transient determined by curve fitting of equation 2.45.

Sample no.	Trans. No.	i_c [μA cm^{-2}]	t_{lag} [s]	I_{ss} [μA]	D_{eff} [m^2 s^{-1}] [Charge - t_{lag}]	D_{eff} [m^2 s^{-1}] [Discharge anod.side- Fick]	C_0 [ppm W]
1	1, 30°C	-150	2193	0,36	$7,85 \cdot 10^{-11}$	$\sim 3,50 \cdot 10^{-10}$	$1,41 \cdot 10^{-2}$
1	2, 30°C	-150	2262	0,33	$7,61 \cdot 10^{-11}$	$\sim 2,50 \cdot 10^{-10}$	$1,32 \cdot 10^{-2}$
1	3, 30°C	-150	2202	0,32	$7,81 \cdot 10^{-11}$	-	$1,26 \cdot 10^{-2}$
1	1, 50°C	-150	1170	1,28	$1,47 \cdot 10^{-10}$	$\sim 5,00 \cdot 10^{-10}$	$2,66 \cdot 10^{-2}$
1	2, 50°C	-150	1110	1,17	$1,55 \cdot 10^{-10}$	$\sim 5,00 \cdot 10^{-10}$	$2,30 \cdot 10^{-2}$
1	3, 50°C	-150	1176	1,09	$1,46 \cdot 10^{-10}$	-	$2,27 \cdot 10^{-2}$
1	1, 75°C	-150	444	4,20	$3,88 \cdot 10^{-10}$	$\sim 8,50 \cdot 10^{-10}$	$3,31 \cdot 10^{-2}$
1	2, 75°C	-150	552	3,38	$3,12 \cdot 10^{-10}$	$\sim 8,00 \cdot 10^{-10}$	$3,31 \cdot 10^{-2}$
1	3, 75°C	-150	660	3,33	$2,61 \cdot 10^{-10}$	-	$3,90 \cdot 10^{-2}$

The parameters determined by the trapping model are shown in Table 8.

Table 8: D_{eff} found by curve fitting of equation 2.43, the trapping model. C_0 calculated using equation 2.26 based on D_{eff} from trapping model.

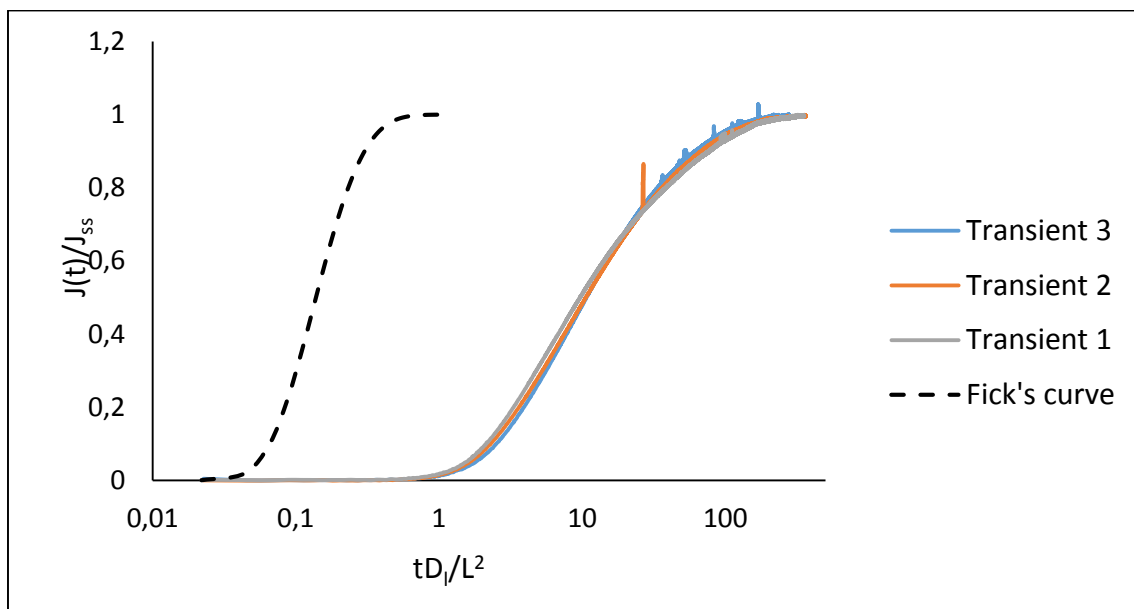| Sample no.	Trans. no.	Deff [m² s⁻¹] [Charge – Iino]	C₀ [ppm W]
1	1, 30°C	$2,97 \cdot 10^{-10}$	$3,71 \cdot 10^{-3}$
1	2, 30°C	$3,17 \cdot 10^{-10}$	$3,18 \cdot 10^{-3}$
1	3, 30°C	$3,28 \cdot 10^{-10}$	$2,99 \cdot 10^{-3}$
2	1, 50°C	$6,14 \cdot 10^{-10}$	$6,38 \cdot 10^{-3}$
2	2, 50°C	$6,45 \cdot 10^{-10}$	$5,54 \cdot 10^{-3}$
2	3, 50°C	$5,73 \cdot 10^{-10}$	$5,80 \cdot 10^{-3}$
3	1, 75°C	$1,75 \cdot 10^{-9}$	$7,32 \cdot 10^{-3}$
3	2, 75°C	Poor fit	-
3	3, 75°C	$8,61 \cdot 10^{-10}$	$1,18 \cdot 10^{-2}$

Figure 26: Normalized permeation flux for charging transients at 30°C. Double anodic polarization between transients.
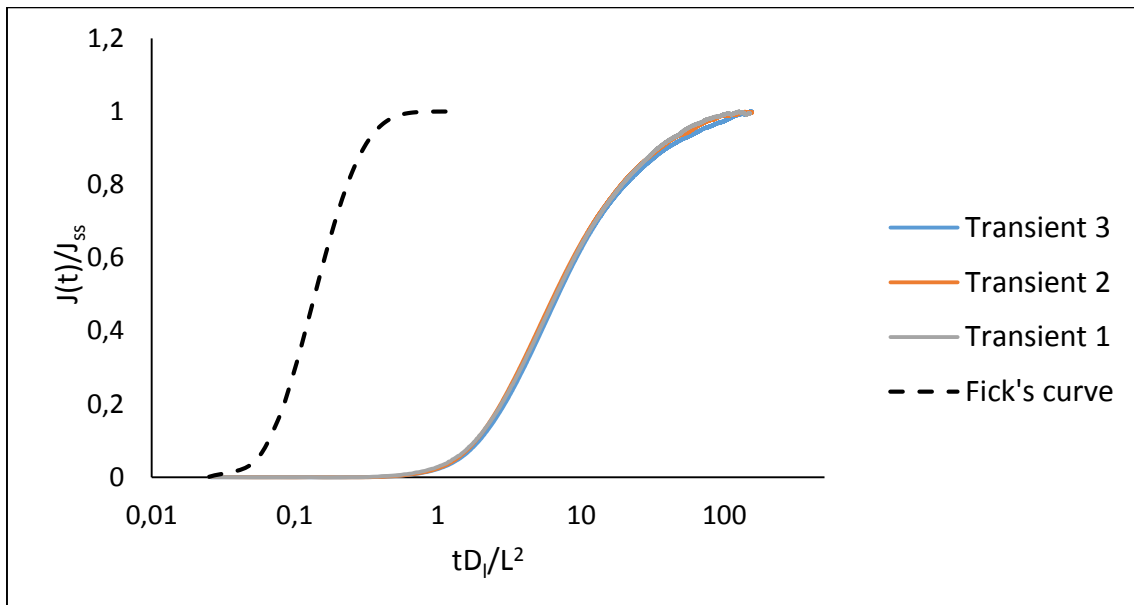
Figure 27: Normalized permeation flux for charging transients at 50°C. Double anodic polarization between transients.
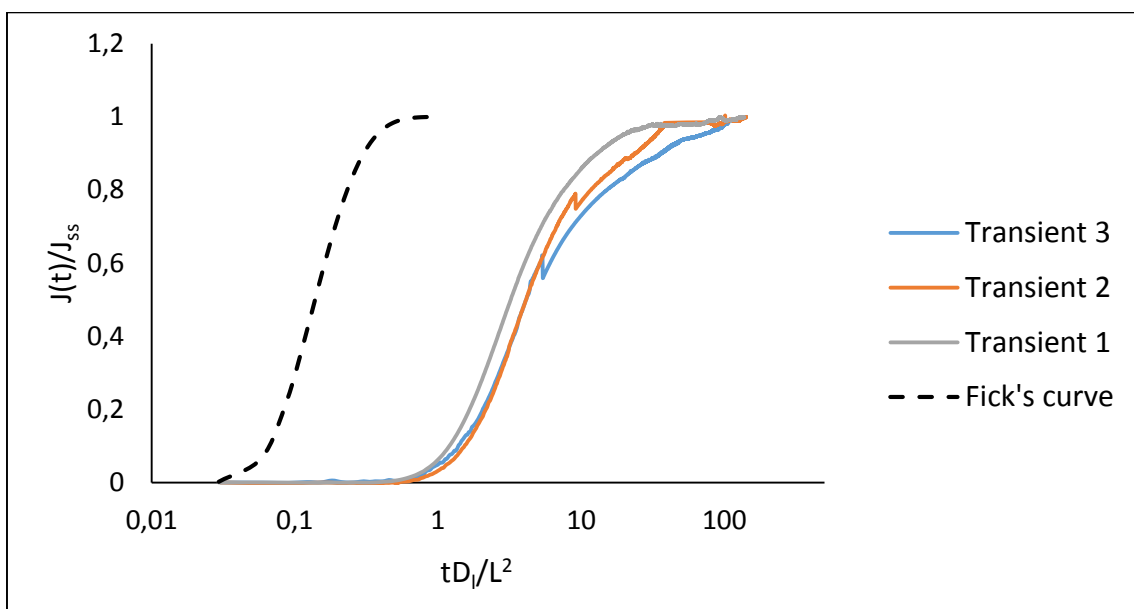

Figure 28: Normalized permeation flux for charging transients at 75°C. Double anodic polarization between transients.

When determining N_r and E_b from the Arrhenius line, the D_{eff} values from the trapping model were considered. No effects of irreversible trapping affected the calculated D_{eff}, meaning the D_{eff} from all three transients at each temperature could be used to determine the Arrhenius line. The upper line in Figure 29 represents the D_{eff} values determined by the trapping model, while the lower line represents the D_{eff} values determined by the t_{lag} method. The further calculations are based on the trapping model values.
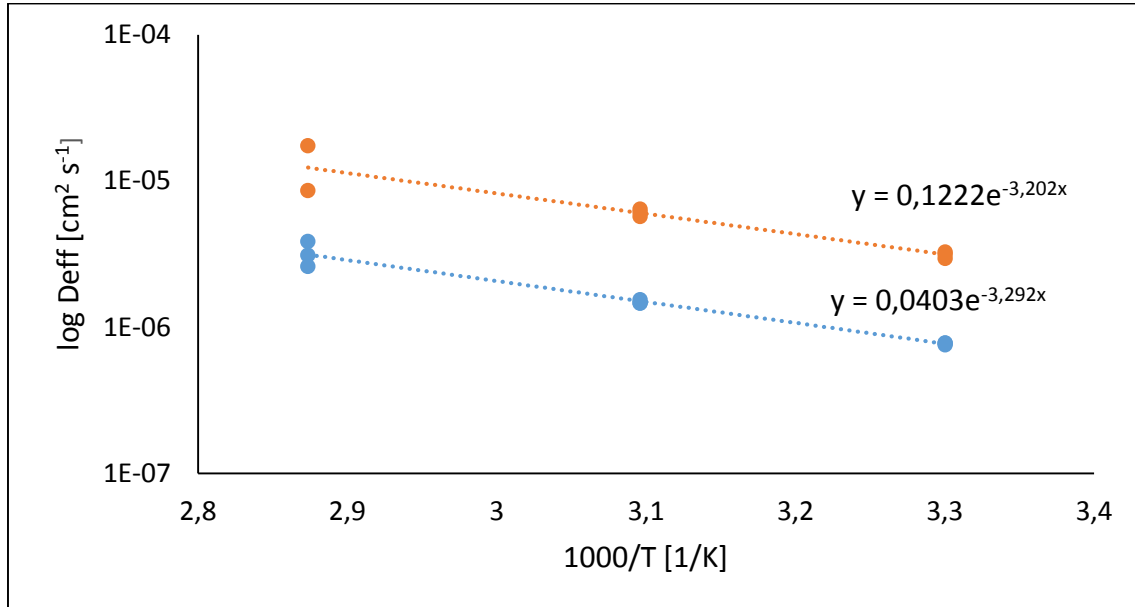
Figure 29: Scatter plot of D_{eff} vs. (1000/T). Regression used for estimating the Arrhenius line.

$$D_{eff} = D_0 \exp(\frac{-E_l}{RT}) \tag{2.23}$$

This gives a lattice activation energy, E_l, of 26,62 $kJ\ mol^{-1}$. Equation (2.23) then changes to:

$$D = 0,1222 \exp(\frac{-26,62 kJmol^{-1}}{RT}) \tag{4.4}$$

By fitting this into equation (2.30), the density of reversible traps, N_r, can be found.

$$D_0 \frac{N_l}{N_r} = 0,1222 \tag{4.5}$$

$$Nr = \frac{7,23\ x\ 10^{-4}\ x\ 5,23\ x\ 10^{23}}{0,1222} = 3,09\ x\ 10^{21}\ sites\ cm^{-3}$$

The binding energy for the reversible traps becomes:

$$E_b = 26,62\ kJmol^{-1} - 5,69\ kJmol^{-1} = 20,93\ kJ\ mol^{-1} \tag{4.6}$$

When testing according to Method 2, the trap density N_r got lower compared to Method 1. The binding energy for the traps E_b got higher compared to the values calculated for Method 1.

When taking the sample out after doing three transients on three different temperatures with double anodic polarization between transients, it was discovered that the electrolyte on the cathodic side had turned into a yellow colour and a matt surface had developed on the cathodic side of the sample. As the water bath was covered with evaporation balls, the cell could not be visually examined during testing and the exact time for the pollution of the electrolyte was therefore not known. In other words, it could have happened during any of the transients. The examination of the cathodic surface of the sample and the examination of the polluted electrolyte are described in Section 4.3 and 4.4, respectively. Because of this unwanted happening in the cathodic cell, a new sample was used for further testing. The chosen method for further testing was Method 1, in order to eliminate Method 2 as a possible reason for the unwanted happening in the cathodic cell, even though the reason for the unwanted reaction had not been determined at this point.

4.1.3   Varying the charging current density

In previous project work [2], the applied cathodic charging current density was varied between -130 $\mu A\ cm^{-2}$ and -250$\mu A\ cm^{-2}$. The chosen charging current density for testing was then -150$\mu A\ cm^{-2}$, as mentioned in Section 3.4.1.

However, charging current densities lower than -130$\mu A\ cm^{-2}$ were never applied during the previous project work. Therefore, in order to examine the effect of imposing a lower charging current density, -100$\mu A\ cm^{-2}$, -50 $\mu A\ cm^{-2}$ and -10 $\mu A\ cm^{-2}$ were charged with to see if the results were affected. In order to get fairly fast transients, the transients were obtained at 50°C. A charging current density of -10 $\mu A\ cm^{-2}$ was charged with at 30°C as well to get the results from the highest and lowest charging current density at different temperatures, with the highest charging current density being -150 $\mu A\ cm^{-2}$ as reported in section 4.1.1. Method 1, i.e. single anodic polarization between transients, was utilized here because of the unwanted happening in the cathodic cell during the testing according to Method 2. Unfortunately, the laboratory computer crashed during the first transient causing loss of data. Trapping effects that can only be observed in the very first transient will therefore not be investigated in this section, since all the tests were executed on the very same sample.

The results from the t_{lag} method are shown in Table 9. The resulting charging transients plotted in a normalized flux vs. dimensionless time plot together with Fick's curve for lattice diffusion are shown in Figure 30, Figure 31 and Figure 32.

Table 9: Results for Fe 3wt.% Si when varying the charging current density. I_{ss} denotes the anodic steady state permeation current. D_{eff} from charge transient calculated using equation 2.22 and C_0 calculated using equation 2.26, based on D_{eff} from equation 2.22.

Sample no.	Trans. No.	i_c [µA cm^{-2}]	t_{lag} [s]	I_{ss} [µA]	D_{eff} [m^2 s^{-1}] [Charge - t_{lag}]	C_0 [ppm W]
2	1, 50°C	-100	2232	0,63	$6,63 \cdot 10^{-11}$	$2,69 \cdot 10^{-2}$
2	2, 50°C	-100	4257	0,68	$3,48 \cdot 10^{-11}$	$5,54 \cdot 10^{-2}$
2	3, 50°C	-100	4545	0,58	$3,26 \cdot 10^{-11}$	$5,05 \cdot 10^{-2}$
2	1, 50°C	-50	2949	0,76	$5,02 \cdot 10^{-11}$	$4,31 \cdot 10^{-2}$
2	2, 50°C	-50	2532	0,60	$5,85 \cdot 10^{-11}$	$2,93 \cdot 10^{-2}$
2	3, 50°C	-50	2529	0,68	$5,85 \cdot 10^{-11}$	$3,31 \cdot 10^{-2}$
2	1, 50°C	-10	3138	0,16	$4,72 \cdot 10^{-11}$	$9,85 \cdot 10^{-2}$
2	2, 50°C	-10	3594	0,15	$4,12 \cdot 10^{-11}$	$1,03 \cdot 10^{-2}$
2	3, 50°C	-10	4542	0,15	$3,26 \cdot 10^{-11}$	$1,26 \cdot 10^{-2}$
2	1, 30°C	-10	7065	0,05	$2,10 \cdot 10^{-11}$	$6,33 \cdot 10^{-3}$
2	2, 30°C	-10	5931	0,04	$2,50 \cdot 10^{-11}$	$4,23 \cdot 10^{-3}$
2	3, 30°C	-10	6546	0,04	$2,26 \cdot 10^{-11}$	$4,77 \cdot 10^{-3}$

The parameters determined by the trapping model are shown in Table 10.

Table 10: Values found by curve fitting of equation 2.43, the trapping model. C_0 calculated using equation 2.26 based on D_{eff} from trapping model.

Sample no.	Trans. no.	i_c [µA cm^{-2}]	D_{eff} [m^2 s^{-1}] [Charge – Iino]	C_0 [ppm W]
2	1, 50°C	-100	$2,56 \cdot 10^{-10}$	$6,99 \cdot 10^{-3}$
2	2, 50°C	-100	$1,38 \cdot 10^{-10}$	$1,39 \cdot 10^{-2}$
2	3, 50°C	-100	$1,73 \cdot 10^{-10}$	$9,52 \cdot 10^{-3}$
2	1, 50°C	-50	$2,44 \cdot 10^{-10}$	$8,87 \cdot 10^{-3}$
2	2, 50°C	-50	$2,98 \cdot 10^{-10}$	$5,75 \cdot 10^{-3}$
2	3, 50°C	-50	$2,65 \cdot 10^{-10}$	$7,31 \cdot 10^{-3}$
2	1, 50°C	-10	$2,96 \cdot 10^{-10}$	$1,57 \cdot 10^{-3}$
2	2, 50°C	-10	$1,93 \cdot 10^{-10}$	$2,20 \cdot 10^{-3}$
2	3, 50°C	-10	$3,12 \cdot 10^{-10}$	$1,31 \cdot 10^{-3}$
2	1, 30°C	-10	$8,29 \cdot 10^{-11}$	$1,60 \cdot 10^{-3}$
2	2, 30°C	-10	$1,00 \cdot 10^{-10}$	$1,05 \cdot 10^{-3}$
2	3, 30°C	-10	$9,41 \cdot 10^{-11}$	$1,15 \cdot 10^{-3}$

Figure 30: Normalized permeation flux for charging transients at 50°C. Single anodic polarization between transients. Charging current density of -100μA cm^{-2}.

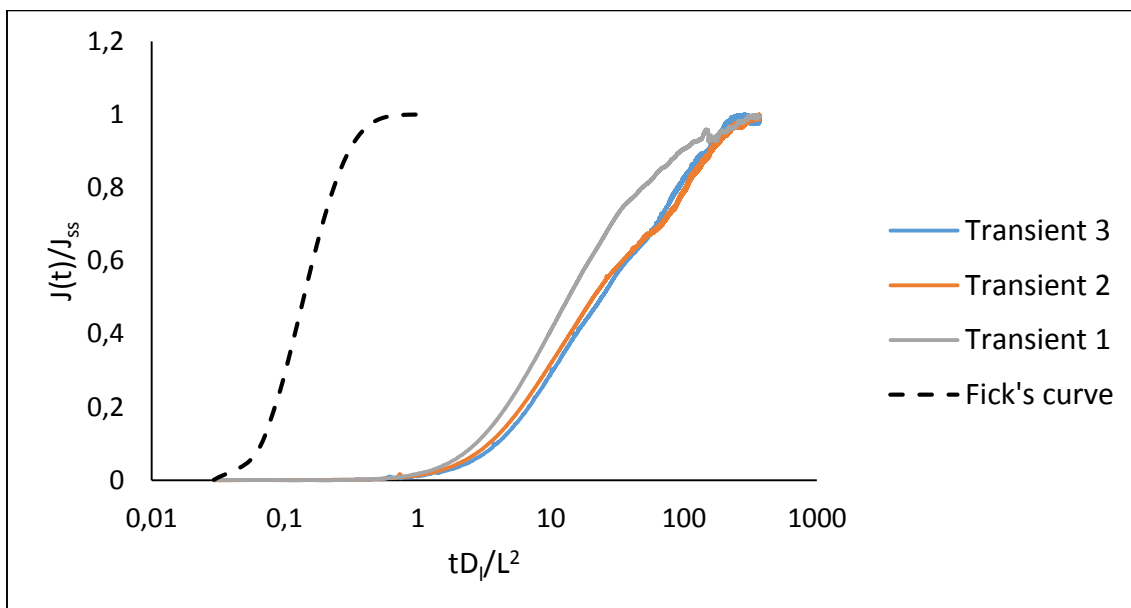
Figure 31: Normalized permeation flux for charging transients at 50°C. Single anodic polarization between transients. Charging current density of -50μA cm^{-2}.

Figure 32: Normalized permeation flux for charging transients at 50˚C. Single anodic polarization between transients. Charging current density of -10μA cm^{-2}.
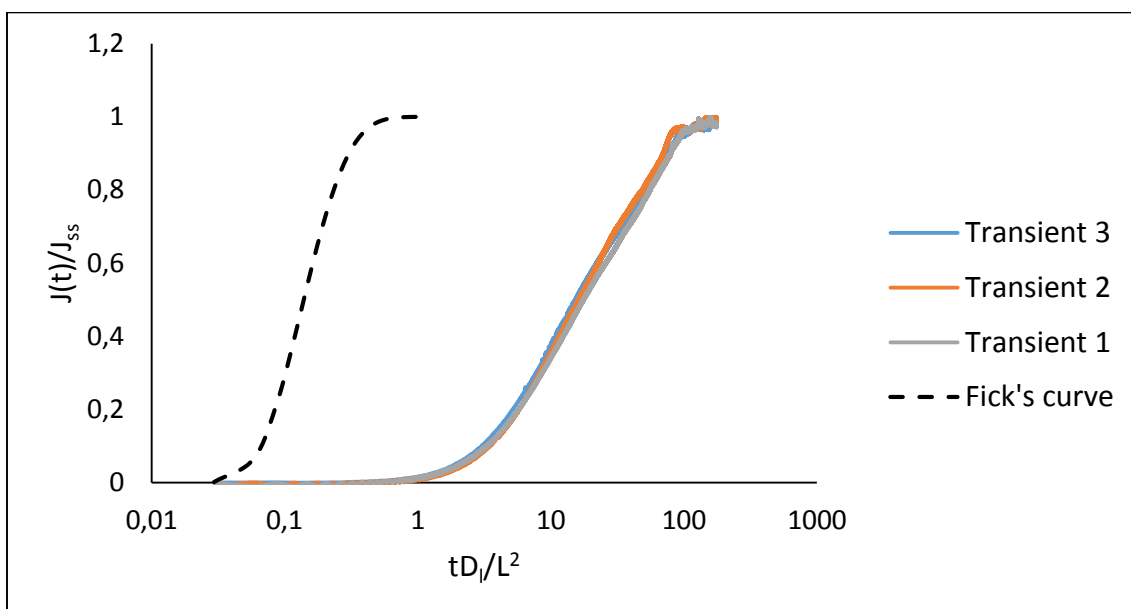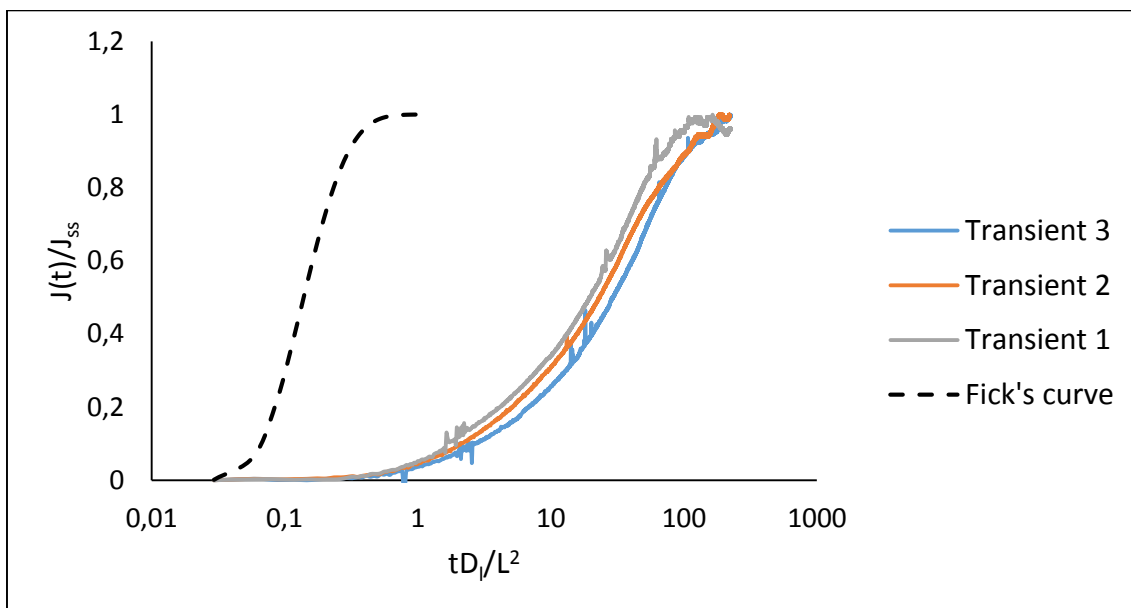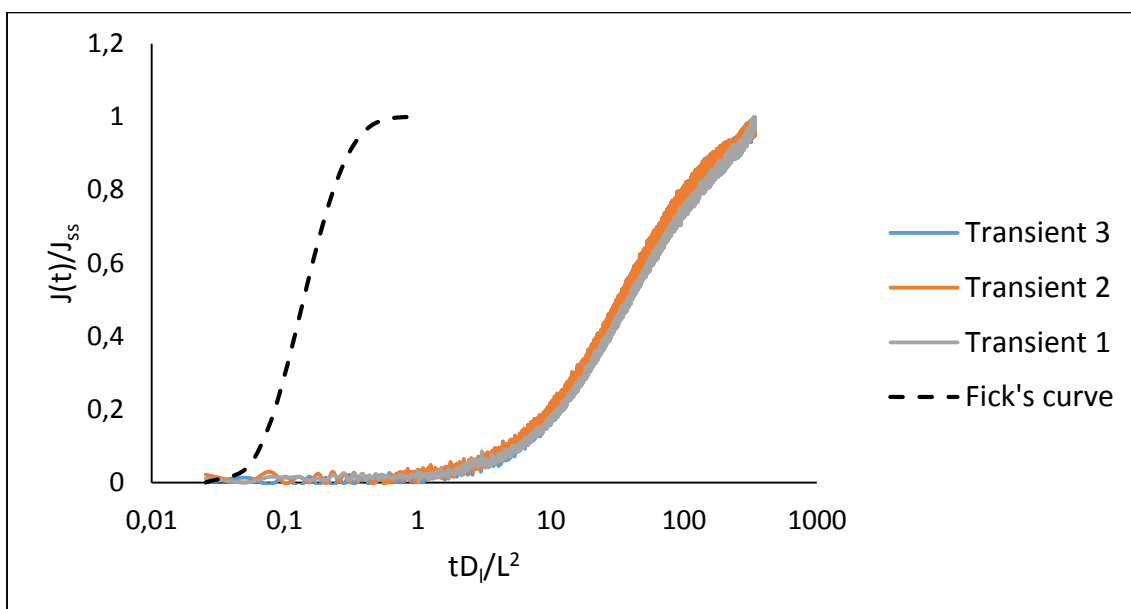

Figure 33: Normalized permeation flux for charging transients at 30°C. Single anodic polarization between transients. Charging current density of -10μA cm^{-2}.

By lowering the cathodic charging current density, the steady state permeation current decreased significantly when the current density was lowered to $-10 \mu A \ cm^{-2}$. When this charging value was applied at 30°C, the permeation current never really got stabile, it increased continuously.

Another limitation occurred in this case. When applying these low currents, the potentiostat started showing a "Control Amp" overload condition on the cathodic charging side. The overload condition was most likely a result of the potentiostat oscillating at such low currents, which made this an unwanted incident. In attempt to avoid this, the potentiostat current range was made less sensitive [42]. Unfortunately, this was not sufficient, with the overload condition still occurring even with a less sensitive current range. The overload condition in addition to the issue with the permeation current never getting stabile for the lowest applied charging current density, $-10 \mu A \ cm^{-2}$, were essential reasons for why this charging current density was not chosen for further testing.

The diffusion coefficient on the other hand, did not vary drastically when charging with different current densities. However, the results for the charging current density of $-150 \ \mu A \ cm^{-2}$ reported in Section 4.1.1 varied slightly from the other results reported in this section by other means. The permeation current was lower than for both $-100 \ \mu A \ cm^{-2}$ and $-50 \ \mu A \ cm^{-2}$ charging at 30°C and 50°C. The sub-surface concentration, C_0, at 50°C was also lower than C_0 for both $-100 \ \mu A \ cm^{-2}$ and $-50 \ \mu A \ cm^{-2}$ charging. This is illustrated in Figure 34 and Figure 35. As mentioned, the sample charged with $-150 \mu A \ cm^{-2}$, sample 1, was a different sample than for the rest of the tests reported in this section, sample 2. That opens the possibility for differences related to testing conditions, surface conditions etc.

The determining factor for the choice of the charging current density to be used for further testing was the problem with the potentiostat. The "CA overload" condition caused by the low charging currents was difficult to overcome with the short amount of time available. This overload condition actually occurred periodically for the charging current densities as high as $-100 \ \mu A \ cm^{-2}$. Given that fact, the charging current density of $-150 \mu A \ cm^{-2}$ was chosen for further testing.

As the tests reported in this section were obtained in order to see the effect of varying the cathodic charging current density, they are not included in any comparisons or conclusive remarks in later sections. The purpose was mainly to choose a proper cathodic charging current density for further testing.

D_{eff} and C_0 shown in Figure 34 and Figure 35 were obtained by the trapping model, and the values shown are from the third transient for each test. The results from 30°C and 50°C reported in Section 4.1.1 are included. However, for the test on 50°C reported in Section 4.1.1, the third

transients provided a poor fit to the trapping model. For this test, the results from the second transient is shown.
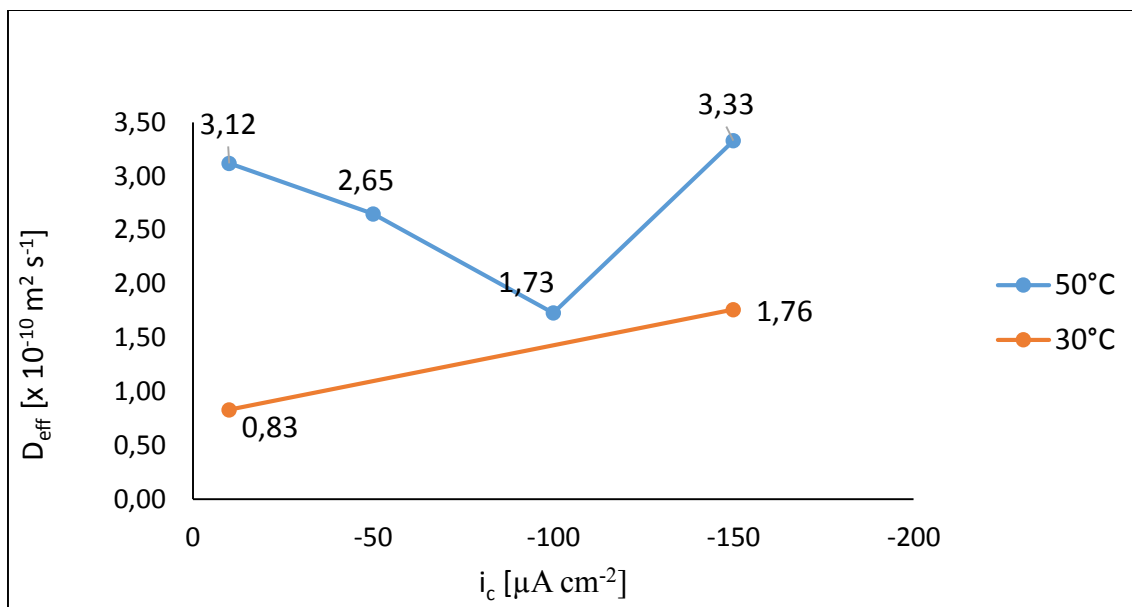

Figure 34: D_{eff} found by curve fitting of equation 2.43, the trapping model.
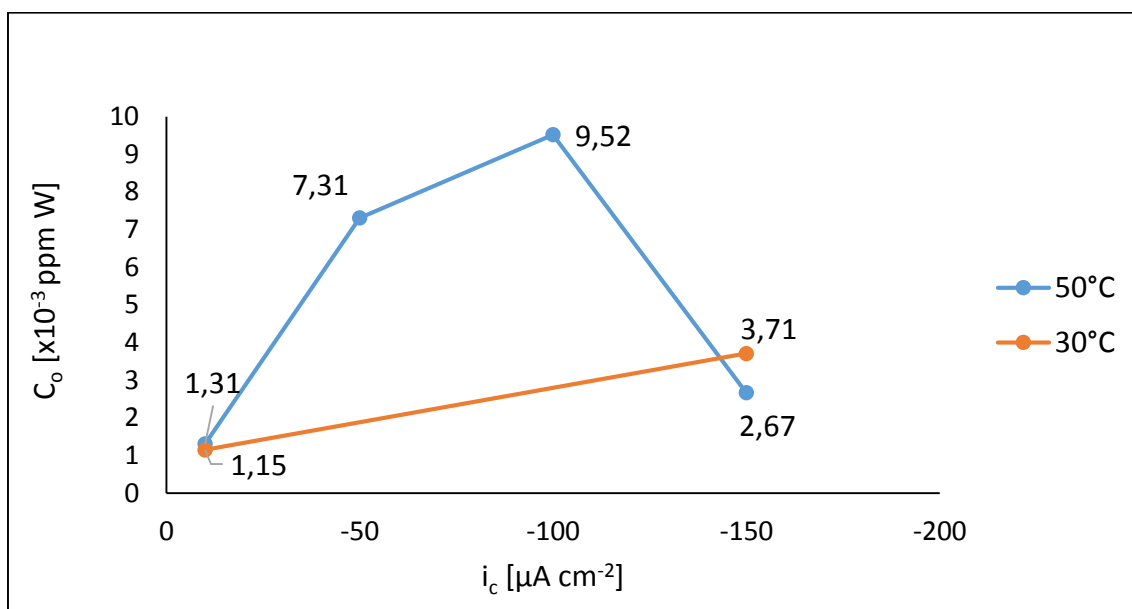

Figure 35: C_0 calculated using equation 2.26 based on D_{eff} from trapping model.

4.2　X70 high strength steel

The second material to be tested was X70 high strength steel. The samples to be tested had different degrees of pre-straining, and included both base metal (BM) and heat affected zone (HAZ) samples. BM1 and HAZ1 had not been deformed, while BM2 was deformed to a level of 1% strain. To examine the effect of irreversible trapping that can be seen in the very first charging transient, a new sample was used for each new test. The samples are numbered 1-3, and three transients were conducted on each sample. The samples were tested at three different temperatures, enabling the determination of the Arrhenius line to determine N_r and E_b. The same trend as for Fe3wt.%Si was seen when increasing the temperature, namely an increased I_{ss} and D_{eff}. The measured permeation current also decreased after a maximum current had been achieved for many of the transients reported in this section as well.

All the testing on this material was executed according to Method 1, single anodic polarization between transients. The discharge model was therefore not applied to evaluate the transients, as the boundary condition C=0 on the cathodic surface could not be assumed to be true. The immediate oxidation of the hydrogen atoms was only happening on the anodic surface.

A cathodic charging current density of $-150\mu A \ cm^{-2}$ was applied on the charging side for all the tests reported in this section.

4.2.1　BM1 (0% strain)

When testing BM1 at 75°C, huge fluctuations in the permeation transients compromised the results. The test on 75°C was therefore executed a second time. The results shown in this section are from the second test on 75°C, as the permeation transients were unquestionably better than for the first test on 75°C. The results from the t_{lag} method are shown in Table 11. The resulting charging transients plotted in a normalized flux vs. dimensionless time plot together with Fick's curve for lattice diffusion are shown in Figure 36, Figure 37 and Figure 38.

Table 11: Results for X70 BM1 when polarizing only on the anodic side between transients. I_{ss} denotes the anodic steady state permeation current. D_{eff} from charge transient calculated using equation 2.22 and C_0 calculated using equation 2.26, based on D_{eff} from equation 2.22.

Sample no.	Trans. no.	i_c [μA cm^{-2}]	t_{lag} [s]	I_{ss} [μA]	D_{eff} [m^2 s^{-1}] [Charge - t_{lag}]	C_0 [ppm W]
1	1, 30°C	-150	3474	0,77	$2,01 \cdot 10^{-10}$	$2,36 \cdot 10^{-2}$
1	2, 30°C	-150	3186	0,68	$2,19 \cdot 10^{-10}$	$1,92 \cdot 10^{-2}$
1	3, 30°C	-150	3264	0,59	$2,14 \cdot 10^{-10}$	$1,69 \cdot 10^{-2}$
2	1, 50°C	-150	681	2,61	$9,58 \cdot 10^{-10}$	$1,62 \cdot 10^{-2}$
2	2, 50°C	-150	966	1,55	$6,75 \cdot 10^{-10}$	$1,37 \cdot 10^{-2}$
2	3, 50°C	-150	1245	1,64	$5,24 \cdot 10^{-10}$	$1,86 \cdot 10^{-2}$
3	1, 75°C	-150	1086	4,32	$6,29 \cdot 10^{-10}$	$4,18 \cdot 10^{-2}$
3	2, 75°C	-150	900	3,05	$7,59 \cdot 10^{-10}$	$2,45 \cdot 10^{-2}$
3	3, 75°C	-150	693	3,10	$9,85 \cdot 10^{-10}$	$1,91 \cdot 10^{-2}$

The parameters determined by the trapping model are shown in Table 12. Fallahmohammadi [3] reported that $k_r = 9,9 \cdot 10^{-17}$ *cm^3 sites^{-1} s^{-1}* for X65 high strength steel, which was assumed to be applicable to X70 steel as well. By knowing this value, the density of reversible trapping sites, N_r, could be calculated according to equation 2.41.

Table 12: Values found by curve fitting of equation 2.43, the trapping model. C_0 calculated using equation 2.26 based on D_{eff} from trapping model. N_r calculated using equation 2.41.

| Sample no.	Trans. no.	D_{eff} [m^2 s^{-1}] [Charge – Iino]	λ	N_r [sites cm^{-3}]	C_0 [ppm W]
1	1, 30°C	$8,59 \cdot 10^{-10}$	12,00	$2,49 \cdot 10^{13}$	$5,50 \cdot 10^{-3}$
1	2, 30°C	$8,47 \cdot 10^{-10}$	10,00	$2,04 \cdot 10^{13}$	$4,95 \cdot 10^{-3}$
1	3, 30°C	$8,70 \cdot 10^{-10}$	10,00	$2,10 \cdot 10^{13}$	$4,16 \cdot 10^{-3}$
2	1, 50°C	$5,22 \cdot 10^{-9}$	8900,00	$1,20 \cdot 10^{17}$	$2,98 \cdot 10^{-3}$
2	2, 50°C	$4,77 \cdot 10^{-9}$	118,0	$1,45 \cdot 10^{15}$	$1,94 \cdot 10^{-3}$
2	3, 50°C	$1,55 \cdot 10^{-9}$	4,00	$1,60 \cdot 10^{13}$	$6,27 \cdot 10^{-3}$
3	1, 75°C	$1,29 \cdot 10^{-9}$	4,00	$1,27 \cdot 10^{13}$	$2,03 \cdot 10^{-2}$
3	2, 75°C	$3,69 \cdot 10^{-9}$	13,00	$1,18 \cdot 10^{14}$	$5,04 \cdot 10^{-3}$
3	3, 75°C	$4,53 \cdot 10^{-9}$	15,00	$1,68 \cdot 10^{14}$	$4,16 \cdot 10^{-3}$
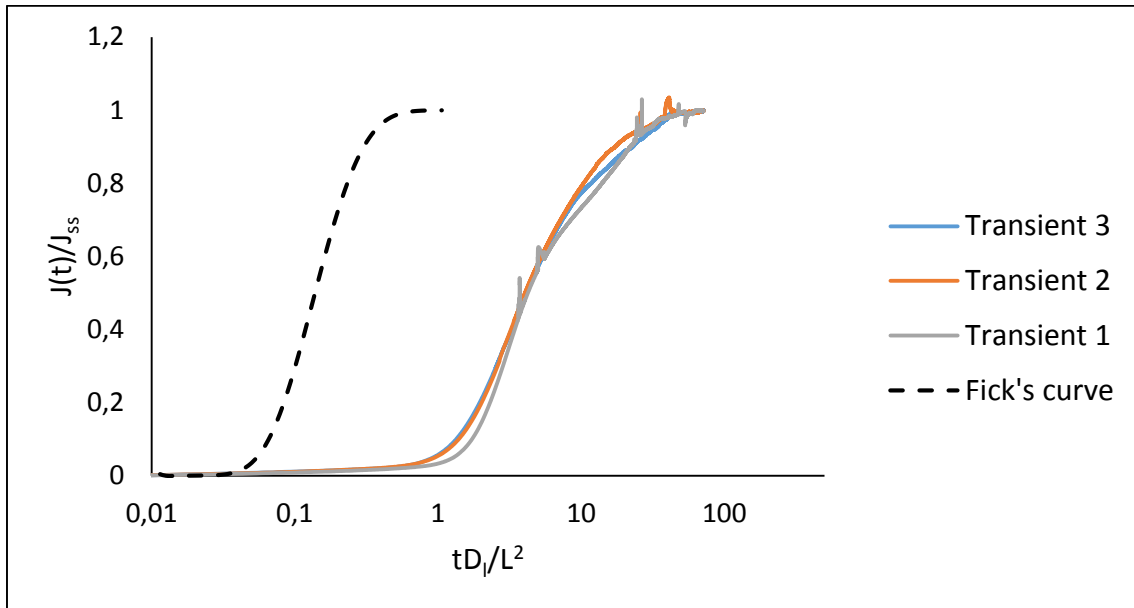
Figure 36: Normalized permeation flux for charging transients at 30°C, sample 1. Single anodic polarization between transients.
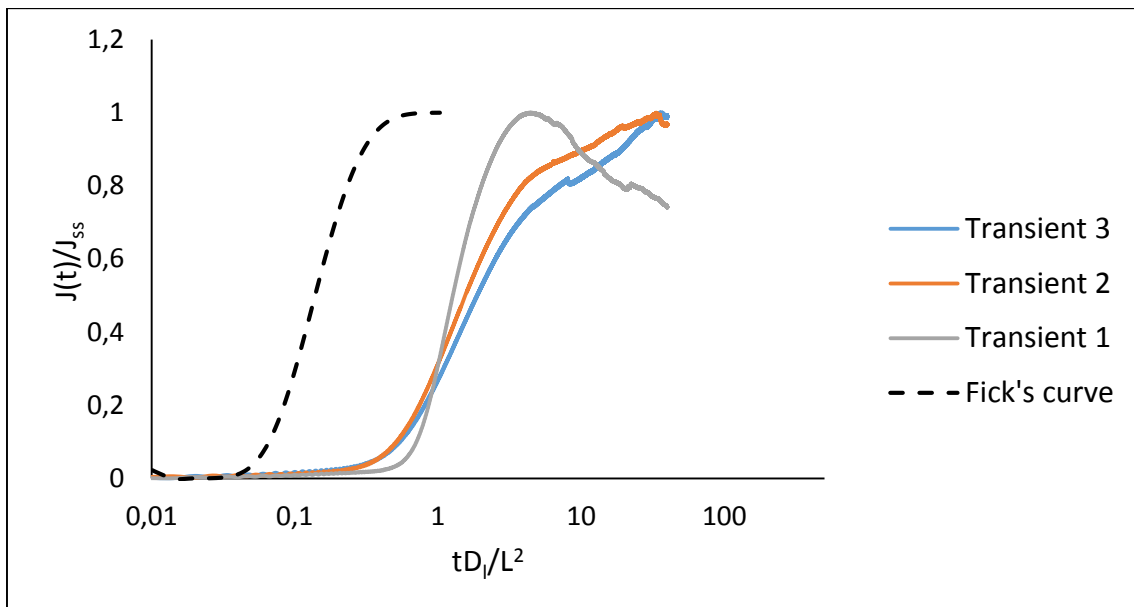

Figure 37: Normalized permeation flux for charging transients at 50°C, sample 2. Single anodic polarization between transients.
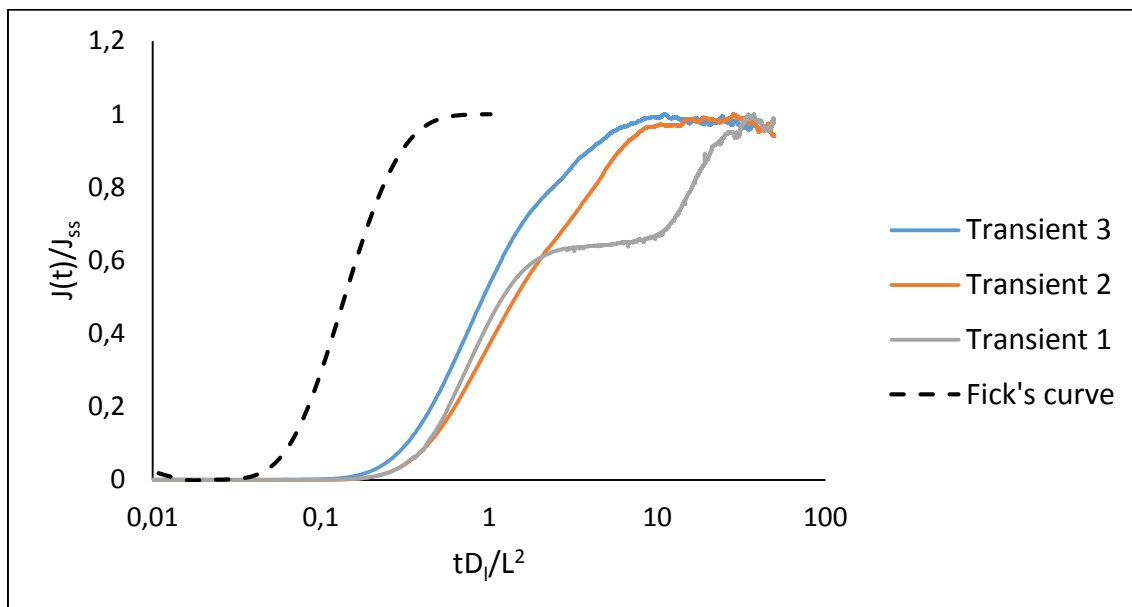
Figure 38: Normalized permeation flux for charging transients at 75°C, sample 3. Single anodic polarization between transients.

For tests executed at 30°C and 50°C, an increased break through time for the first transient could be detected. This indicated the presence of irreversible traps. For the test at 75°C, the first transient had a unique shape, the so-called "double plateau" as mentioned in Section 2.7.1, and no increased break through time could be detected compared to the second transient. This behaviour was also seen for the HAZ1 and BM2 samples, and the phenomenon will be further described in Section 4.2.2.

When running the test at 75°C, the partial charge and discharge method as described in Section 3.4.2 was also tested to see if the assumption that the traps should get saturated and that lattice diffusion would be the dominating mechanism during the transients was valid. Due to the fact that the partial discharge transient was obtained when still applying a charging current density on the cathodic side, the discharge model was not applied to evaluate the partial discharge transients as the concentration on the cathodic surface was not zero. The D_{eff} determined by the t_{lag} method was calculated by stating that $J(0)=I(0)=0$, where t=0s is the starting time for the partial charge transient. Table 13 shows the D_{eff} determined by the t_{lag} method and trapping model for the partial charge transients.

Table 13: Results for the partial charge transients.

Partial transient no.	I_c [μA cm^{-2}]	I_{ss} [μA]	D_{eff} [m^2 s^{-1}] [Partial charge - t_{lag}]	D_{eff} [m^2 s^{-1}] [Partial charge - Iino]
1, 75˚C	-150 -200 -150	0,365	$7{,}11 \cdot 10^{-10}$	Poor fit
2, 75˚C	-150 -200 -150	0,391	$9{,}29 \cdot 10^{-10}$	$4{,}47 \cdot 10^{-9}$
3, 75˚C	-150 -200 -150	0,265	$1{,}16 \cdot 10^{-9}$	$1{,}80 \cdot 10^{-9}$

It was generally found that the partial charging transient provided a better fit to Fick's curve than the standard charging transient. The standard and partial charging transients from transient 3 are shown in Figure 39 and Figure 40.
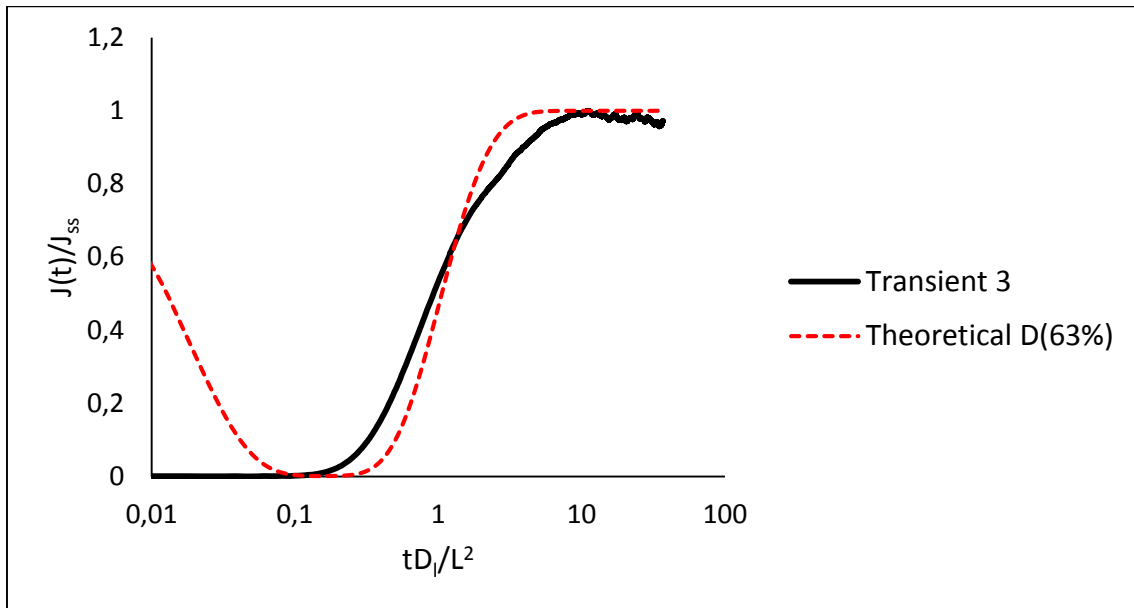
Figure 39: Standard charging transient plotted together with the theoretical Fick's curve based on the D_{eff} found by the t_{lag} method.
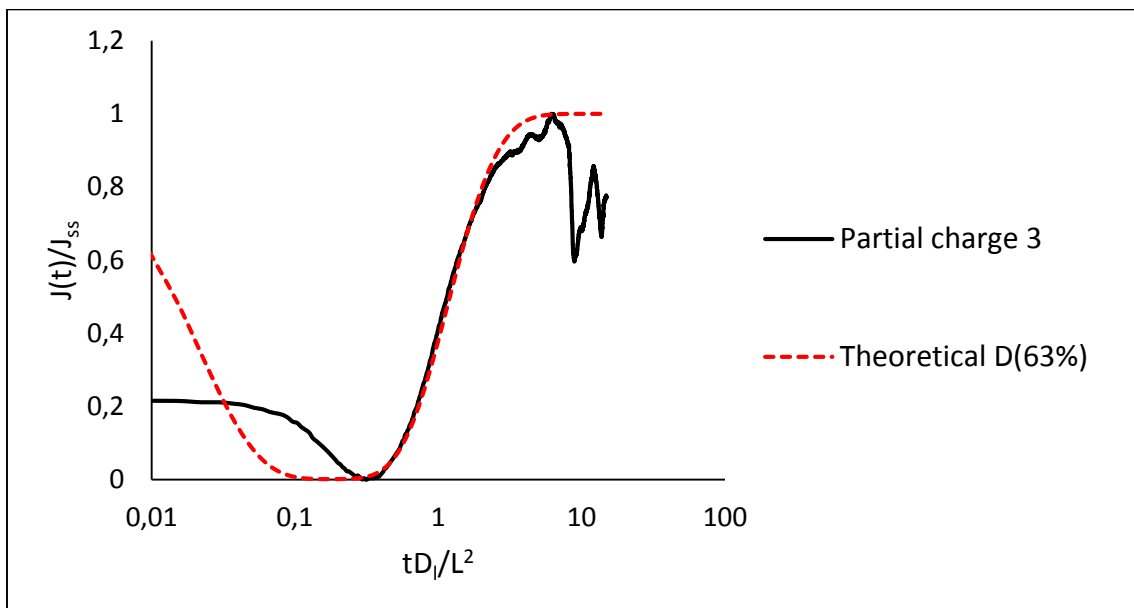

Figure 40: Partial charging transient plotted together with the theoretical Fick's curve based on the D_{eff} found by the t_{lag} method.

When determining the Arrhenius line for BM1, only the third standard charging transient from each temperature was taken into consideration in order to be sure to avoid the effects of irreversible trapping. The upper line in Figure 41 represents the D_{eff} values determined by the trapping model, while the lower line represents the D_{eff} values determined by the t_{lag} method. The further calculations are based on the trapping model values.
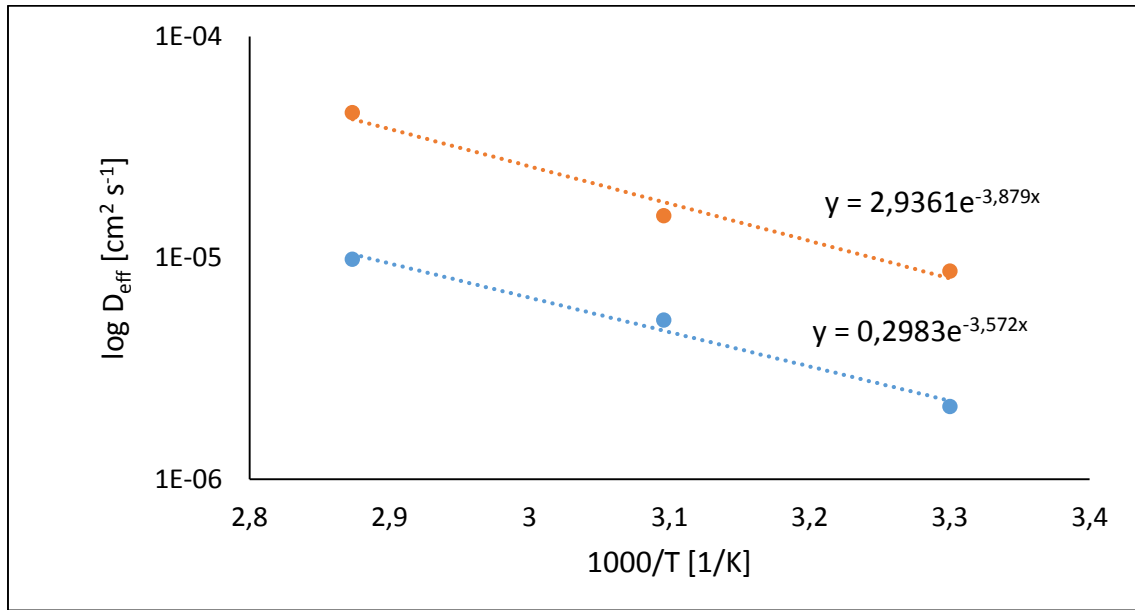
Figure 41: Scatter plot of D_{eff} vs. (1000/T). Regression used for estimating the Arrhenius line.

$$D_{eff} = D_0 \exp(\frac{-E_l}{RT}) \tag{2.23}$$

This gives a lattice activation energy, E_l, of 32,25 $kJ\ mol^{-1}$. Equation (2.23) then changes to:

$$D = 2,9361(\frac{-32,25kJmol^{-1}}{RT}) \tag{4.7}$$

By fitting this into equation 2.30, the density of reversible traps, N_r, can be found.

$$D_0\frac{N_l}{N_r} = 2,9361 \tag{4.8}$$

$$Nr = \frac{7,23\ x\ 10^{-4}\ x\ 5,23\ x\ 10^{23}}{2,9361} = 1,29\ x\ 10^{20}\ sites\ cm^{-3}$$

The binding energy for the reversible traps becomes:

$$E_b = 32,25\ kJmol^{-1} - 5,69\ kJmol^{-1} = 26,56\ kJ\ mol^{-1} \tag{4.9}$$

N_r calculated by Arrhenius equation 2.23 was higher than the N_r calculated by the equation 2.41. For the standard charging transient, N_r varied between $1,60 \cdot 10^{13} - 1,68 \cdot 10^{14}\ sites\ cm^{-3}$ according

to equation 2.41. The N_r calculated for transient 1 and 2 at 50°C was disregarded in this context because of its unexpected large value compared to the other calculated values.

4.2.2   HAZ1 (0% strain)

When testing BM1 prior to HAZ1, the transients at 75°C showed severe fluctuations as mentioned in Section 4.2.1. As this was highly undesirable, the cause for the fluctuations had to be found and eliminated before further testing. Therefore, after testing HAZ1 at 30°C, transients at 50°C and 75°C were also obtained continuously on the same sample to see if the fluctuations still occurred in order to avoid compromising new samples. The main suspicion for the current fluctuations was either fluctuations in the water bath temperature or noise picked up from the heating device itself. The temperature was therefore logged when testing sample 1 at 75°C to see if fluctuations in the temperature could be a cause. The results from the t_{lag} method are shown in Table 14. Figure 42 to Figure 46 show all the resulting transients plotted in a normalized flux vs. dimensionless time plot together with Fick's curve for lattice diffusion.

Table 14: Results for X70 HAZ1. I_{ss} denotes the anodic steady state permeation current. D_{eff} from charge transient calculated using equation 2.22 and C_0 calculated using equation 2.26, based on D_{eff} from equation 2.22.

Sample no.	Trans. no.	i_c [μA cm^{-2}]	t_{lag} [s]	I_{ss} [μA]	D_{eff} [m^2 s^{-1}] [Charge - t_{lag}]	C_0 [ppm W]
1, 30°C	1	-150	3948	1,12	$1,75\cdot10^{-10}$	$3,91\cdot10^{-2}$
1, 30°C	2	-150	6120	1,03	$1,13\cdot10^{-10}$	$5,58\cdot10^{-2}$
1, 30°C	3	-150	6594	1,08	$1,05\cdot10^{-10}$	$6,29\cdot10^{-2}$
1, 50°C	1	-150	5748	2,61	$1,20\cdot10^{-10}$	$1,33\cdot10^{-1}$
1, 50°C	2	-150	4050	2,81	$1,71\cdot10^{-10}$	$1,01\cdot10^{-1}$
1, 50°C	3	-150	2631	2,67	$2,63\cdot10^{-10}$	$6,23\cdot10^{-2}$
1, 75°C	1	-150	1137	6,37	$6,08\cdot10^{-10}$	$6,42\cdot10^{-2}$
1, 75°C	2	-150	999	5,34	$6,92\cdot10^{-10}$	$4,73\cdot10^{-2}$
1, 75°C	3	-150	918	4,70	$7,53\cdot10^{-10}$	$3,82\cdot10^{-2}$
2, 50°C	1	-150	4647	1,57	$1,43\cdot10^{-10}$	$6,58\cdot10^{-2}$
2, 50°C	2	-150	7158	1,95	$0,93\cdot10^{-10}$	$1,26\cdot10^{-1}$
2, 50°C	3	-150	7695	2,01	$0,86\cdot10^{-10}$	$1,40\cdot10^{-1}$
3, 75°C	1	-150	5322	3,71	$1,29\cdot10^{-10}$	$1,75\cdot10^{-1}$
3, 75°C	2	-150	1323	3,02	$5,18\cdot10^{-10}$	$3,54\cdot10^{-2}$
3, 75°C	3	-150	1068	2,93	$6,42\cdot10^{-10}$	$2,79\cdot10^{-2}$

The parameters determined by the trapping model are shown in Table 15. N_r was calculated using equation 2.41, with $k_r=9,9\cdot10^{-17}$ *cm³ sites⁻¹ s⁻¹* [3].

Table 15: Values found by curve fitting of equation 2.43, the trapping model. C_0 calculated using equation 2.26 based on D_{eff} from trapping model. N_r calculated using equation 2.41.

| *Sample no.*	Trans. no.	D_{eff} [m² s⁻¹] [Charge – Iino]	λ	N_r [sites cm⁻³]	C_0 [ppm W]
1, 30˚C	1	$7,49\cdot10^{-10}$	14,00	$2,55\cdot10^{13}$	$9,15\cdot10^{-3}$
1, 30˚C	2	$6,90\cdot10^{-10}$	26,00	$4,37\cdot10^{13}$	$9,12\cdot10^{-3}$
1, 30˚C	3	$5,00\cdot10^{-10}$	10,00	$1,22\cdot10^{13}$	$1,32\cdot10^{-2}$
1, 50˚C	1	$6,53\cdot10^{-10}$	9,00	$1,43\cdot10^{13}$	$2,45\cdot10^{-2}$
1, 50˚C	2	$8,36\cdot10^{-10}$	12,00	$2,44\cdot10^{13}$	$2,05\cdot10^{-2}$
1, 50˚C	3	$1,30\cdot10^{-9}$	16,00	$5,05\cdot10^{13}$	$1,26\cdot10^{-2}$
1, 75˚C	1	$3,18\cdot10^{-9}$	28,00	$2,17\cdot10^{14}$	$1,23\cdot10^{-2}$
1, 75˚C	2	$3,39\cdot10^{-9}$	27,00	$2,23\cdot10^{14}$	$9,65\cdot10^{-3}$
1, 75˚C	3	Poor fit	-	-	-
2, 50˚C	1	$4,85\cdot10^{-10}$	5,00	$6,16\cdot10^{12}$	$1,94\cdot10^{-2}$
2, 50˚C	2	Poor fit	-	-	-
2, 50˚C	3	$3,62\cdot10^{-10}$	6,00	$5,52\cdot10^{12}$	$3,33\cdot10^{-2}$
3, 75˚C	1	Poor fit	-	-	-
3, 75˚C	2	$2,13\cdot10^{-9}$	12,00	$6,27\cdot10^{13}$	$8,64\cdot10^{-2}$
3, 75˚C	3	$3,45\cdot10^{-9}$	91,00	$7,70\cdot10^{14}$	$5,19\cdot10^{-3}$
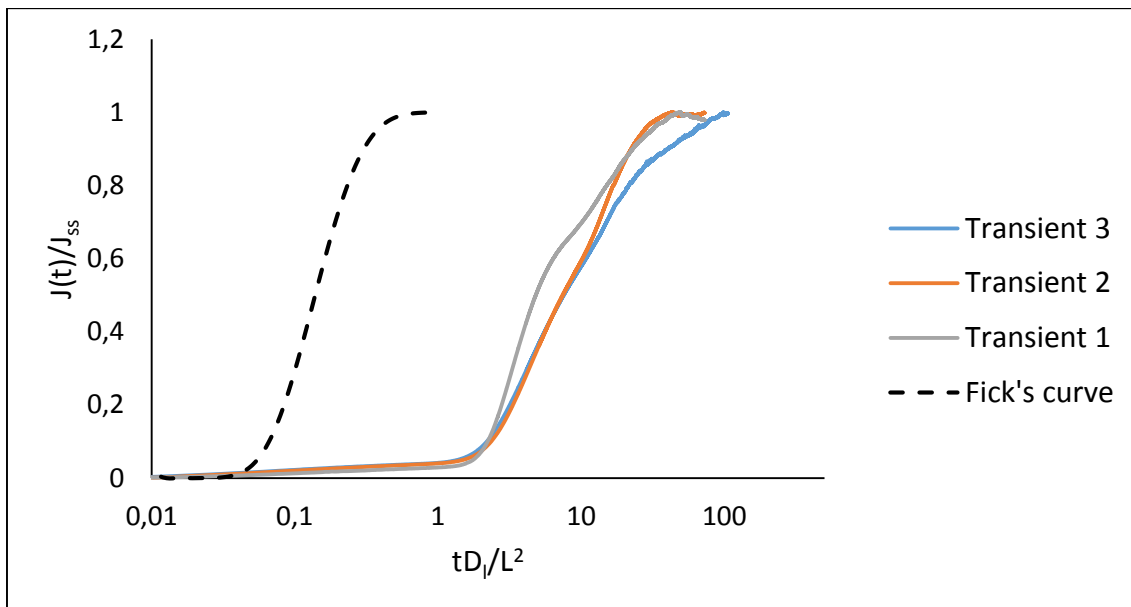
Figure 42: Normalized permeation flux for charging transients at 30°C, sample 1. Single anodic polarization between transients.
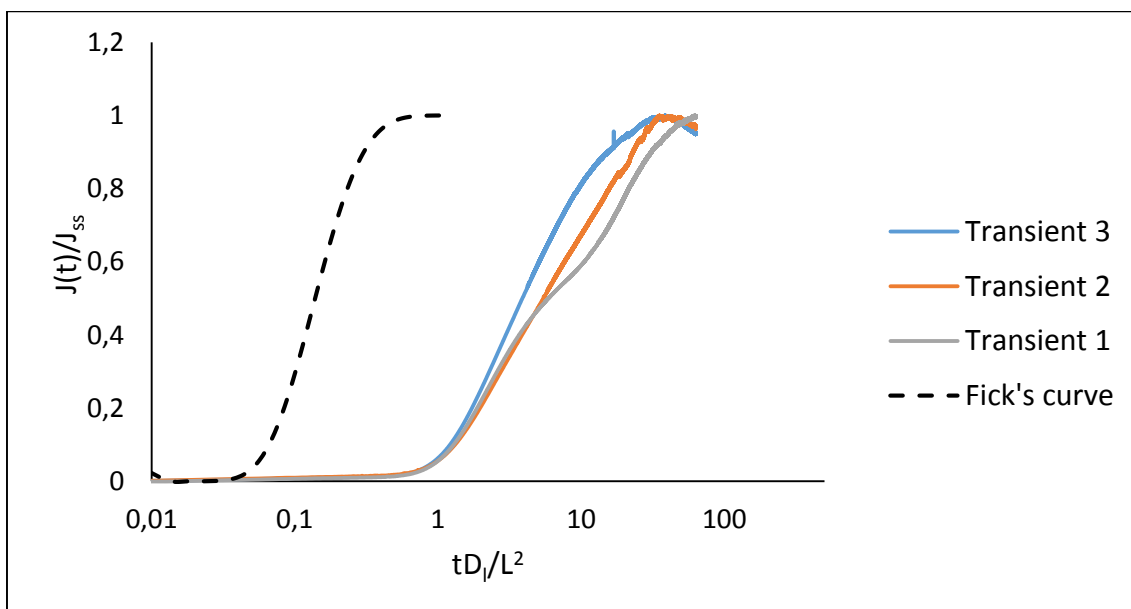

Figure 43: Normalized permeation flux for charging transients at 50°C, sample 1. Single anodic polarization between transients.
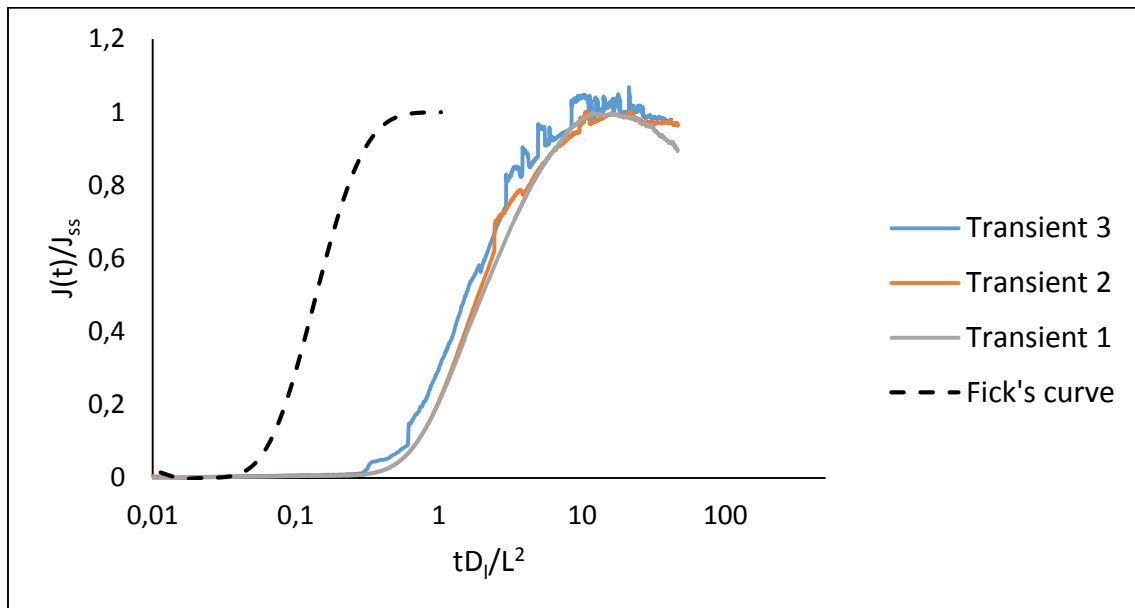
Figure 44: Normalized permeation flux for charging transients at 75˚C, sample 1. Single anodic polarization between transients.

The logging of the temperature during the test on 75˚C revealed that the maximum temperature fluctuations were ±0,2˚C, which is accepted for this kind of test. According to the ASTM standard [1], it is recommended to keep the temperature fluctuations below ±0,5˚C. The same fluctuations in the permeation transients that was seen during the first test on 75˚C for BM1 could not be observed for HAZ1. Given the fact that the same heating device was used throughout the entire experimental work in this thesis, the noise from it was an unlikely cause for the current fluctuations seen in the first test on BM1 at 75˚C. All indications pointed towards the fluctuations being a one-time event.

What was discovered here was that the electrolyte on the cathodic side turned yellow after sample 1 had been tested continuously at 30˚C, 50˚C and 75˚C. To investigate this further, the electrolyte was examined as explained in Section 4.4. The examination of the cathodic surface of the sample is described in Section 4.3.

The transients from the test of sample 2 and 3 at temperatures of 50˚C and 75˚C are shown in Figure 45 and Figure 46.
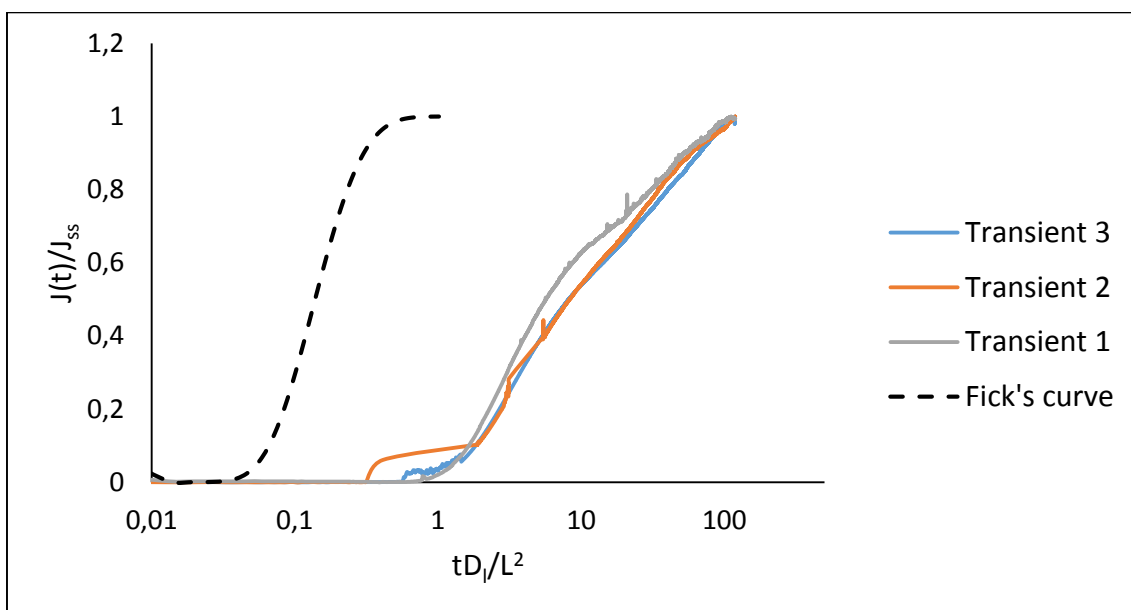
Figure 45: Normalized permeation flux for charging transients at 50˚C, sample 2. Single anodic polarization between transients.
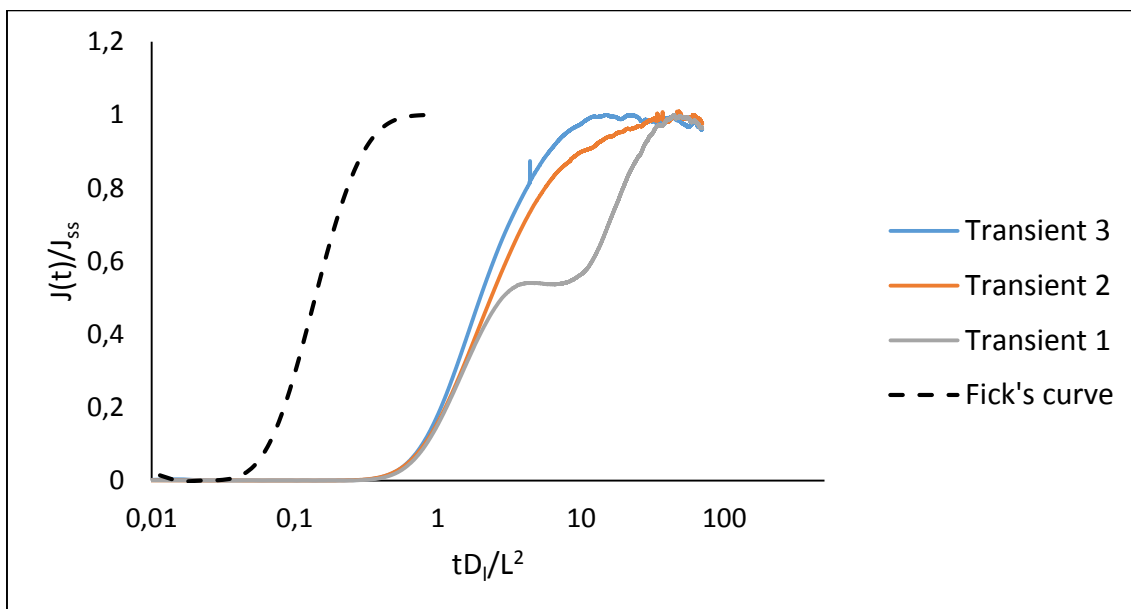

Figure 46: Normalized permeation flux for charging transients at 75˚C, sample 3. Single anodic polarization between transients.

The first transient obtained on each sample is shown in Figure 47. A similar behaviour could be detected for each first transient, namely the "double plateau" as mentioned in Section 2.7.1. This behaviour was also seen in the first transient for BM1 at 75°C. This behaviour has been reported earlier by both Iino and Fallahmohammadi [3, 4, 31]. The first assumption, made by Iino, states that the cause of this "double plateau" is reversible traps affecting the permeation rate. By varying the trapping parameters in the trapping model as described in Section 2.7.1, the "double plateau" behaviour occurs. This verifies that trapping caused this behaviour. However, as reported by Fallahmohammadi [3, 31], irreversible traps can also cause this behaviour depending on the binding energy of the trap. Given the fact that this "double plateau" occurred mostly during the first transient, the assumption regarding irreversible traps was plausible.

No sign of an increased break-through time could be detected between the first and second transient in each test.
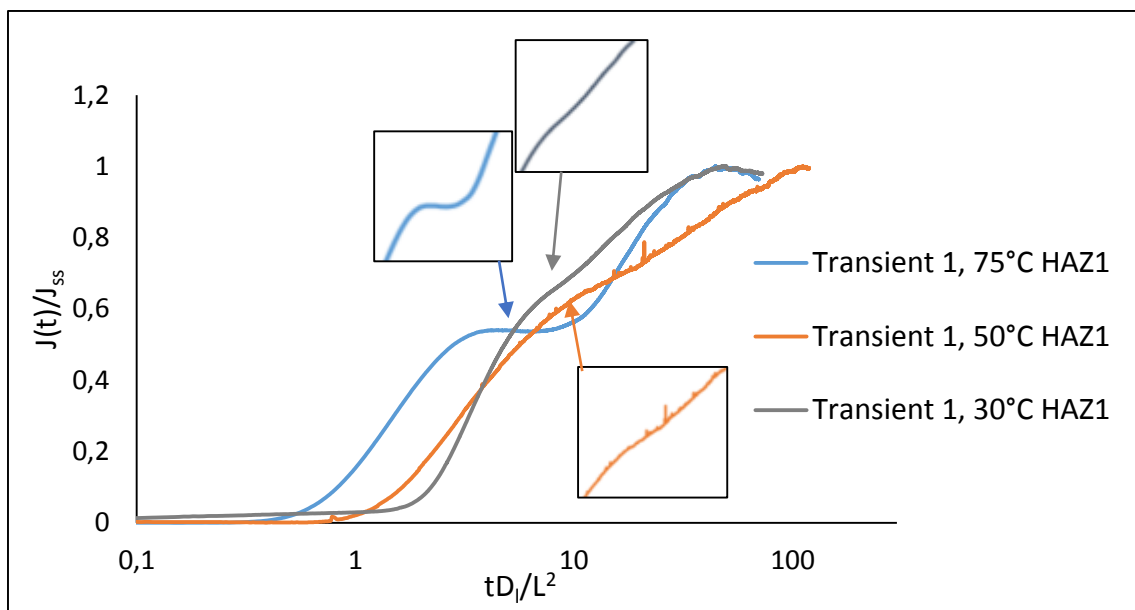
Figure 47: Transient 1 at 30°C, 50°C and 75°C showing a "double plateau".

When determining the Arrhenius line for HAZ1, the transients obtained on sample 1 were considered. This means that except for the first transient obtained at 30°C, no irreversible trapping effects was assumed to affect the transients. All the transients except for the first one were therefore used to determine the Arrhenius line. The upper line in Figure 48 represents the D_{eff} values determined by the trapping model, while the lower line represents the D_{eff} values determined by the t_{lag} method. The further calculations are based on the trapping model values.
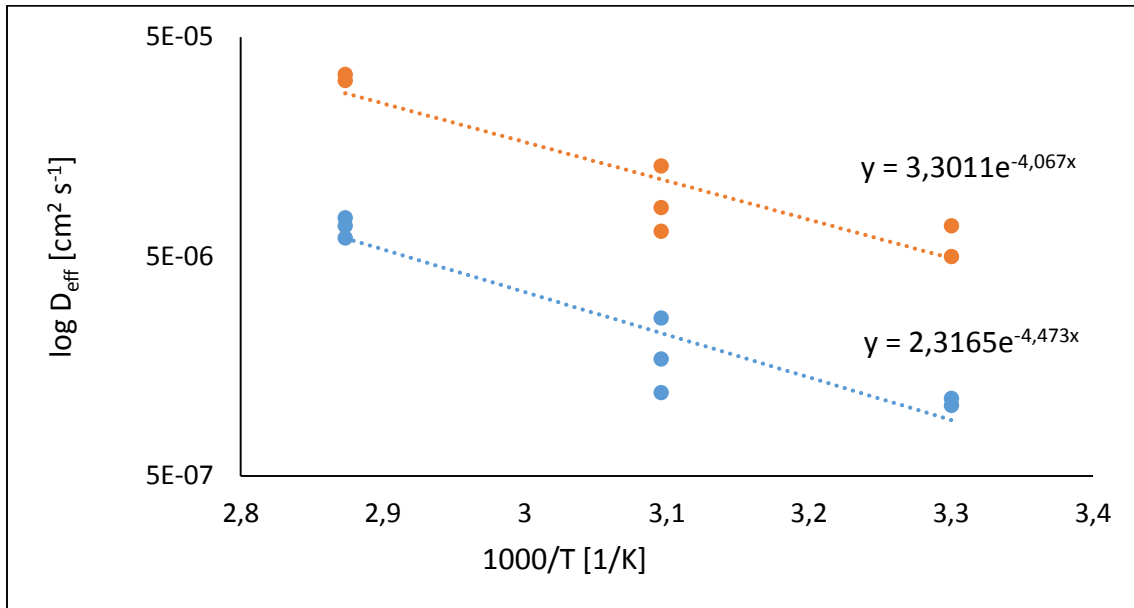
Figure 48: Scatter plot of D_{eff} vs. (1000/T). Regression used for estimating the Arrhenius line.

$$D = D_0 \exp(\frac{-E_l}{RT}) \tag{2.23}$$

This gives a lattice activation energy, E_l, of 33,81 $kJ\ mol^{-1}$. Equation (2.23) then changes to:

$$D = 3,3011 \exp(\frac{-33,81 kJmol^{-1}}{RT}) \tag{4.10}$$

By fitting this into equation 2.30, the density of reversible traps, N_r, can be found.

$$D_0 \frac{N_l}{N_r} = 3,3011 \tag{4.11}$$

$$N_r = \frac{7,23\ x\ 10^{-4}\ x\ 5,23\ x\ 10^{23}}{3,3011} = 1,15\ x\ 10^{20}\ sites\ cm^{-3}$$

The binding energy for the reversible traps becomes:

$$E_b = 33,81\ kJmol^{-1} - 5,69\ kJmol^{-1} = 28,12\ kJ\ mol^{-1} \tag{4.12}$$

N_r calculated by the Arrhenius equation 2.23 was higher than the N_r calculated by equation 2.41. The N_r calculated by equation 2.41 varied between $1,22 \cdot 10^{13} - 7,70 \cdot 10^{14}\ sites\ cm^{-3}$.

4.2.3   BM2 (1% strain)

The results from the t_{lag} method are shown in Table 16. The resulting charging transients plotted in a normalized flux vs. dimensionless time plot together with Fick's curve for lattice diffusion are shown in Figure 49.

Table 16: Results for X70 BM2. I_{ss} denotes the anodic steady state permeation current. D_{eff} from charge transient calculated using equation 2.22 and C_0 calculated using equation 2.26, based on D_{eff} from equation 2.22.

Sample no.	Trans. No.	i_c [μA cm^{-2}]	t_{lag} [s]	I_{ss} [μA]	D_{eff} [m^2 s^{-1}] [Charge - t_{lag}]	C_0 [ppm W]
1, 30˚C	1	-150	3057	0,67	$2,24 \cdot 10^{-10}$	$1,82 \cdot 10^{-2}$
1, 30˚C	2	-150	2061	0,51	$3,33 \cdot 10^{-10}$	$9,34 \cdot 10^{-3}$
1, 30˚C	3	-150	2085	0,46	$3,29 \cdot 10^{-10}$	$8,58 \cdot 10^{-3}$

The parameters determined by the trapping model are shown in Table 17. N_r was calculated using equation 2.41, with $k_r = 9,9 \cdot 10^{-17}$ *cm^3 sites^{-1} s^{-1}* [3].

Table 17: Values found by curve fitting of equation 2.43, the trapping model. C_0 calculated using equation 2.26 based on D_{eff} from trapping model. N_r calculated using equation 2.41.

Sample no.	Trans. no.	D_{eff} [m^2 s^{-1}] [Charge – Iino]	λ	N_r [sites cm^{-3}]	C_0 [ppm W]
1, 30˚C	1	$8,21 \cdot 10^{-10}$	8,00	$1,61 \cdot 10^{13}$	$4,97 \cdot 10^{-3}$
1, 30˚C	2	$1,59 \cdot 10^{-9}$	23,00	$8,98 \cdot 10^{13}$	$1,95 \cdot 10^{-3}$
1, 30˚C	3	$1,49 \cdot 10^{-9}$	19,00	$6,96 \cdot 10^{13}$	$1,89 \cdot 10^{-3}$
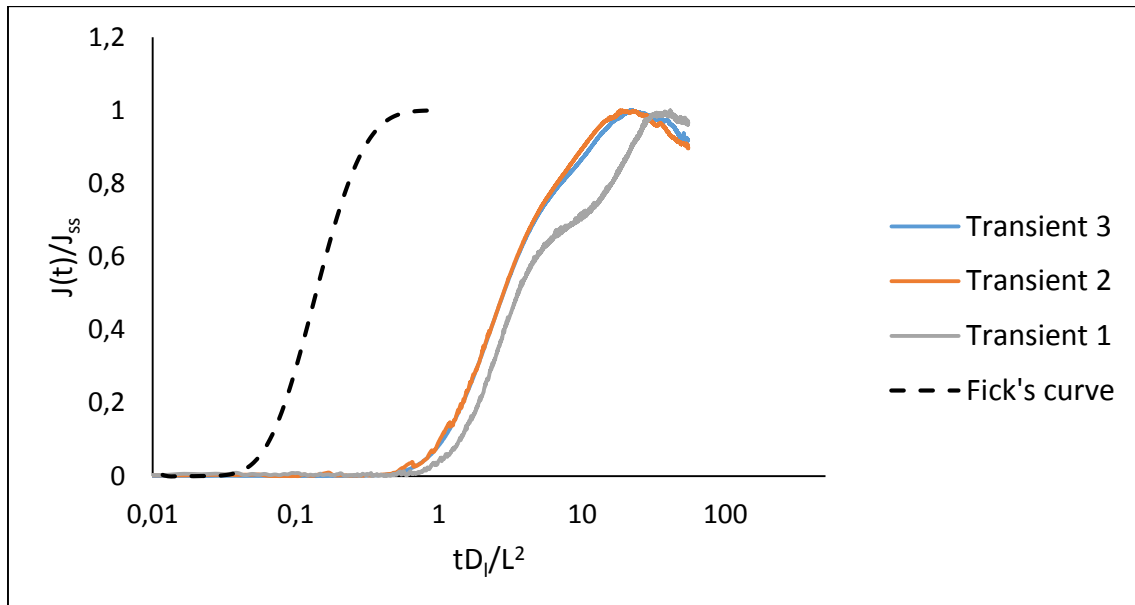
Figure 49: Normalized permeation flux for charging transients at 30°C. Single anodic polarization between transients.

The characteristic "double plateau" behaviour, as described in Section 2.7.1 and 4.2.2, was also seen for the first transient obtained at 30°C. The main difference was that in this case, an increased break through time for the first transient could also be seen simultaneously with the "double plateau" behaviour. This was not the case for the BM1 and HAZ1 samples where this behaviour occurred.

In Figure 50, the D_{eff} vs. pre-strain level is shown. The upper line represents the D_{eff} values determined by the trapping model, while the lower line represents the D_{eff} values determined by the t_{lag} method.

Figure 50: D_{eff} as a function of pre-strain level for X70 BM at 30°C. The plotted values for D_{eff} are from the third transients.

4.3   Material examination

In order to examine the surface of the samples, the Scanning Electron Microscope (SEM) was utilized. The goal of this was to characterize the microstructure and get good surface pictures of the different samples, and also to investigate the cathodic and anodic surface composition of the samples. This composition investigation was executed for the samples where the electrolyt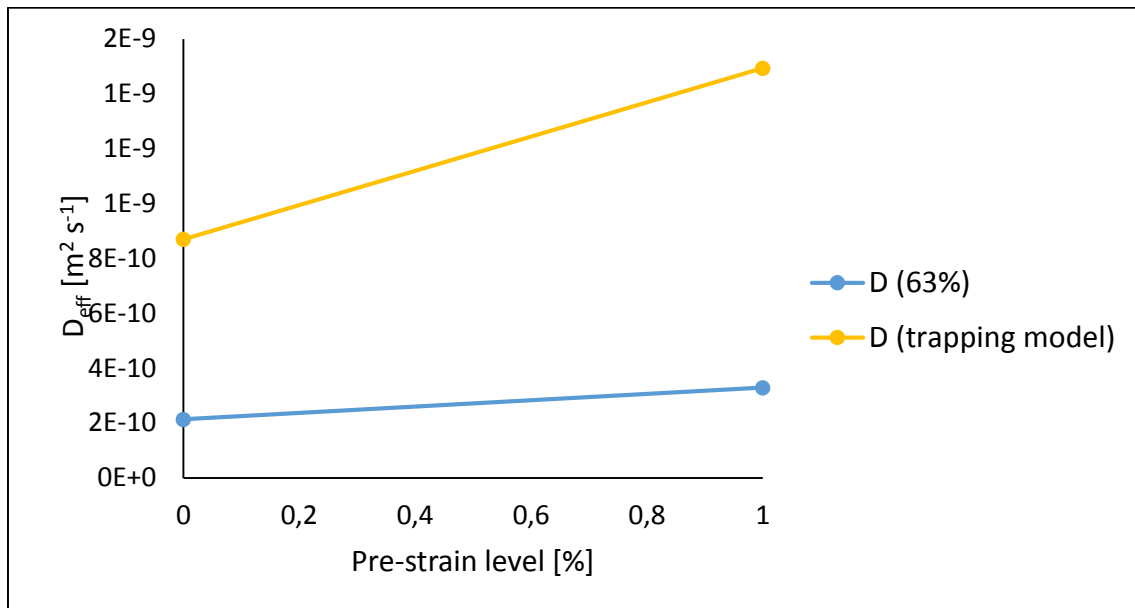e got polluted and turned into a yellow color using Energy Dispersing Spectroscopy (EDS). This happened for Fe3wt.% Si sample 1 that was tested continuously at 30°C, 50°C and 75°C according to both Method 1 and Method 2, and also X70 HAZ1 sample 1 that was tested continuously at 30°C, 50°C and 75°C according to Method 1. The Fe3wt.%Si sample 1 was tested for 2-3 weeks, while X70 HAZ1 sample 1 was tested for 1-2 weeks. In other words, both samples were installed for a relatively long time.

4.3.1   Surface examination

Figure 51 and Figure 52 show the surface examination of the cathodic and anodic side of Fe3wt.%Si sample 1, respectively. A huge difference could be noticed between the two sides. Despite approximately same surface conditions of the two sides prior to testing, only the cathodic side revealed its microstructure after testing. On the anodic side, grinding lines etc. from the preparation could still be noticed. On the cathodic side, no such traces from preparation

could be seen. This indicated that the cathodic side got etched during the testing, enabling the revealing of the microstructure. Figure 52 shows the grain boundaries on the cathodic side of the Fe3wt.%Si sample, revealing its grain structure. The microstructure of this sample was pure ferritic, i.e. single phase BCC.
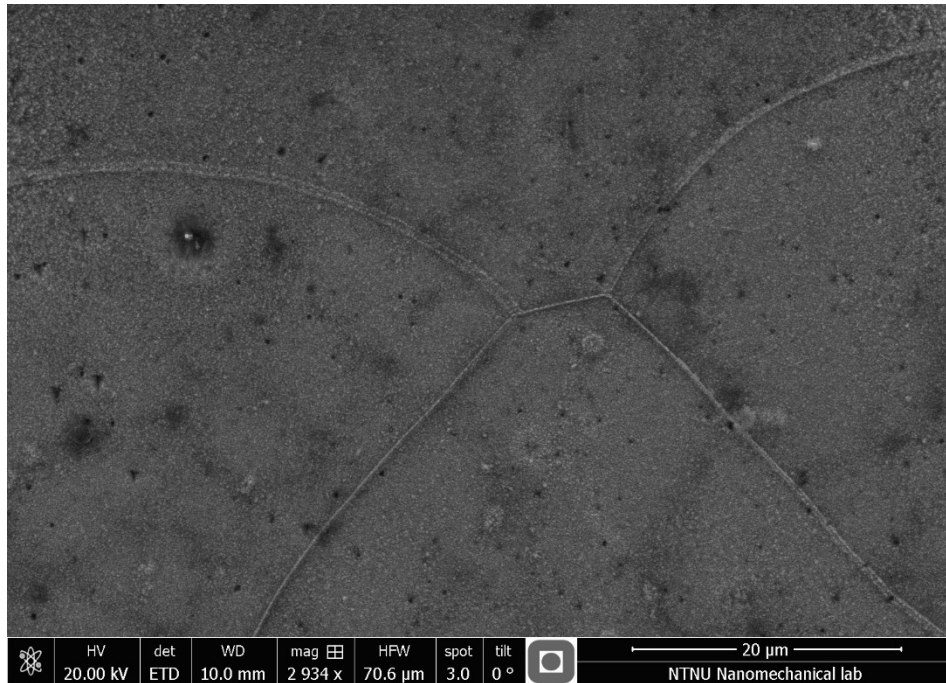

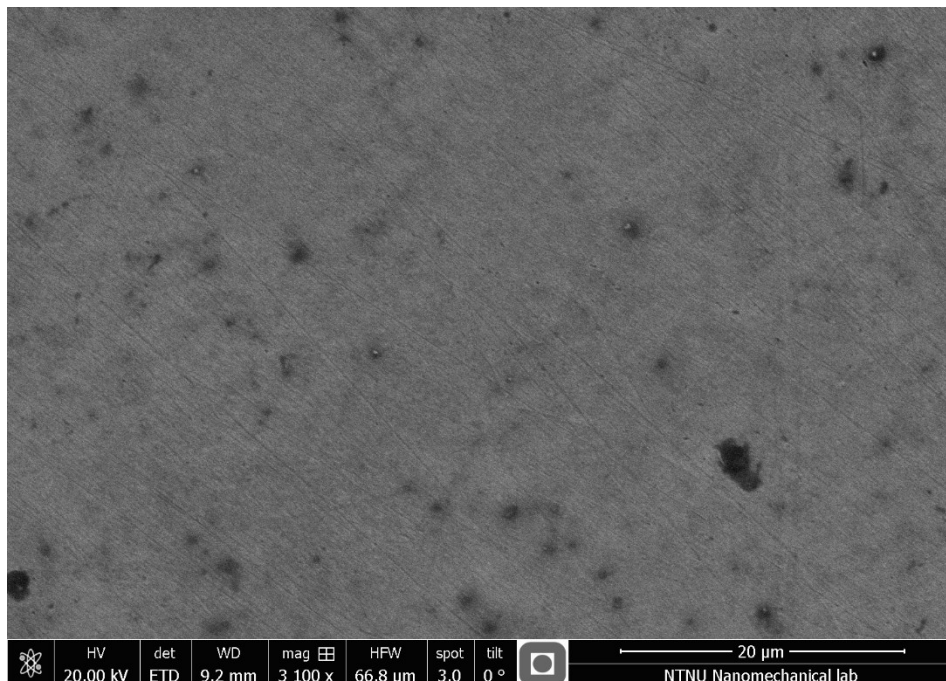Figure 51: Cathodic side of Fe 3wt.%Si sample 1 at 2900x magnification.

Figure 52: Anodic side of Fe 3wt.%Si sample 1 at 3100x magnification.

70

Huge differences between the anodic and cathodic sample surface could also be noticed for X70 HAZ1 sample 1. Only the cathodic side revealed its microstructure, while the anodic side showed traces of preparation. The surface conditions for the two sides prior to testing were approximately similar. For this sample, pitting was discovered on the anodic side as seen in Figure 54, which proved that localized corrosion had taken place. The pitting was not as prominent for the Fe3wt.%Si sample. Figure 53 shows the cathodic side of the sample, while Figure 54 shows the anodic side. The microstructure was characterized to be dual phase, consisting of Bainite and Ferrite. However, considering the fact that the surface was examined after testing without further surface treatment, the microstructure was not as easily characterized because of contamination and incomplete etching. Previous examinations of the microstructure of both X70 BM1 and HAZ1 executed by Hauge [28] and Olden et al [43] have led to the conclusion that BM1 contains a Ferritic/Pearlitic structure, while HAZ1 contains mainly Martensite with Acicular Ferrite and Ferritic sideplates. As stated in the unpublished paper by Olden et al [43], the resulting microstructure for heat treated X70 HAZ samples is generally a mixture between Martensite and Bainite . This might explain and justify why the microstructure of HAZ1 in the present work was concluded to be Bainite and Ferrite. The cathodic side of X70 BM1 tested at 75°C was also examined, but as this was tested for a lot shorter amount of time the etching on the cathodic side was not that prominent and the microstructure could not be identified. It was assumed to be similar to the results by Hauge and Olden et al [28, 43], considering the samples were from the very same slab of material as in the present work.
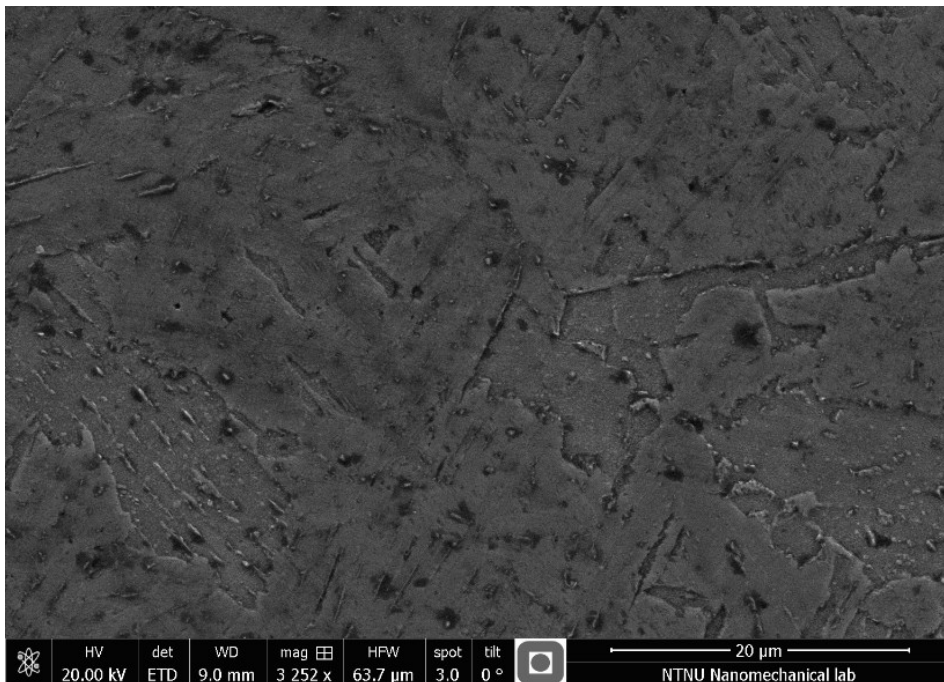

Figure 53: Cathodic side of X70 HAZ1 sample 1 at 3200x magnification.
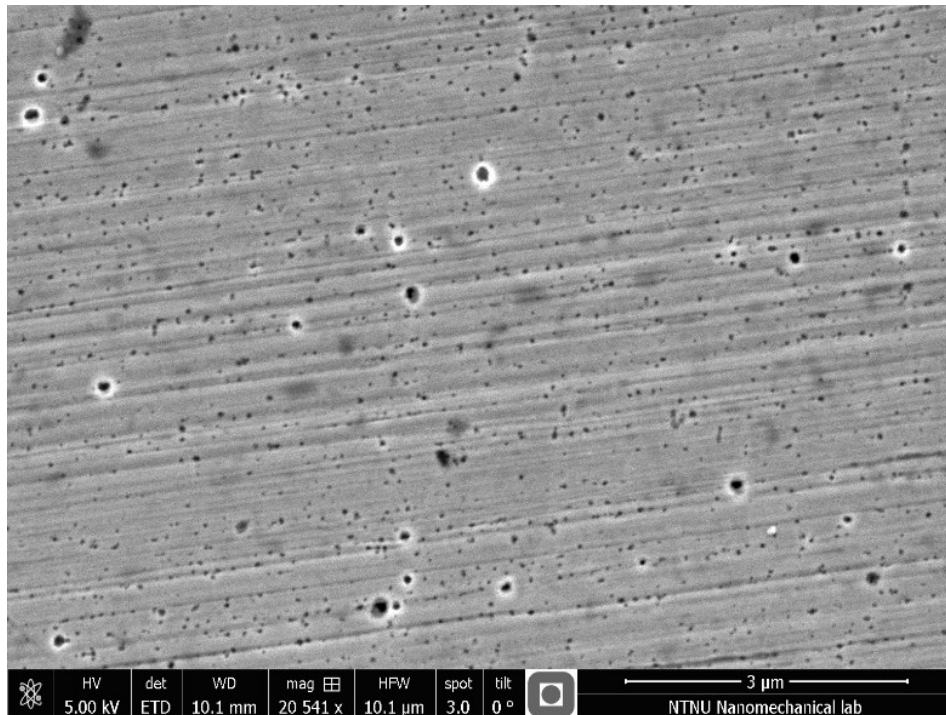
Figure 54: Anodic side of X70 HAZ1 sample 1 at 20500x magnification.

4.3.2   Composition of materials

To examine the cathodic and anodic surface of the different samples and decide the chemical composition, EDS was utilized. One EDS test was done on the surface of the material, and a second EDS test was done in the bulk of the material with an accelerating voltage of 5 kV and 20 kV, respectively. The original composition from the bulk of the material could then be compared to the composition at the surface of the material.

For both X70 HAZ1 and Fe 3wt.% Si, differences between the surface and the bulk composition could be identified. Both the oxygen and carbon content on both the anodic and cathodic surface was higher than in the bulk for both samples. The increased oxygen level indicated that an oxide layer most likely had formed on the surface before or during the testing, while the increased carbon level could origin from the glycerin in the electrolyte or simply be organic contamination originating from before the testing. To examine if the increased oxygen and carbon content on the surface originated from before or after submersing the samples in the electrolyte, an EDS test was also executed on the surface of a freshly polished Fe3wt.%Si sample. This showed slightly elevated amounts of both carbon and oxygen, meaning that parts of the oxygen and carbon amounts detected on the surface of the tested samples most likely formed before the submersing. The surface oxygen levels for Fe3wt.%Si before and after testing were approximately 3wt.% and 6wt.% for the anodic side and 3wt.% and 10wt.% for the cathodic

side, while the carbon levels were approximately 19wt.% and 10wt.% for the anodic side and 19wt.% and 29wt.% for the cathodic side. The oxygen levels increased slightly on both the anodic and cathodic side. The carbon level decreased on the anodic side, while it increased on the cathodic side.

However, black spots noticed on the surface of the samples turned out to be carbon contamination. A point analysis showed severely elevated carbon levels at these contamination spots. These spots were not detected before testing, meaning that the glycerin in the electrolyte had contaminated the surface during testing. White spots noticed on the surface turned out to be traces of an oxide layer, and the point analysis showed severely elevated oxygen levels at these spots. These spots could not be seen before testing, revealing a formation of an oxide layer during testing. Figure 55, Figure 56, Figure 57 and Figure 58 show the analysis on the cathodic surface of the both Fe3wt.%Si and X70 HAZ1, i.e. not the contaminated spots.

Figure 55: EDS from the surface of Fe 3wt.% Si sample after testing. The y-axis represents the number of counts per second, i.e. the signal for each element, while the x-axis represents the energy level for the counts.
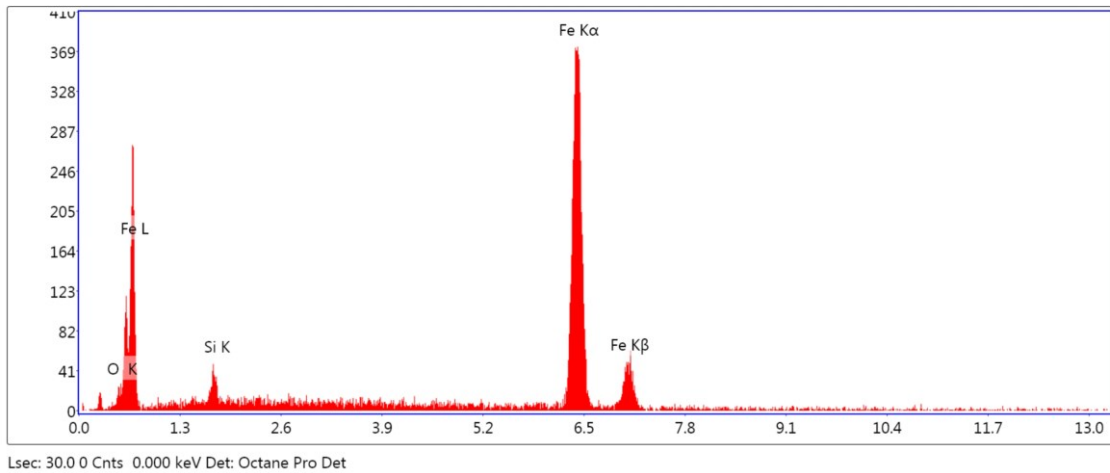
Figure 56: EDS from the bulk of Fe 3wt.% Si sample after testing. The y-axis represents the number of counts per second, i.e. the signal for each element, while the x-axis represents the energy level for the counts.
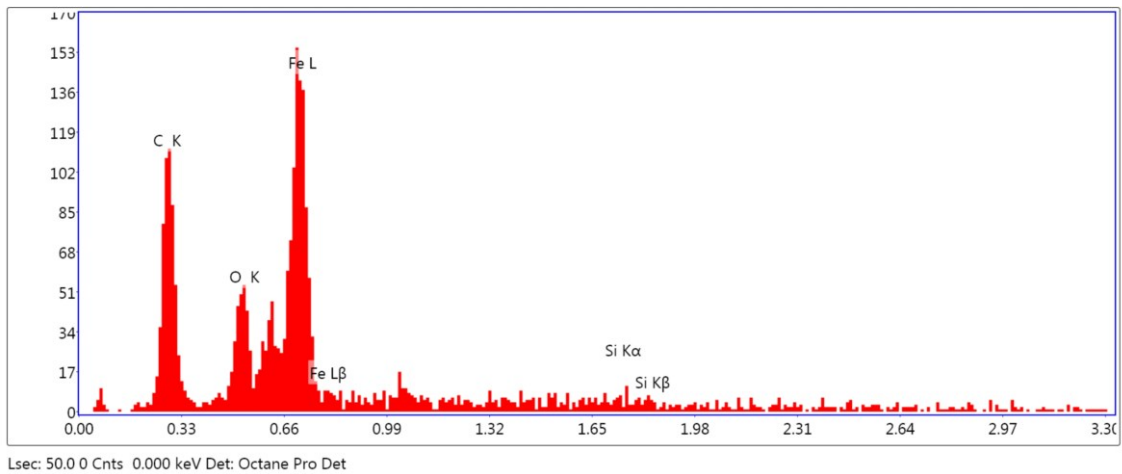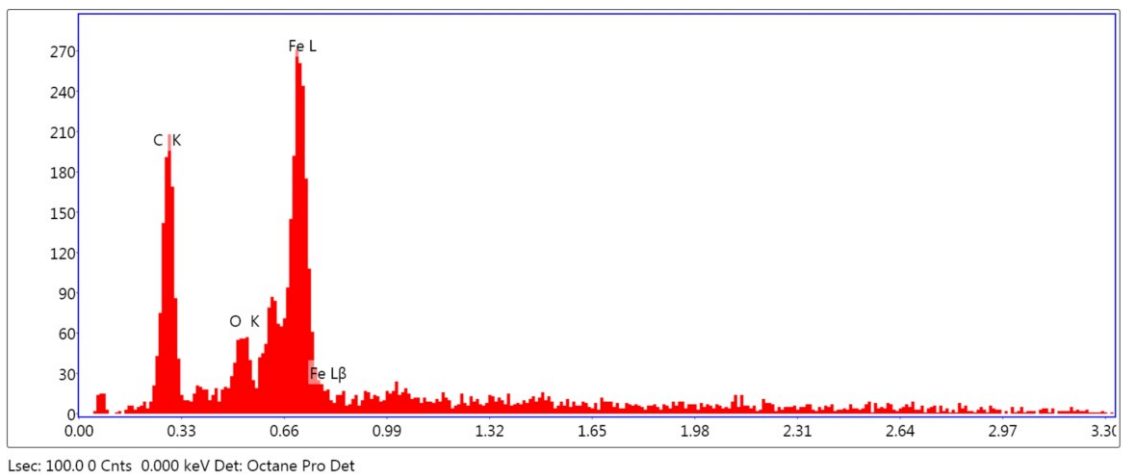

Figure 57: EDS from the surface of X70 HAZ1 sample after testing. The y-axis represents the number of counts per second, i.e. the signal for each element, while the x-axis represents the energy level for the counts.

74
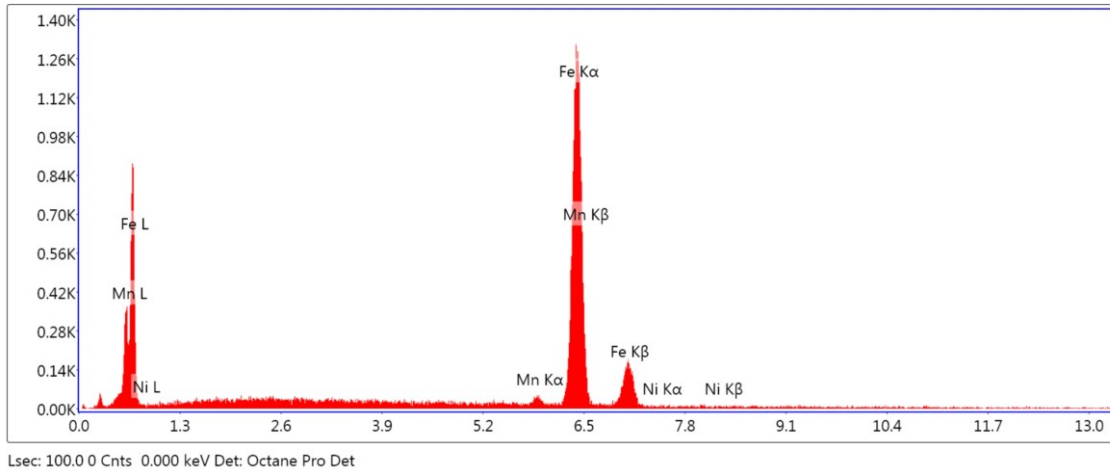
Figure 58: EDS from the bulk of X70 HAZ1 sample after testing. The y-axis represents the number of counts per second, i.e. the signal for each element, while the x-axis represents the energy level for the counts.

4.4   Examination of polluted electrolyte

To investigate the changes in the electrolyte on the cathodic side from the tests on Fe3wt.%Si sample 1 and X70 HAZ1 sample 1, pH and conductivity were measured and compared to the values obtained before testing. In addition, by using Potassium FerriCyanide/FerroCyanide, it was decided if the electrolyte contained Fe^{2+} or Fe^{3+} ions. The results are shown in Table 18.

The process of detecting Fe^{2+}/Fe^{3+} ions consisted of making 0,1M solutions of Potassium Ferricyanide, $K_3[Fe(CN)_6]$, and Potassium Ferrocyanide, $K_4[Fe(CN)_6]\cdot3H_2O$, and adding a small amount of the solutions to the polluted electrolyte.

If a blue precipitate forms when $K_3[Fe(CN)_6]$ is added to a solution, Fe^{2+} is present in the solution. If the blue precipitate forms when $K_4[Fe(CN)_6]\cdot 3H_2O$ is added, Fe^{3+} is present in the solution [44].

Potassium Ferrocyanide solution + Fe^{3+} [44]:

$$4Fe^{3+} + 3[Fe(CN)_6]^{4-} \rightarrow Fe_4[Fe(CN)_6]_3 \qquad \textit{Dark blue precipitate} \qquad (4.13)$$
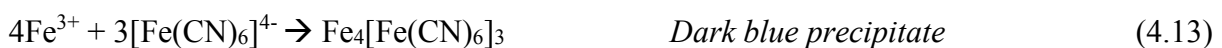
Potassium Ferricyanide solution + Fe^{2+} [44]:

$$Fe^{2+} + [Fe(CN)_6]^{3-} \rightarrow Fe^{3+} + [Fe(CN)_6]^{4-} \qquad (4.14)$$

$$4Fe^{3+} + 3[Fe(CN)_6]^{4-} \rightarrow Fe_4[Fe(CN)_6]_3 \qquad \textit{Dark blue precipitate} \qquad (4.13)$$

Table 18: Results of the examination of the polluted electrolyte. pH and Resistivity were measured before and after testing, and a detection test for iron ions was executed after the testing.

Sample material Tests executed	pH	Resistivity	Fe^{2+}	Fe^{3+}
Fe3wt.%Si sample 1 30˚C, 50˚C and 75˚C Method 1 and 2	Before: 7,13 After: 7,06	Before: 380 Ωcm After: 490 Ωcm	No	No
X70 HAZ1 sample 1 30˚C, 50˚C and 75˚C Method 1	Before: 7,13 After: 7,03	Before: 380 Ωcm After: 484 Ωcm	No	No

The change in pH was insignificant in this matter, as such a small change was difficult to relate to anything. The measured resistivity was higher after the testing than before.

When trying to detect Fe^{2+}/Fe^{3+} ions, none of the characteristic reactions mentioned above happened. In other words, the dark blue precipitate did not form when adding either of the 0,1M solutions to the electrolyte, indicating that none of the ions were present. The yellow colour of the electrolyte could therefore not with certainty be related to iron ions present in the electrolyte.

Chapter 5

Comparison with previous results

The results obtained for the Fe3wt.%Si samples described in Section 4.1.1 and 4.1.2 found by the trapping model were compared with results reported by Kumnick and Johnson [45]. The results found were for pure iron. This will not provide a perfect foundation for comparison, but it is assumed to give a decent indication.

The results reported by Hauge [28], and also the results reported by Olden et al [43] were the main basis for comparison of the X70 steel as the tests done in these works were executed on the very same slab of X70 steel as in this thesis. The diffusion properties for the steel obtained in this thesis were therefore assumed to show similarity to the previous results. For a wider comparison, the results obtained by Smirnova [15] for X70 BM1 were also included, even though they were not obtained on the very same slab of X70 steel. The present results reported in this comparison were obtained by charging the standard way as mentioned in Section 3.4.1 because this was the chosen method in the work done by Hauge, Olden et al and Smirnova [15, 28, 43], i.e. no partial charging/discharging. Hauge [28] only tested the samples to be compared at one temperature, 25°C. Most of the comparison is therefore done with respect to the results obtained by Olden et al [43], as the samples in this work were tested at elevated temperatures as well. A comparison of the permeation transients can be found in Appendix B. For all of the testing done on X70 steel, the steady state permeation currents found in this thesis were significantly lower than in the results reported by Olden et al [43]. Most of the transients shown in a normalized flux vs. dimensionless time plot were also less steep than both Fick's curve and the previous results, and the break through time was lower. All this can also be seen in Appendix B.

In the comparison of the X70 steel, the results obtained by both the trapping model and the t_{lag} method are shown. This is because the results reported in the mentioned previous works were obtained by the t_{lag} method, and it is relevant to compare with results obtained in the same way. The values for N_r shown in this comparison were calculated by using the Arrhenius equation 2.23, as this was the chosen method in the previous works reported in this section.

5.1 Fe 3wt.% Si

Kumnick and Johnson [45] have reported values for hydrogen diffusivity in pure iron obtained by several authors. The values for D_{eff} reported in Figure 59 from this work are from the test with both single and double anodic polarization between the transients at 30°C, Method 1 and 2 respectively. Only the D_{eff} from the third transient is shown. The values reported for comparison represents hydrogen diffusivity at 25°C.
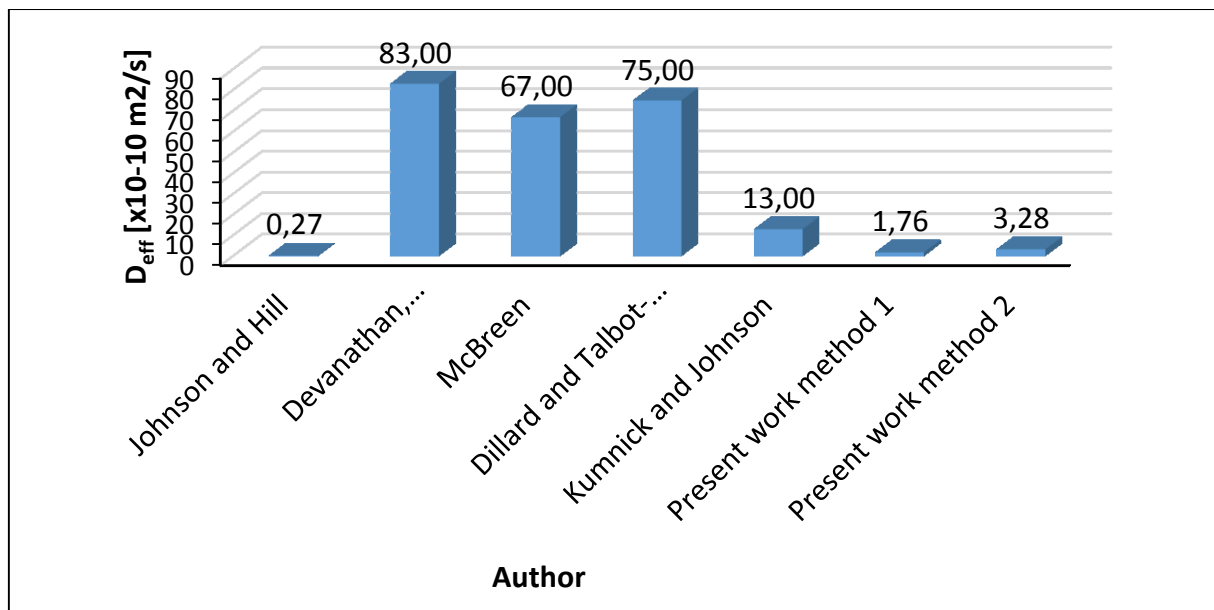
Figure 59: D_{eff} reported by various authors placed in chronological order, including the present work.

The materials used in this comparison are as follows [45]:

Johnson and Hill, 1960: 99,9 purity iron

Devanathan, Stachurski and Beck, 1963: Armco iron

McBreen, 1965: Armco iron

Dillard and Talbot-Besnard, 1973: 99,9965 purity iron

Kumnick and Johnson, 1974: 99,98 purity iron

Generally, the present results for Fe3wt.%Si showed lower D_{eff} values than the previous results for pure iron. The values reported by Johnson and Hill, however, are lower than the present results.

Considering this is not the very same material, this is not an optimal comparison. As reported by Kumnick and Johnson [45], the Armco iron consists of a total maximum wt.% of alloying elements of approximately 0,3wt.%. The Fe3wt.%Si contains a higher wt.% of alloying elements, approximately 3wt.%. This can be seen in Table 3.

5.2 X70 high strength steel

5.2.1 BM1 (0% strain)

In Figure 60, the D_{eff} from the third transient at each temperature is shown. The comparison of the sub-surface concentration range C_0, reversible trap binding energy E_b and number of reversible trapping sites N_r are shown in Table 19. The results from Olden et al [43] and the results from Hauge [28] are shown in the same row because the results reported by Olden et al were an extension of the results reported by Hauge. The results marked "[1]" are calculated based on the t_{lag} method, while the results marked "[2]" are calculated based on the trapping model.

Table 19: Comparison of C_0, E_b and N_r values for BM1 reported by several authors, including the present work.

Author	Temp.range [ºC]	C_0 range [ppm W]	N_r [sites cm^{-3}]	E_b [kJ mol^{-1}]
Hope (present work)	30-75	[1] $(1,37\text{-}4,18)\cdot 10^{-2}$ [2] $(0,19\text{-}2,03)\cdot 10^{-2}$	[1] $1,27\cdot 10^{21}$ [2] $1,29\cdot 10^{20}$	[1] 24,00 [2] 26,56
Hauge [28], Olden et al [43]	25-70	[1] $(3,30\text{-}5,81)\cdot 10^{-2}$	[1] $2,93\cdot 10^{18}$	[1] 38,15
Smirnova [15]	25-70	[1] $(2,00\text{-}3,00)\cdot 10^{-1}$	[1] $2,73\cdot 10^{19}$	[1] 35,60
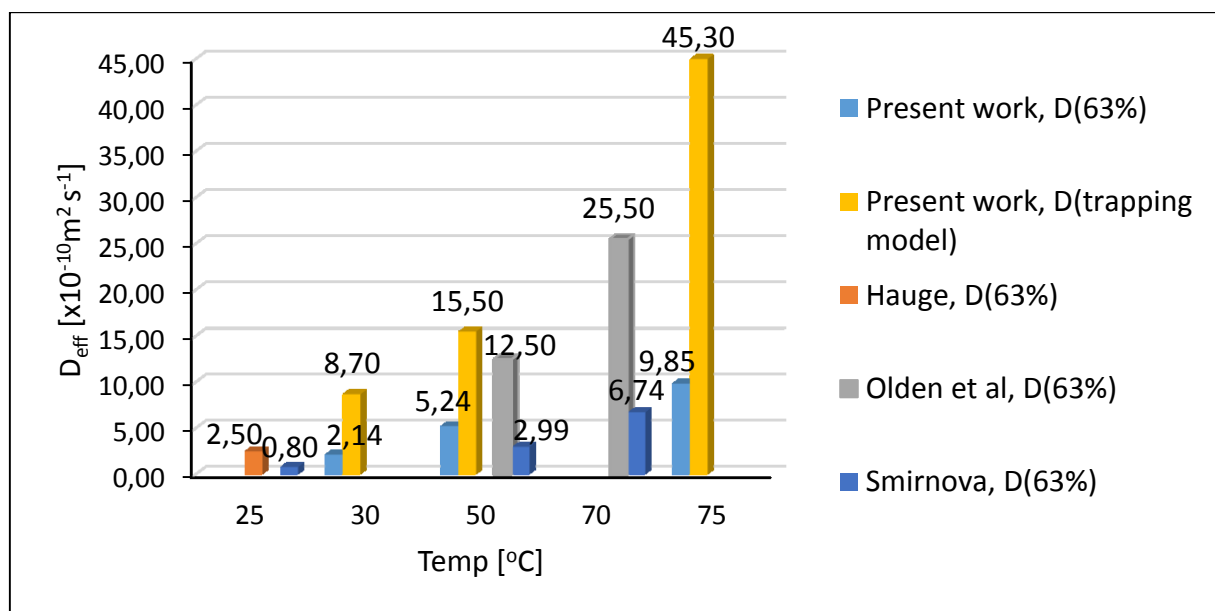
Figure 60: Comparison of D_{eff} values vs. temperature for BM1 reported by several authors, including the present work.

Compared to the previous results from the very same slab of steel, the D_{eff} found in the present work by the t_{lag} method was lower. The D_{eff} found by the trapping model, however, was higher. The D_{eff} obtained by Smirnova was lower than all of the reported values from the same slab of steel as used in the present work. This might have its out spring in a slightly different microstructure, alloying weighting etc. in the different batches of X70 steel. The sub-surface concentration C_0 was lower in the present work compared to all of the previous values. The binding energy E_b was lower, while N_r turned out to be higher.

5.2.2   HAZ1 (0% strain)

In Figure 61, the D_{eff} from the third transient at each temperature is shown. The D_{eff} values for HAZ at the different temperatures included in this comparison were obtained on the very same sample, both in the work reported by Olden et al [43] and in the present work. The comparison of the sub-surface concentration range C_0, reversible trap binding energy E_b and number of reversible trapping sites N_r are shown in Table 20.

Table 20: Comparison of C_0, E_b and N_r values for HAZ1 reported by several authors, including the present work.

| Author	Temp.range [ºC]	C_0 [ppm W]	N_r [sites cm^{-3}]	E_b [kJ mol^{-1}]
Hope (present work)	30-75	[1] $(3,82-13,28)\cdot10^{-2}$ [2] $(0,91-2,45)\cdot10^{-2}$	[1] $1,63\cdot10^{20}$ [2] $1,15\cdot10^{20}$	[1] 31,50 [2] 28,12
Hauge [28], Olden et al [43]	25-70	[1] $(6,01-16,39)\cdot10^{-2}$	[1] $4,98\cdot10^{18}$	[1] 39,82
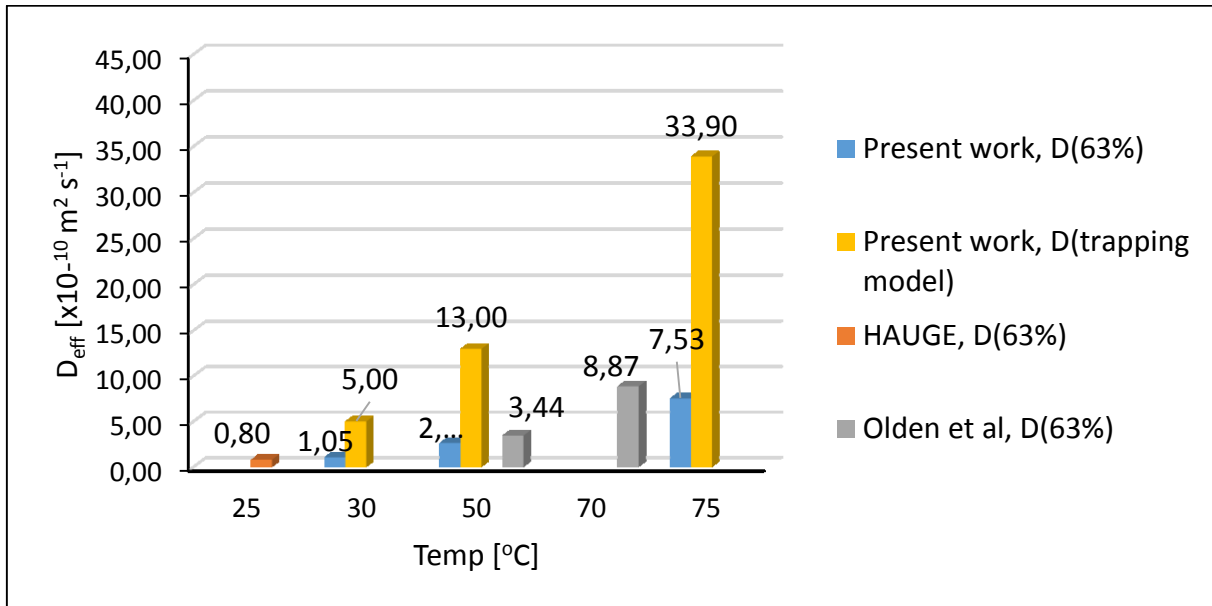
Figure 61: Comparison of D_{eff} values vs. temperature for HAZ1 reported by several authors, including the present work.

The same trend as for BM1 could be seen here. The D_{eff} values from the t_{lag} method of the present results were lower, and the D_{eff} values from the trapping model were higher than the previous values. The sub-surface concentration C_0 was lower in the present work compared to the previous values. The binding energy E_b was lower, while N_r turned out to be higher.

5.2.3   BM2 (1% strain)

For BM2, where the testing was executed at one temperature, the Arrhenius relation could not be obtained. The D_{eff} from each transient at this temperature is shown in Figure 62. In Figure 63 the Deff vs. pre-strain level is shown for X70 BM1 (0%strain) and BM2 (1%strain). The comparison of the sub-surface concentration range C_0 is shown in Table 21.

Table 21: Comparison of C_0 values for BM2 reported by several authors, including the present work.

Author	Temp.range [ºC]	C_0 range [ppm W]
Hope (present work)	30	[1] $(0,86\text{-}1,82)\cdot 10^{-2}$ [2] $(1,89\text{-}4,97)\cdot 10^{-3}$
Hauge [28]	25	[1] $(6,40\text{-}6,80)\cdot 10^{-2}$
Olden et al [43]	25	[1] $(59,27\text{-}159,78)\cdot 10^{-2}$
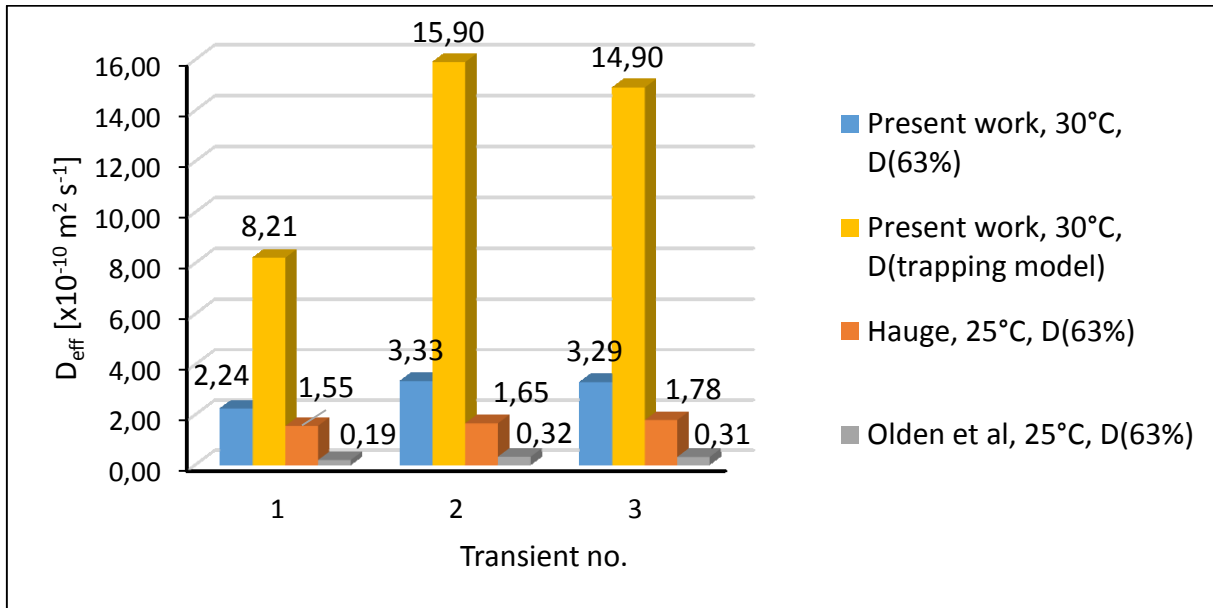
Figure 62: Comparison of Deff values vs. transient no. for BM2 reported by several authors, including the present work.
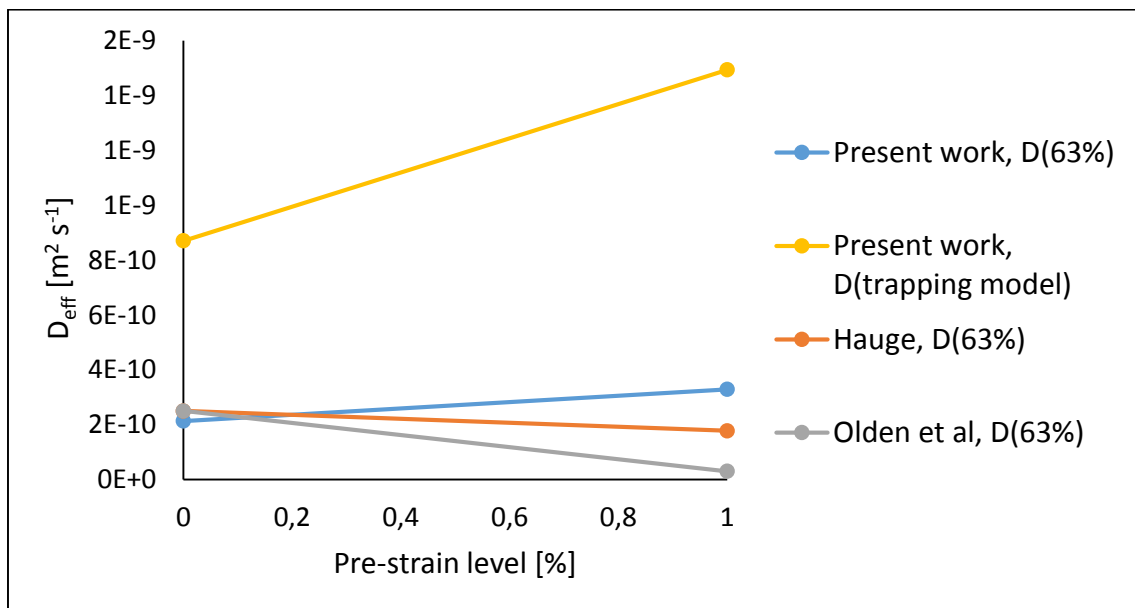
Figure 63: Comparison of D_{eff} values vs. pre-strain level for BM1 and BM2 reported by several authors, including the present work.

For this material, the D_{eff} calculated by both the t_{lag} method and the trapping model were higher than for all of the reported previous results, while the sub-surface concentration C_0 was lower. The increase in D_{eff} with increasing pre-strain level was only seen in the present work.

Chapter 6

Discussion

6.1   Testing and analyzing methods

When comparing the diffusion coefficients, D_{eff}, found in the three different ways for the samples, namely by the t_{lag} method, trapping model and discharge model, differences can be noticed. First of all, the D_{eff} from the discharge model was larger than for the t_{lag} method for all the tests reported in Section 4.1.2. The D_{eff} found from curve fitting of the trapping model was closer to the D_{eff} from the discharge model than from the t_{lag} method. This could actually indicate that the method of fitting the first part of the discharge curve to the discharge model produced results more representative of lattice diffusion than the t_{lag} method. However, the process of fitting the first part of the experimental discharge curve to the model gave quite inaccurate results as the fitting was done manually and a good fit was hard to achieve. What it provided was only a good indication.

For the partial charging transients, the assumption of a better fit to the Fourier solution of Fick's second law, Fick's curve, was verified. The transients obtained in that way was therefore more representative of lattice diffusion. The D_{eff} values found by the t_{lag} method for these transients were slightly higher than the values found by the t_{lag} method for the standard charge transients. The trapping model and t_{lag} method actually gave more similar results for the partial charging transients than for the standard charging transients, which is a good indication that trapping effects can be overcome to a greater extent when running partial charging transients.

For the tests described in Section 4.1.2, the difference in discharge currents measured on the anodic and cathodic side was prominent considering that the discharge curve from the cathodic side decreased much faster than on the anodic side. In addition, the cathodic current was much larger than the anodic current when initiating the discharge. On the anodic side, the sub-surface concentration C_0 was assumed to be zero before discharge because of the continuous oxidation of the hydrogen. On the cathodic side, on the other hand, the sub-surface concentration C_0 was not zero before discharge. When starting to polarize anodically on the cathodic side, and the concentration of hydrogen on the surface is not zero, a larger number of atoms will be oxidized immediately in order for the concentration to drop to zero. This might explain the immediate steepness of the discharge curve on the cathodic side compared to the anodic side, in addition to the current initially being higher. On the anodic side, the atoms need to diffuse their way out of the sample before they are oxidized, which makes the process slower.

The N_r values calculated by the trapping model, equation 2.41, were much lower than the N_r values calculated by the Arrhenius relation, even though the Arrhenius line was determined based on the D_{eff} values from the trapping model. However, because the trapping model includes many unknown parameters, small variations in the parameter values can lead to different but equally good fits to the experimental data. Thus, calculations based on the model parameters might lead to inaccurate results. The reported value of k_r=9,9·10^{-17} *cm^3 sites^{-1} s^{-1}* for X65 steel [3] can also provide wrong information about the X70 steel samples tested in the present work due to the possibility of slightly different yield strength, microstructure, alloying weighting etc.

As the Arrhenius relation is well reported [15, 28, 30, 43], the N_r values calculated by this relation was chosen as the main basis for comparison to previous values as described in Chapter 5. In Table 22, the Arrhenius results for the D_{eff} values from both the t_{lag} method and the trapping model are shown, revealing variations of N_r and E_b. The relation between the different materials was not affected by these variations.

6.2   Comparison of Fe3wt.%Si, X70 BM1, X70 HAZ1 and X70 BM2

Table 22: Arrhenius relation for the different materials. Number of reversible trapping sites N_r and binding energy for these sites E_b calculated by the Arrhenius equation 2.23. The results marked "[1]" are calculated based on the t_{lag} method, while the results marked "[2]" are calculated based on the trapping model.

| Material	Arrhenius relation [cm^2 s^{-1}]	N_r[sites cm^{-3}]	E_b [kJ mol^{-1}]
Fe 3wt.% Si Method 1	[1] $D = 0{,}0007\exp\left(\frac{-24{,}37kJmol^{-1}}{RT}\right)$ [2] $D = 0{,}0178\exp\left(\frac{-23{,}25kJmol^{-1}}{RT}\right)$	[1] $5{,}40\cdot10^{23}$ [2] $2{,}12\cdot10^{22}$	[1] 18,68 [2] 17,56
Fe 3wt.% Si Method 2	[1] $D = 0{,}0178\exp\left(\frac{-27{,}37kJmol^{-1}}{RT}\right)$ [2] $D = 0{,}1222\exp\left(\frac{-26{,}62kJmol^{-1}}{RT}\right)$	[1] $9{,}38\cdot10^{21}$ [2] $3{,}09\cdot10^{21}$	[1] 21,68 [2] 20,93
X70 BM1	[1] $D = 0{,}0178\exp\left(\frac{-26{,}69kJmol^{-1}}{RT}\right)$ [2] $D = 2{,}9361\exp\left(\frac{-32{,}25kJmol^{-1}}{RT}\right)$	[1] $1{,}27\cdot10^{21}$ [2] $1{,}29\cdot10^{20}$	[1] 24,00 [2] 26,56
X70 HAZ1	[1] $D = 0{,}0178\exp\left(\frac{-37{,}19kJmol^{-1}}{RT}\right)$ [2] $D = 3{,}3011\exp\left(\frac{-33{,}81kJmol^{-1}}{RT}\right)$	[1] $1{,}63\cdot10^{20}$ [2] $1{,}15\cdot10^{20}$	[1] 31,50 [2] 28,12
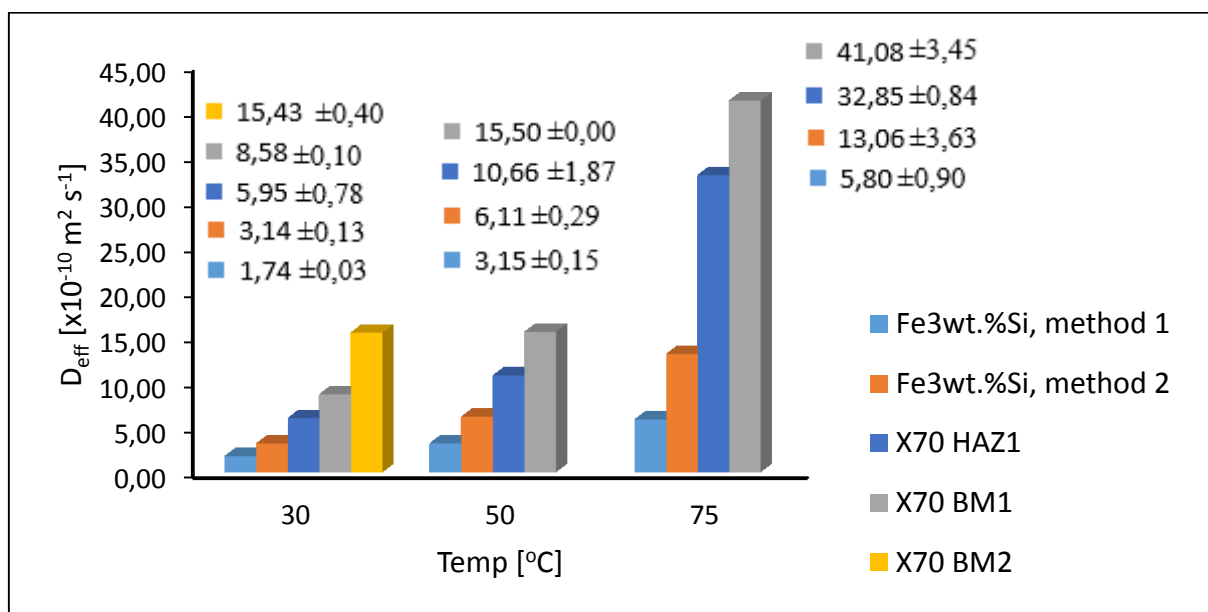
Figure 64: Comparison of the calculated D_{eff} from the trapping model for the different materials at each temperature. The D_{eff} presented is the mean value of the transients, with the standard deviation shown. Considering the same Fe3wt.%Si was used throughout the testing, the very first transients on BM1, BM2 and HAZ1 were not taken into consideration in this comparison to avoid irreversible trapping effects.

Table 22 and Figure 64 show the calculated N_r, E_b and D_{eff} for the different samples found by the Arrhenius relation and the trapping model.

Fe 3wt.% Si showed lower E_b and E_l than X70 steel, but an increased N_r compared to the X70 steel according to the Arrhenius relation. According to the microstructure, Fe3wt.%Si was assumed to show a higher D_{eff} because of the pure ferritic structure and the fact that phase boundaries may act as trapping sites [9] as mentioned in Section 2.6. Despite of this, Fe3wt.%Si generally showed a lower D_{eff} than the X70 steel. Fe3wt.%Si has a coarser grain structure than X70 steel as mentioned in Section 3.3.2. Fe3wt.%Si should therefore contain a lower number of these trapping sites than X70 due to a smaller amount of grain boundaries and the fact that grain boundaries may act as trapping sites as mentioned in Section 2.6. However, it has been suggested that grain boundaries may act as fast paths for hydrogen diffusion [46]. This may be one possible explanation the lower D_{eff} of Fe3wt.%Si compared to the X70 steel. For the results obtained with single anodic polarization between transients according to Method 1, the D_{eff} for Fe3wt.%Si was generally one order of magnitude smaller than for X70 BM1. The sub-surface concentration C_0 was fairly similar for the two materials.

As the results reported on the same X70 HAZ1 sample, sample 1, proved to be fairly stable and in accordance with the Arrhenius relation, they were used for further comparisons and conclusive remark. For the testing done on X70 HAZ1 sample 1-3, the D_{eff} proved to decrease

with increasing temperature between 30°C and 50°C, which means the results were not in accordance with the Arrhenius relation.

The X70 HAZ1 had a D_{eff} consequently lower than BM1, and a slightly higher C_0, which verified the previous results reported in Chapter 5. This result is plausible considering the fact that HAZ1 contains residual stress concentrations where the hydrogen will accumulate [9, 22] as mentioned in Section 2.2.3, in addition to the fact that a ferritic/bainitic microstructure will result in a lower D_{eff} than a ferritic/pearlitic microstructure as reported by Park et al [23]. The Arrhenius relation showed that HAZ1 had a slightly lower N_r than BM1, but higher E_b. A higher N_r was expected compared to the previous results reported in Chapter 5. According to the trapping model and equation 2.41, the calculated N_r for HAZ1 was actually slightly higher than for BM1.

The difference between BM1 and BM2 was not quite as expected. The D_{eff} at 30°C was actually slightly higher for BM2 than for BM1, and the C_0 slightly lower. The number of traps was assumed to increase because of the plastic deformation [18] as described in Section 2.8.2, and hence a lower D_{eff} was expected. According to equation 2.41, BM2 barely showed a higher N_r than BM1.

The "double plateau" behaviour in the first charging transient for the X70 steel samples was normally not seen simultaneously with an increased break through time. This only happened for BM2. Whether only "double plateau", only increased break through time or both behaviours occurred at the same time was assumed to be as a result of different binding energies in the traps of the different samples, as assumed by Fallahmohammadi [3, 31].

6.3   Comparison with previous results

The comparison of the steady state permeation current and steepness of the transients were done with respect to the testing of the X70 steel executed by Olden et al [43], as all data was available for comparison and could be plotted together with the present results as shown in Appendix B. The comparison of the calculated values for the materials are shown in Section 5.2.1-5.2.3. The difference shown in these sections for X70 steel could have originated from the fact that the steady state permeation current I_{ss} was lower in the present than in previous results, or the fact that many of the charging transients shown in a normalized flux vs. dimensionless time plot were less steep than Fick's curve and the previous results. These events will be highlighted and discussed in Section 6.3.1 and 6.3.2.

For Fe3wt.%Si, the difference compared to the previous results reported by Kumnick and Johnson [45] could originate from the events highlighted in Section 6.3.1 and 6.3.2, but this conclusion cannot be drawn due to lacking information about the previous results. Microstructural differences, grain size etc. are all factors that could have caused the difference in results.

6.3.1   Steady state permeation current

The most thorough comparison with the X70 high strength steel tested by Hauge and Olden et al [28, 43] revealed several differences, including a lower steady state permeation current as seen in Appendix B. When looking at the measured potential at the cathodic/charging side during the charging transients, it is clear that the potential in this work was higher than in the previous work for high temperatures. The charging in the previous work was done potentiostatically at a constant potential of -1050mV vs. Ag/AgCl. In this work, where the charging was done galvanostatically, the cathodic potential stabilized at a higher value for high temperatures. This is shown in Figure 65. At 75°C, the potential stabilized at approximately -1250V vs. Hg/Hg$_2$SO$_4$, which equals -800mV vs. Ag/AgCl. At 30°C, it stabilized on approximately -1500mV vs. Hg/Hg$_2$SO$_4$, which equals -1050mV vs. Ag/AgCl.
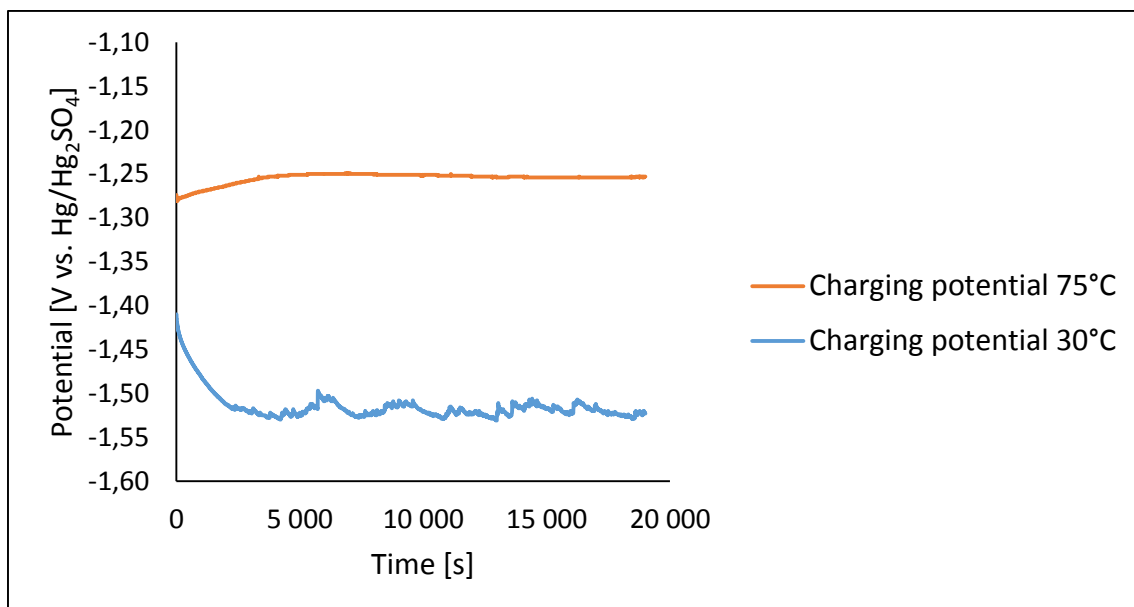

Figure 65: Cathodic charging potential measured at 30°C and 75°C.

The increase in potential indicated a lower amount of hydrogen atoms with the possibility of entering the metal on the charging side for the higher temperatures, meaning the cathodic protection (CP) conditions were not the same [8, 14]. This was a likely cause of the lowered permeation current for the higher temperatures, but could not explain the difference at lower temperatures. Therefore, another reason was assumed to be the dominating one.

The two main differences between the previous and present testing setup were the electrolyte used, and also the lack of a Pd coating on the anodic side in the present work. The electrolyte used in the testing done by Olden et al and Hauge [28, 43] was 0,1M NaOH, and a Pd layer was deposited on the anodic side of the testing sample. A Pd coating on the anodic side was originally assumed not to be necessary in this work as mentioned in Section 3.3.4, but this comparison might indicate that a deposited layer of Pd might be necessary after all to avoid the severely lowered permeation current. Figure 20 illustrates the effect of not using Pd coating, namely a lowered I_{ss}. For further description of the purpose of the Pd coating, see Section 3.3.4.

6.3.2   Shape of charging transients

Another big difference between the present and previous results was the steepness of the charging transients. This can easily be seen in the plot of normalized permeation flux vs. dimensionless time, shown in Appendix B. Compared to Fick's curve, the charging transients reported in the work by Olden et al [43] were steeper, while just about all the transients obtained in this work were less steep, including the transients for Fe 3wt.% Si. As mentioned in Section 2.6, a transient being less steep than Fick's curve is an indication of unsteady surface conditions [1]. The transients from the present work also showed different shapes for some of the tests, which again is an indication of a surface controlled diffusion [15]. By looking at the difference between the surface condition for the anodic and cathodic sides of the samples after testing as shown in Section 4.3, it is possible to search for possible explanations.

First of all, the formation of an oxide layer discovered on the sample surfaces could be a reason for why some of the transients decreased after reaching the maximum steady state permeation current as reported by Kupka et al [29].

At the anodic surface of X70 HAZ1 sample 1, localized corrosion in the form of pitting was discovered. A reason for this could be that impurities present in the material acted as sites for the pitting corrosion, meaning that a passive layer formed during the anodic polarization in the passive range of the material was broken at the impurity sites. For Fe3wt.%Si, less evidence of pitting was seen on the anodic surface, which means that there should be less impurities in the Fe3wt.%Si sample according to the suggested theory. The Fe3wt.%Si material contains more

alloying elements than X70 steel, but less grain boundaries due to larger grains. Impurities will segregate to the iron grain boundaries [47], which opens the possibility for more impurities in the X70 steel samples. The fact that pitting occurs more frequently at impurity sites has been reported by Bardal [8] among others.

At the cathodic side of both the Fe3wt.%Si sample and X70 HAZ1 sample, the microstructure was revealed. The surface had been etched. As discovered in Section 4.3.2, an oxide layer formed on the samples before submersing them in electrolyte. A possible (simplified) explanation to this etching might be:

First hydrogen charging: Oxide layer removal during cathodic charging. The reduction of the oxide layer will be the cathode reaction until the layer is removed due to the lowering in potential [8].

OCP after first charging: No protective layer on the cathodic surface. Corrosion might occur as the surface is exposed and no passive oxide layer is present [8].

Second hydrogen charging: The ions present as a result of the corrosion will be reduced, and deposited back on the surface.

This means that the surface conditions on the cathodic side will change for each charging transient. The surface corrodes in one step and the ions get reduced and deposited on the surface in the next step, enabling the possibility of different shapes of the different charging transients for each test. This removal of material by corrosion might be a reason for why the surface had an etched appearance.

However, no significant amounts of iron ions were discovered in the solution. Considering that each test was ended after the final discharge transients, i.e. by monitoring the OCP on the cathodic side, it would be reasonable to assume that iron ions should be detected according to the suggested theory. The amount of iron ions, on the other hand, could in fact be so small that it was not detected. This suggests that the yellow colour discovered for the cathodic electrolyte had another explanation than iron ions, e.g. that the very dirty, yellow water from the bath had leaked in. When diluting the electrolyte with water prior to testing to obtain desired viscosity and resistivity, the resistivity decreased. In the polluted electrolyte, the resistivity had increased compared to the measured value before testing. Therefore, the fact that the reason for the pollution could be water from the bath leaking into the cell was originally unlikely. However, the water from the bath was dirty and severely polluted, meaning the possibility of this water increasing the resistivity instead of decreasing it could not be ruled out.

This theory rules out the method of double anodic polarization between transients, Method 2, as a reason for the pollution of the electrolyte. In fact, to avoid ever having to apply OCP, the

method of double anodic polarization between transients is a possible measure in order to try to avoid the etching phenomenon.

Further investigation of this phenomenon is highly recommended, as the theory presented in this section is only a vague hypothesis.

Because of the highlighted differences in steady state permeation current density and steepness of the normalized permeation transients, the difference in calculated D_{eff} and C_0 values compared to previous results should probably not be that highly emphasized. The basis for comparison will therefore be somewhat poor when a surface controlled diffusion is suspected to have been the case.

Chapter 7

Conclusion

- The effective hydrogen diffusion coefficient, D_{eff}, for Fe3wt.%Si at a temperature range of 30°C-75°C varied from $3,77 \cdot 10^{-11}$ to $3,88 \cdot 10^{-10}$ $m^2\ s^{-1}$ according to the t_{lag} method [1], and from $1,69 \cdot 10^{-10}$ to $1,75 \cdot 10^{-9}$ $m^2\ s^{-1}$ according to the trapping model developed by Iino [3-6] according to the two testing methods presented.

- D_{eff} for X70 BM1 at a temperature range of 30°C-75°C varied from $2,01 \cdot 10^{-10}$ to $9,85 \cdot 10^{-10}$ $m^2\ s^{-1}$ according to the t_{lag} method, and from $8,47 \cdot 10^{-10}$ to $4,77 \cdot 10^{-9}$ $m^2\ s^{-1}$ according to the trapping model.

- D_{eff} for X70 HAZ1 at a temperature range of 30°C -75°C varied from $1,05 \cdot 10^{-10}$ to $7,53 \cdot 10^{-10}$ $m^2\ s^{-1}$ according to the t_{lag} method, and from $5,00 \cdot 10^{-10}$ to $3,39 \cdot 10^{-9}$ $m^2\ s^{-1}$ according to the trapping model.

- D_{eff} for X70 BM2 at a temperature of 30°C varied from $2,24 \cdot 10^{-10}$ to $3,33 \cdot 10^{-10}$ $m^2\ s^{-1}$ according to the t_{lag} method, and from $8,21 \cdot 10^{-10}$ to $1,59 \cdot 10^{-9}$ $m^2\ s^{-1}$ according to the trapping model.

- D_{eff} was higher for X70 steel than for Fe3wt.%Si, meaning a single phase ferritic microstructure showed lower diffusivity than a dual phase microstructure, an unexpected result based on the fact that phase boundaries may act as trapping sites. However, the stated fact that grain boundaries may act as fast paths for hydrogen might have been a reasonable explanation considering X70 steel has a finer grain structure.

- D_{eff} was slightly higher for X70 BM1 than HAZ1, confirming that a coarse grained HAZ microstructure, assumed to consist of Bainite/Ferrite, showed lower hydrogen diffusion than BM1, which was assumed to consist of Ferrite/Pearlite. This is comparable with both previous results and the assumption that the higher level of residual stresses in HAZ will reduce the diffusivity.

- D_{eff} increased with increasing pre-strain level for X70 BM1 and BM2, an unexpected result considering that increased pre-strain level is assumed to increase the number of traps and hence lower the D_{eff}. Previous results and statements could not be verified by the present results.

- The method of partial charge provided a good fit of the transient to Fick's curve, meaning this method was proven to be fairly representative of lattice diffusion. The D_{eff} for the partial charge of X70 BM1 at 75°C varied from $7,11 \cdot 10^{-10}$ to $1,16 \cdot 10^{-9}$ $m^2\ s^{-1}$ according to the t_{lag} method, and from $4,47 \cdot 10^{-10}$ to $1,80 \cdot 10^{-9}$ $m^2\ s^{-1}$ according to the trapping model.

- The sub-surface concentration, C_0, was fairly unaffected by the different material types, except for X70 HAZ1 which showed a higher C_0. C_0 for Fe3wt.%Si, X70 BM1 and X70 BM2 varied from $8,58 \cdot 10^{-3}$ to $6,18 \cdot 10^{-2}$ $ppm\ W$ according to the D_{eff} from the t_{lag} method and from $1,89 \cdot 10^{-3}$ to $2,03 \cdot 10^{-2}$ $ppm\ W$ according to the D_{eff} from the trapping model.

For X70 HAZ1, it varied from $3,82 \cdot 10^{-2}$ to $1,33 \cdot 10^{-1}$ *ppm W* according to the D_{eff} from the t_{lag} method and from $9,12 \cdot 10^{-3}$ to $2,45 \cdot 10^{-2}$ *ppm W* according to the D_{eff} from the trapping model. For the X70 steel, this suggested that the C_0 was fairly unaffected by pre-strain level, but affected by the heat affected zone (HAZ).

- According to the Arrhenius relation based on D_{eff} from the trapping model, the density of reversible trapping sites, N_r, was $2,12 \cdot 10^{22}$ and $3,09 \cdot 10^{21}$ *sites cm^{-3}* for Fe3wt.%Si according to the two different testing methods presented, respectively. For X70 BM1, this was $1,29 \cdot 10^{20}$ *sites cm^{-3}*, while for X70 HAZ1 it was $1,15 \cdot 10^{20}$ *sites cm^{-3}*. A higher density of trapping sites for X70 BM1 compared to HAZ1 was unexpected based on previous results and the assumption that HAZ1 contains a higher level of residual stress concentrations where the hydrogen is assumed to accumulate.

- According to the Arrhenius relation based on D_{eff} from the trapping model, the binding energy for reversible traps, E_b, was 17,56 and 20,93 *kJ mol^{-1}* for Fe3wt.%Si according to the two different testing methods presented, respectively. For X70 BM1, this was 26,56 *kJ mol^{-1}*, while for X70 HAZ it was 28,12 *kJ mol^{-1}*. This confirmed that HAZ1 showed a higher trap binding energy than BM1, which was expected based on the previously reported results.

- A lower steady state permeation current compared to previous results was seen for all the tests, in addition to just about all the charging transients being less steep than the ideal Fick's curve. This indicated unsteady surface conditions throughout the presented experimental testing. Different shapes of the transients obtained in the same tests were also an indication of a surface controlled diffusion. Formation of an oxide layer in addition to carbon contamination was discovered on both sides of the samples. In addition to this, pitting was discovered on the anodic sample side while etching was discovered on the cathodic sample side.

Chapter 8

Further work

- Provide further testing on X70 BM2 to provide a full Arrhenius relation, and also redo the test at 30°C because of the unexpected results reported in this work.

- Provide further testing with the electrolyte used in this work to learn the possible effects on the results compared to earlier reported diffusion results with standard electrolytes. This involves identifying the exact surface conditions that occur during testing, and work towards overcoming any unwanted surface effects. XPS (X-ray Photoelectron Spectroscopy) will be a suited method for a more thorough surface investigation.

- Try to deposit a palladium layer (Pd coating) on the anodic side to see if it will affect the results as suggested by Manolatos et al [41]. If so, executing the experimental work reported in this thesis over again is recommended to obtain more reliable results.

- Try avoiding to avoid switching to OCP measurement on the cathodic side after the hydrogen charging, and investigate if the etching of the cathodic surface can be avoided.

- Test different degrees of pre-straining for both BM and HAZ samples (even go as high as 10%). Also test several degrees of pre-straining at different temperatures.

- Test all the samples by the partial charge method.

Bibliography

1.   G148-97, A., *Standard Practice for Evaluation of Hydrogen Uptake, Permeation, and Transport in Metals by an Electrochemical Technique.* 2003.

2.   Hope, M.B., *Hydrogen uptake in steel.* 2014, Norwegian University of Science and Technology: Trondheim, Norway.

3.   Fallahmohammadi, E., *Diffusion and trapping of hydrogen in pipeline steels.* 2014, Politecnico di Milano: Italy.

4.   Iino, M., *Analysis of irreversible hydrogen trapping.* Acta Metallurgica, 1982. **30**(2): p. 377-383.

5.   Iino, M., *A more generalized analysis of hydrogen trapping.* Acta Metallurgica, 1982. **30**(2): p. 367-375.

6.   Simonsen, B.W., *An application prototype for hydrogen permeation data analysis.* 2015, Norwegian University of Science and Technology: Trondheim, Norway.

7.   Callister, W.D. and D.G. Rethwisch, *Materials Science and Engineering.* 8 ed. 2011: John Wiley & Sons (Asia) Pte Ltd.

8.   Bardal, E., *Korrosjon og korrosjonsvern.* 2 ed. 1994, Trondheim: Tapir Akademiske Forlag.

9.   Olden, V., C. Thaulow, and R. Johnsen, *Modelling of hydrogen diffusion and hydrogen induced cracking in supermartensitic and duplex stainless steels.* Materials & Design, 2008. **29**(10): p. 1934-1948.

10.   Turnbull, A., M.W. Carroll, and D.H. Ferriss, *Analysis of hydrogen diffusion and trapping in a 13% chromium martensitic stainless steel.* Acta Metallurgica, 1989. **37**(7): p. 2039-2046.

11.   Barnoush, A., *Hydrogen Embrittlement.* 2011, Saarland University.

12.   ISO, *ISO 21457 Petroleum, petrochemical and natural gas industries - materials selection and corrosion control for oil and gas production systems.*

13.   Lynch, S.P., *Progress Towards Understanding Mechanisms Of Hydrogen Embrittlement And Stress Corrosion Cracking.* NACE International.

14.   Xie, J., et al., *Hydrogen Effects On High Strength Pipeline Steels.* NACE International.

15.   Smirnova, A., *Hydrogen permeation in 13% Cr super martensitic stainless steel and API X70 pipeline steel.* 2010, Norwegian University of Science and Technology: Trondheim.

16. Benassi, G., *Critical analysis of hydrogen permeation techniques. Application to different steel microstructures.* 2013, Politecnico di Milano: Italy.

17. Okwurdiri, E., *Hydrogen diffusion in pipeline steels*. 2011, Politecnico di Milano: Italy.

18. Kim, S.J. and K.Y. Kim, *A review of corrosion and hydrogen diffusion behaviors of high strength pipe steel in sour environments.* Journal of Welding and Joining, 2014. **32**(5).

19. Kawashima, A., K. Hashimoto, and S. Shimodaira, *Hydrogen Electrode Reaction and Hydrogen Embrittlement of Mild Steel in Hydrogen Sulfide Solutions.* Corrosion, 1976. **32**(8): p. 321-331.

20. Zheng, S., et al., *Effects of the Temperature on the Hydrogen Permeation Behaviours of L360NCS Pipeline Steel in 1MPa H 2 S Environments.* International Journal of Electrochemical Science, 2013. **8**(2).

21. Hodgkiess, T., *Cathodic protection*. 2013, University of Glasgow: Glasgow.

22. Wang, S.H., et al., *Hydrogen permeation in a submerged arc weldment of TMCP steel.* Materials Chemistry and Physics, 2003. **77**(2): p. 447-454.

23. Park, G.T., et al., *Effect of microstructure on the hydrogen trapping efficiency and hydrogen induced cracking of linepipe steel.* Corrosion Science, 2008. **50**(7): p. 1865-1871.

24. Dowling, N., *Mechanical behavior of materials.* 4 ed. 2013, Virginia: Pearson Education Limited.

25. Porter, D., K. Easterling, and M. Sherif, *Phase transformation in metals and alloys*. 3 ed. 2009: Taylor & Francis group.

26. Crank, J., *The mathematics of diffusion*. Vol. 2. 1975: Clarendon press Oxford.

27. Devanathan, M.A.V. and Z. Stachurski, *The Adsorption and Diffusion of Electrolytic Hydrogen in Palladium*. Vol. 270. 1962. 90-102.

28. Hauge, A., *Hydrogen embrittlement in subsea pipelines made from X70 - effect of plastic deformation on hydrogen diffusion*. 2011, Norwegian University of Science and Technology: Trondheim.

29. Kupka, M., K. Stępień, and K. Nowak, *Studies on hydrogen diffusivity in iron aluminides using the Devanathan–Stachurski method.* Journal of Physics and Chemistry of Solids, 2014. **75**(3): p. 344-350.

30. Skjellerudsveen, M., et al., *Effect of Microstructure and Temperature on HydrogenDiffusion and Trapping in X70 grade Pipeline Steel and itsWeldments.* 2010.

31. Fallahmohammadi, E., F. Bolzoni, and L. Lazzari, *Measurement of lattice and apparent diffusion coefficient of hydrogen in X65 and F22 pipeline steels.* International Journal of Hydrogen Energy, 2013. **38**(5): p. 2531-2543.

32. Oriani, R.A., *The diffusion and trapping of hydrogen in steel.* Acta Metallurgica, 1970. **18**(1): p. 147-157.

33. Kiuchi, K. and R.B. McLellan, *The solubility and diffusivity of hydrogen in well-annealed and deformed iron.* Acta Metallurgica, 1983. **31**(7): p. 961-984.

34. Thomas, P. and E. Stern, *Efficient numerical modelling of hydrogen diffusion with trapping.* Journal of Materials Science, 1981. **16**(11): p. 3122-3130.

35. McNabb, A. and P. Foster, *A new analysis of the diffusion of hydrogen in iron and ferritic steels.* Trans. Aime, 1963. **227**: p. 618.

36. Zakroczymski, T., *Adaptation of the electrochemical permeation technique for studying entry, transport and trapping of hydrogen in metals.* Electrochimica Acta, 2006. **51**(11): p. 2261-2266.

37. DNV, *DNV-OS-F101 Pipeline standard.*

38. Hardie, D., E.A. Charles, and A.H. Lopez, *Hydrogen embrittlement of high strength pipeline steels.* Corrosion Science, 2006. **48**(12): p. 4378-4385.

39. Sofronis, P., Y. Liang, and N. Aravas, *Hydrogen induced shear localization of the plastic flow in metals and alloys.* European Journal of Mechanics - A/Solids, 2001. **20**(6): p. 857-872.

40. Hillenbrand, H.G. and M.K. Gräf, C. *Development and production of high strength pipeline steels.* 2001.

41. Manolatos, P., M. Jerome, and J. Galland, *Necessity of a palladium coating to ensure hydrogen oxidation during electrochemical permeation measurements on iron.* Electrochimica Acta, 1995. **40**(7): p. 867-871.

42. Loveday, D., *Ca Overload*, M.B. Hope, Editor. 2015: Personal communication.

43. Olden, V., et al., *Influence of plastic strain on the effective hydrogen diffusion and trapping in X70 steel.* Norwegian University of Science and Technology, NTNU: Trondheim, Norway.

44. Flinn Scientific, i. *Colorful iron complexes.* 2009.

45. Kumnick, A.J. and H.H. Johnson, *Hydrogen transport through annealed and deformed armco iron.* Metallurgical Transactions, 1974. **5**(5): p. 1199-1206.

46. Kimura, A. and H.K. Birnbaum, *Hydrogen induced grain boundary fracture in high purity nickel and its alloys—Enhanced hydrogen diffusion along grain boundaries.* Acta Metallurgica, 1988. **36**(3): p. 757-766.

98

47.   Braithwaite, J.S. and P. Rez, *Grain boundary impurities in iron.* Acta Materialia, 2005. **53**(9): p. 2715-2726.

Appendix A

Polarization curves for Fe3wt.%Si and X70 BM1

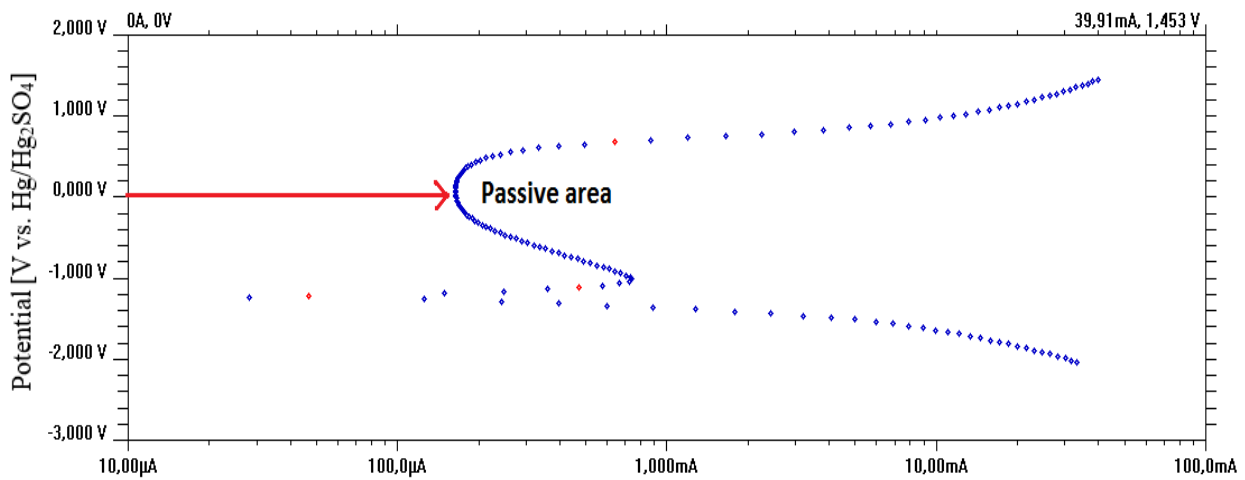
Figure A 1: Polarization curve for Fe3wt.%Si rev Current [mA] ' vs. Hg/Hg$_2$SO$_4$ is in the passive area of the curve.

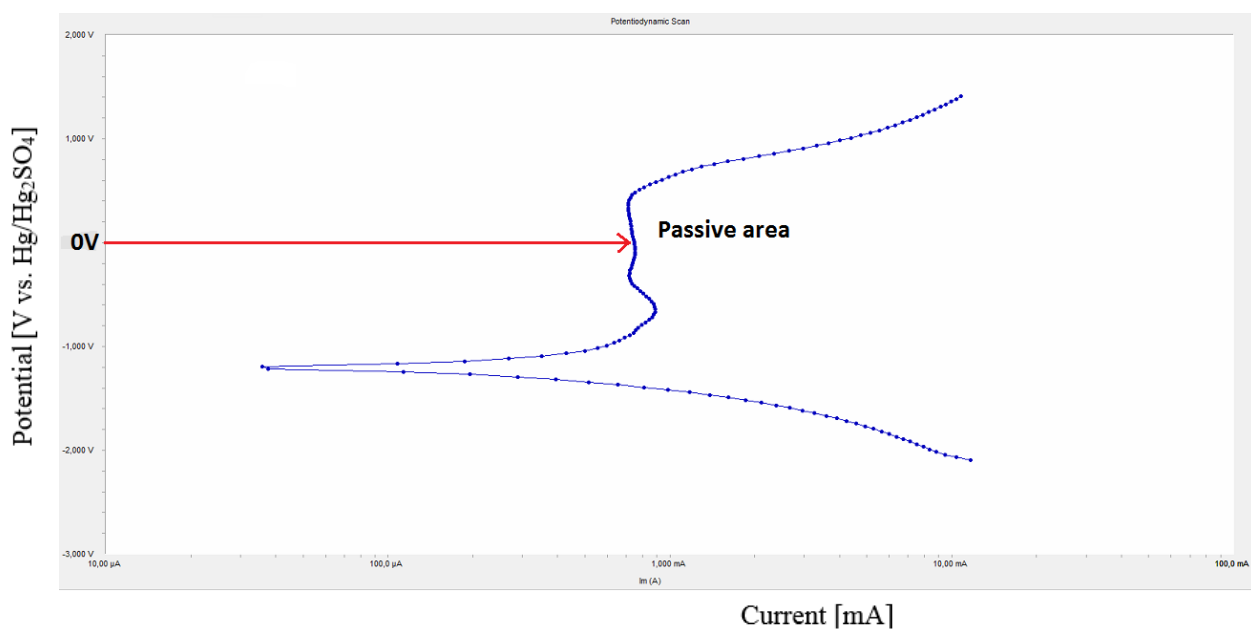Figure A 2: Polarization curve for X70 BM1 revealing that 0V vs. Hg/Hg$_2$SO$_4$ is in the passive area of the curve.

100

Appendix B

Detailed permeation plots

B.1   Detailed plots for Fe3wt.%Si – anodic current vs. time

B.1.1   Method 1: Single anodic polarization between transients
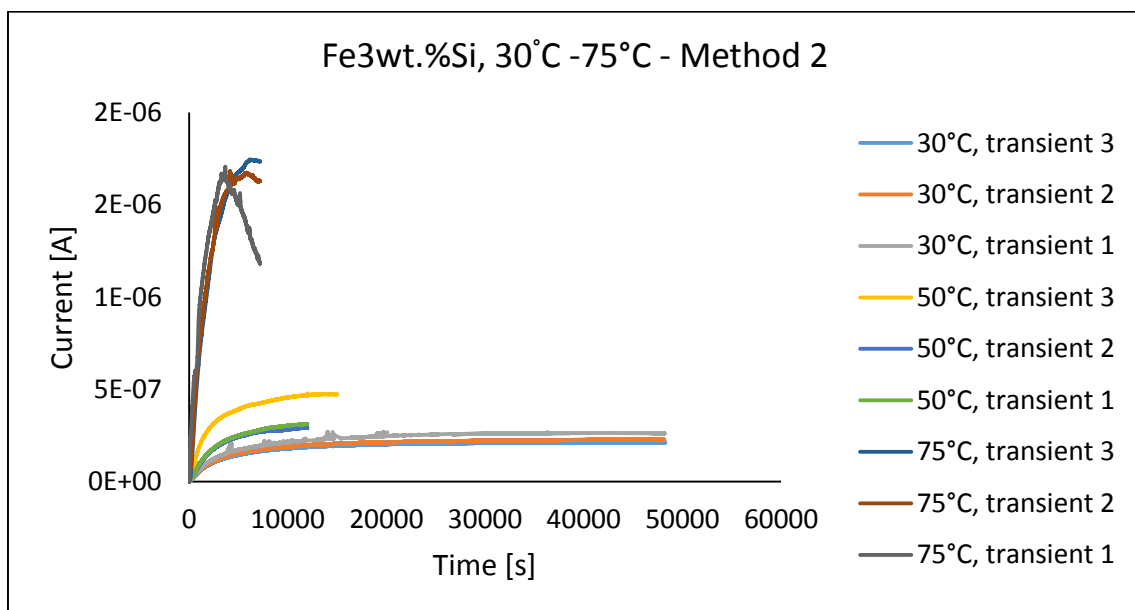
Figure B 1: Anodic current vs. time for Fe3wt.%Si according to Method 1 at a temperature range of 30°C-75°C.

B.1.2 Method 2: Double anodic polarization between transients
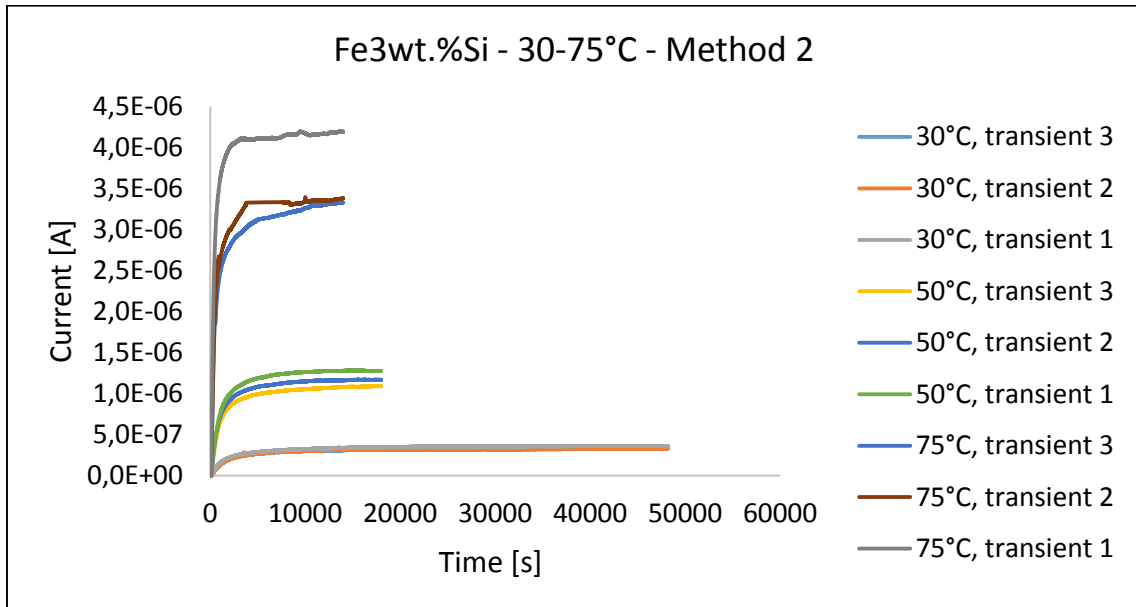
Figure B 2: Anodic current vs. time for Fe3wt.%Si according to Method 2 at a temperature range of 30°C-75°C.
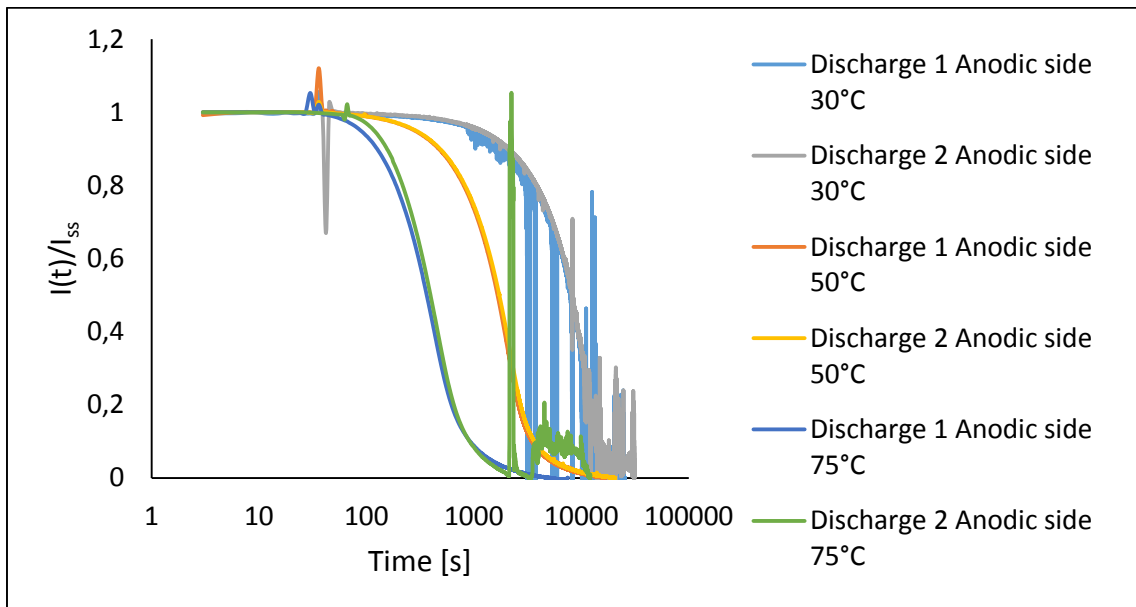
Figure B 3: Normalized discharge current on the anodic vs. time. Obtained at a temperature range of 30°C-75°C.
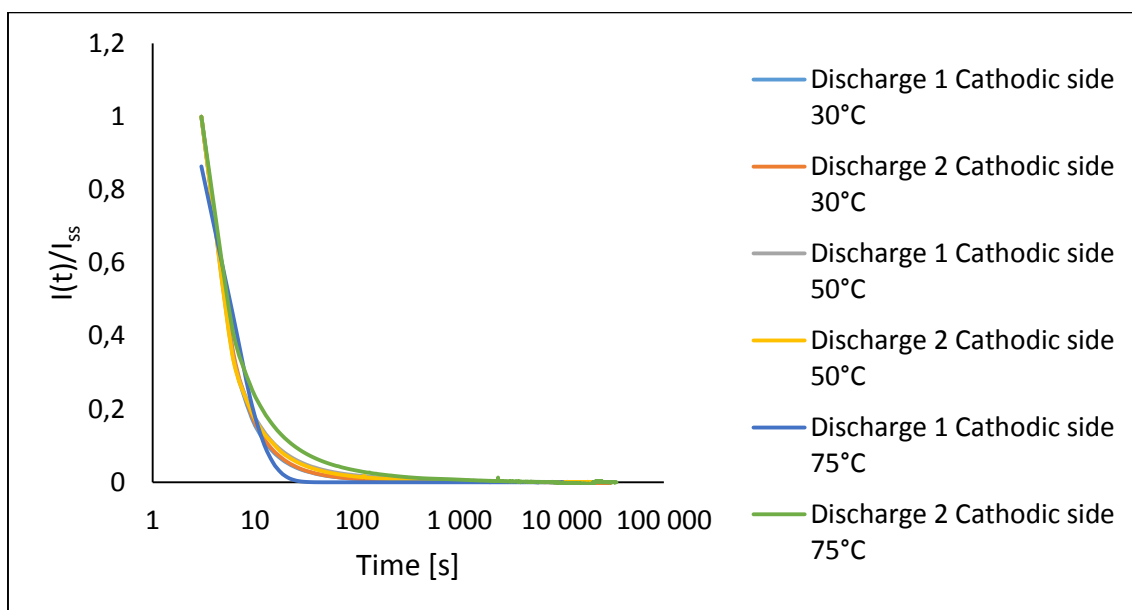
Figure B 4: Normalized discharge current on the cathodic vs. time. Obtained at a temperature range of 30°C-75°C.

B.1.3   Varying the charging current density
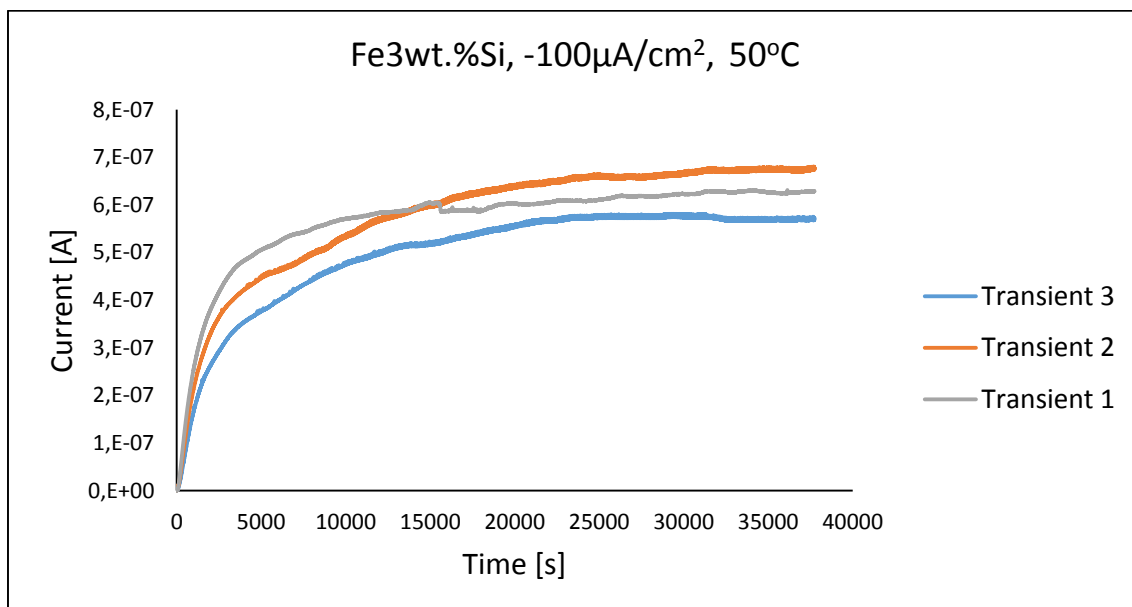
Figure B 5: Anodic current vs. time for Fe3wt.%Si according to Method 1 at a temperature of 50°C with a cathodic charging current density of -100µAcm^{-2}.

104
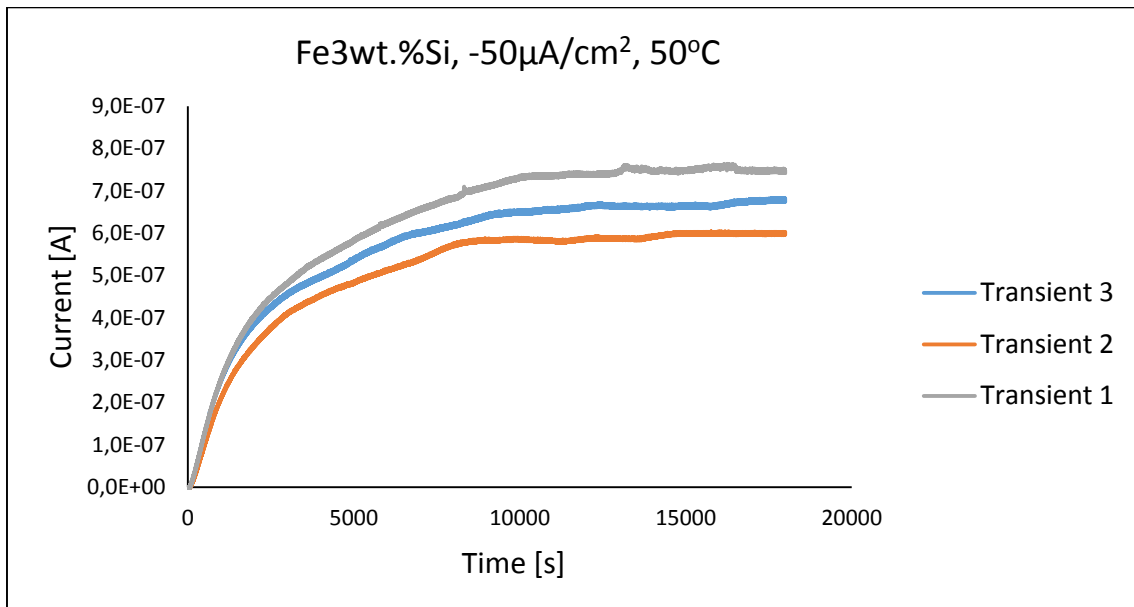
Figure B 6: Anodic current vs. time for Fe3wt.%Si according to Method 1 at a temperature of 50°C with a cathodic charging current density of -50µAcm^{-2}.
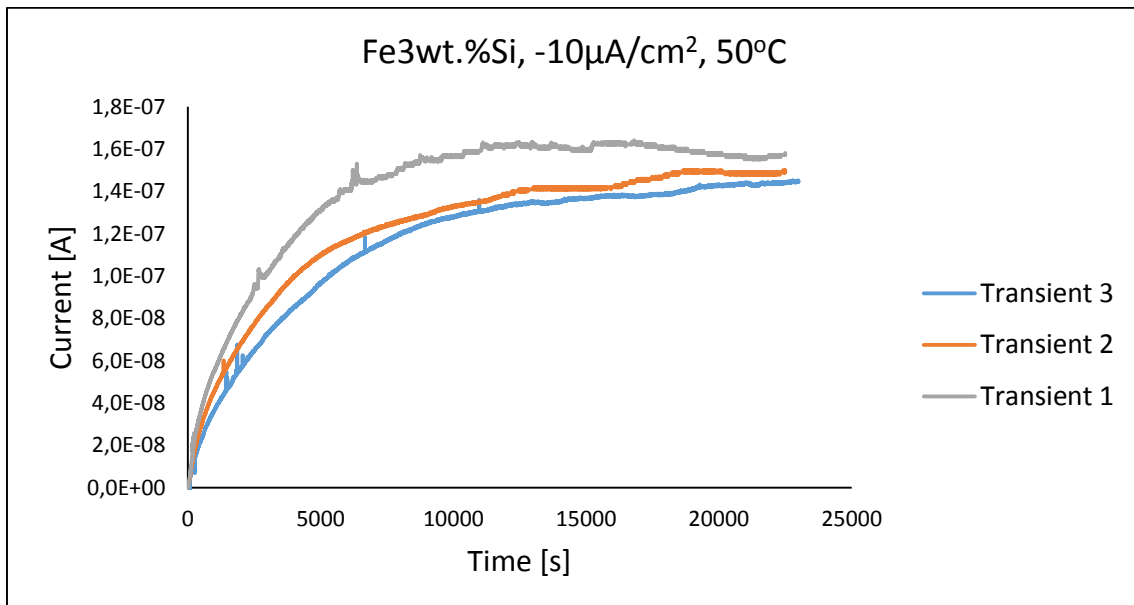
Figure B 7: Anodic current vs. time for Fe3wt.%Si according to Method 1 at a temperature of 50°C with a cathodic charging current density of -10µAcm^{-2}.
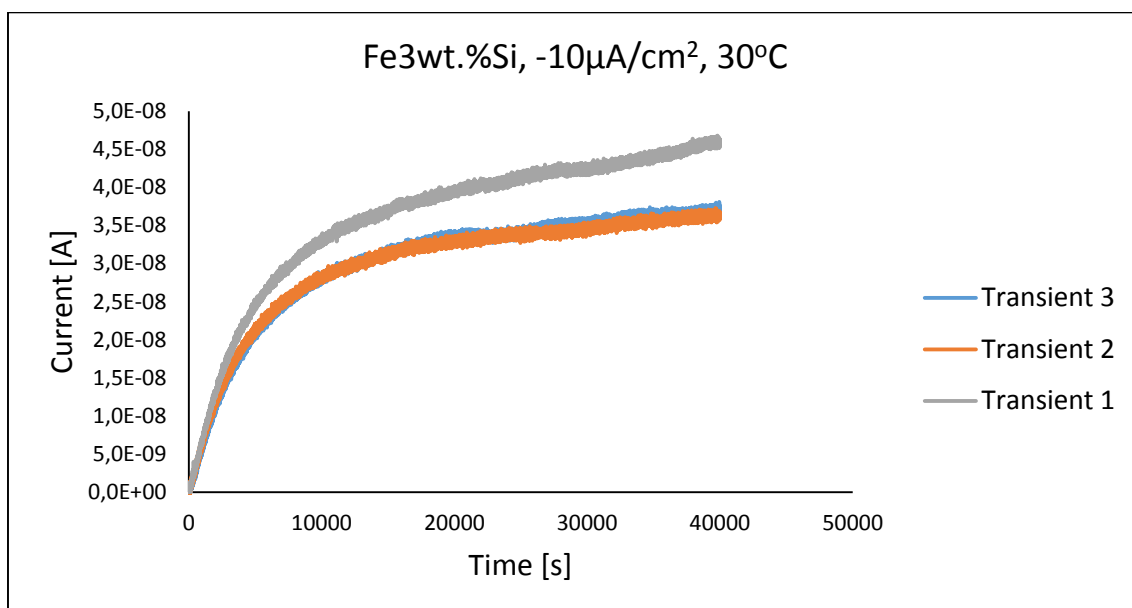
Figure B 8: Anodic current vs. time for Fe3wt.%Si according to Method 1 at a temperature of 30°C with a cathodic charging current density of -10µAcm^{-2}.

B.2 Detailed permeation plots for X70 steel in comparison with previous results

B.2.1 BM1 (0% strain)

Figure B 9: Anodic current density vs. time for X70 BM1 at a temperature of 25°C -30°C. The results from present work are from X70 BM1 sample 1.

Figure B 10: Normalized permeation flux vs. dimensionless time for X70 BM1 at a temperature of 25°C-30°C. The results from present work are from X70 BM1 sample 1.
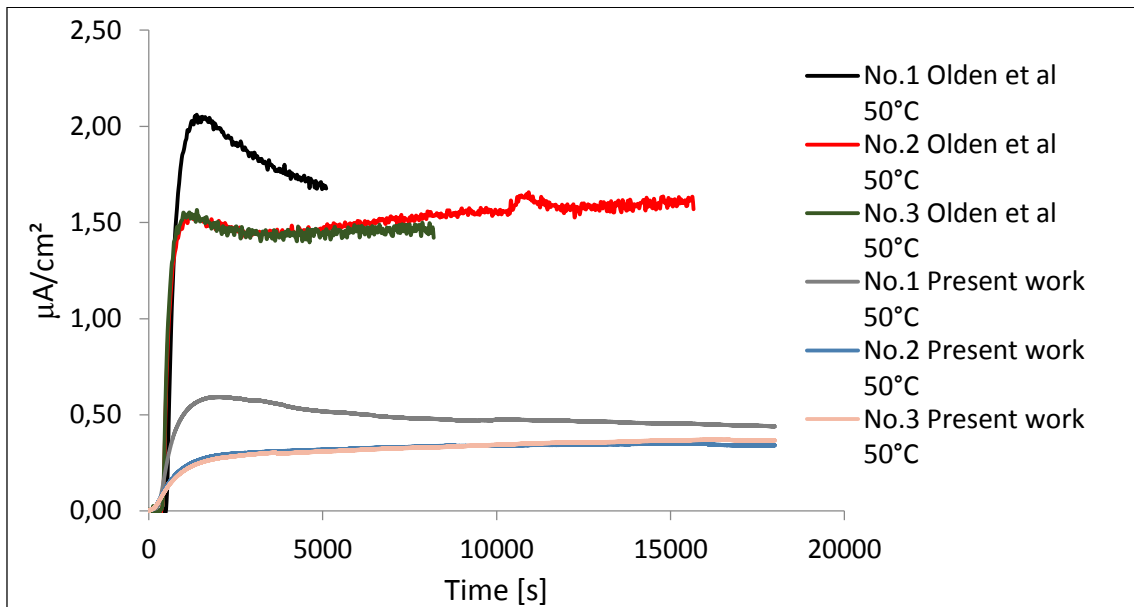
Figure B 11: Anodic current density vs. time for X70 BM1 at a temperature of 50˚C. The results from present work are from X70 BM1 sample 2.
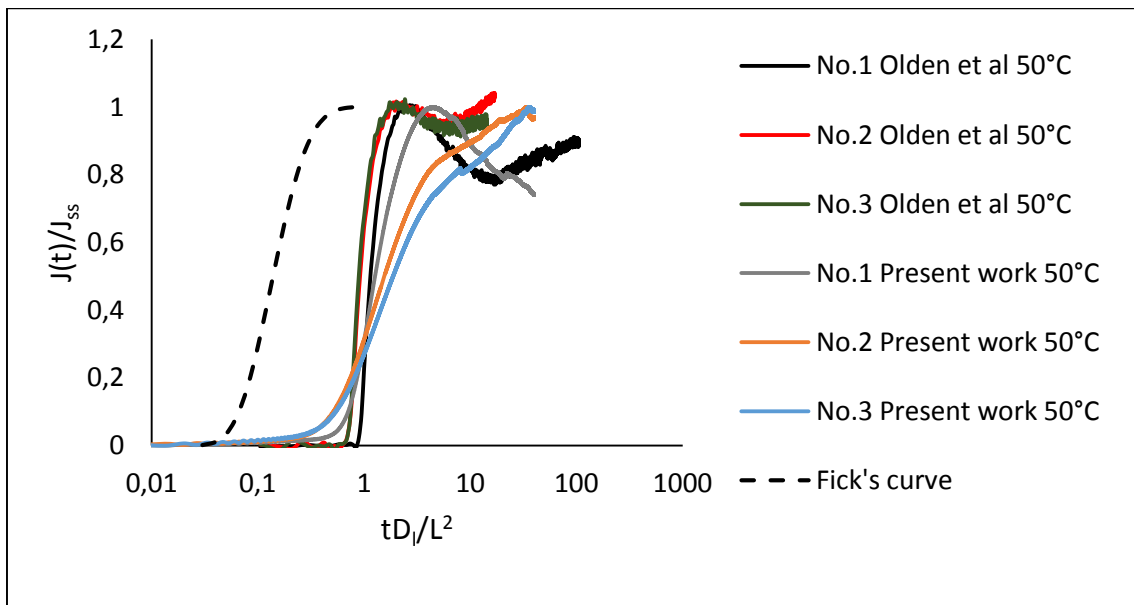
Figure B 12: Normalized permeation flux vs. dimensionless time for X70 BM1 at a temperature of 50˚C. The results from present work are from X70 BM1 sample 2.
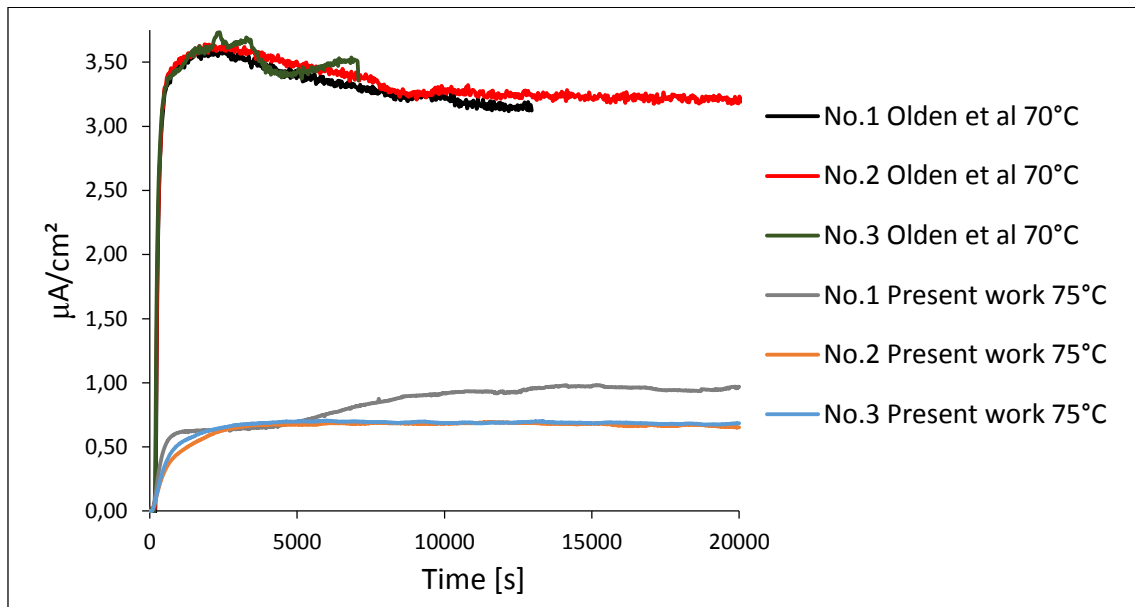
Figure B 13: Anodic current density vs. time for X70 BM1 at a temperature of 70°C-75°C. The results from present work are from X70 BM1 sample 3.
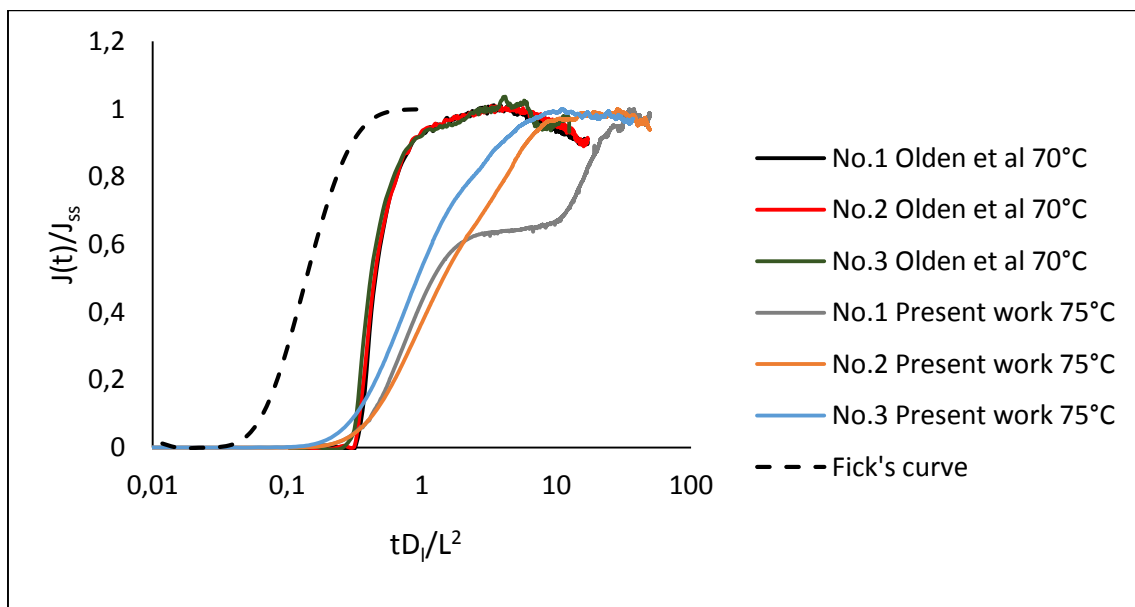
Figure B 14: Normalized permeation flux vs. dimensionless time for X70 BM1 at a temperature of 70°C-75°C. The results from present work are from X70 BM1 sample 3.

B.2.2   HAZ1 (0%strain)
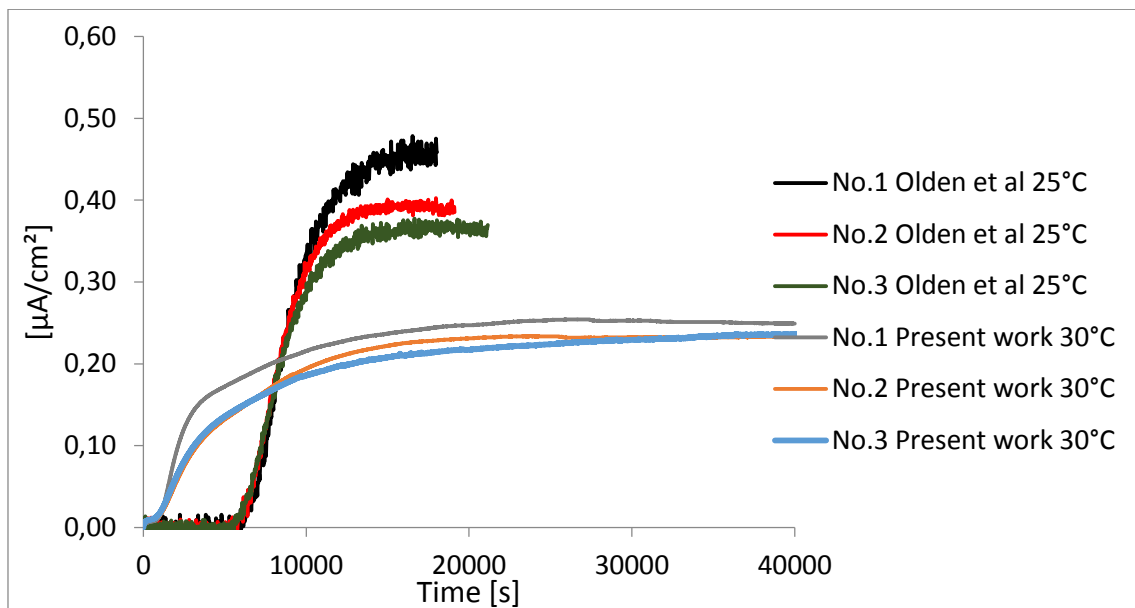
Figure B 15: Anodic current density vs. time for X70 HAZ1 at a temperature of 25°C-30°C. The results from present work are from X70 HAZ1 sample 1.
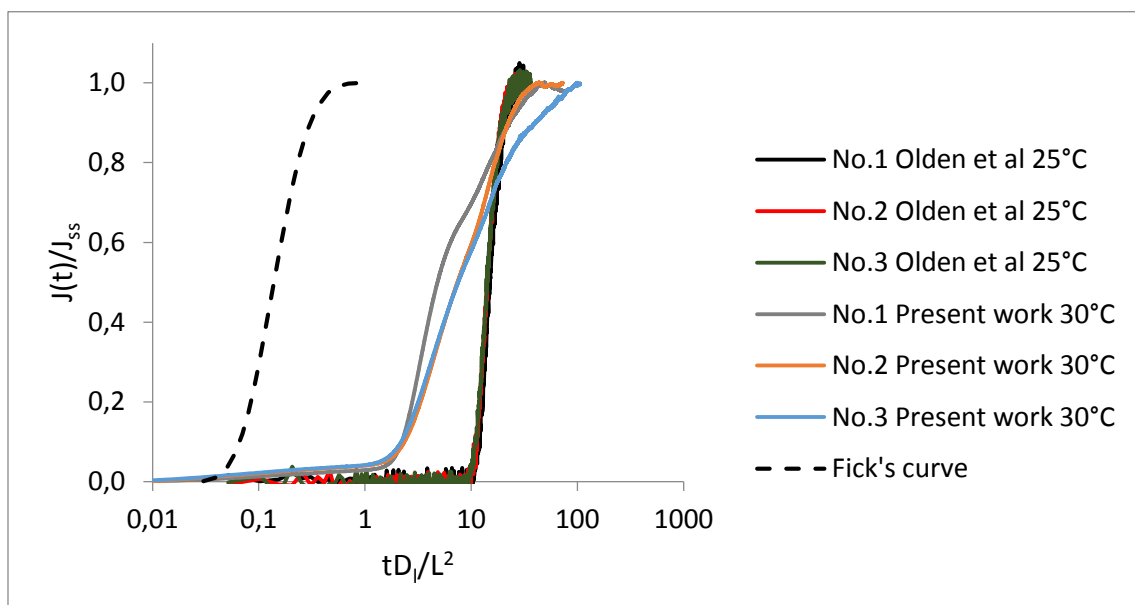
Figure B 16: Normalized permeation flux vs. dimensionless time for X70 HAZ1 at a temperature of 25°C-30°C. The results from present work are from X70 HAZ1 sample 1.
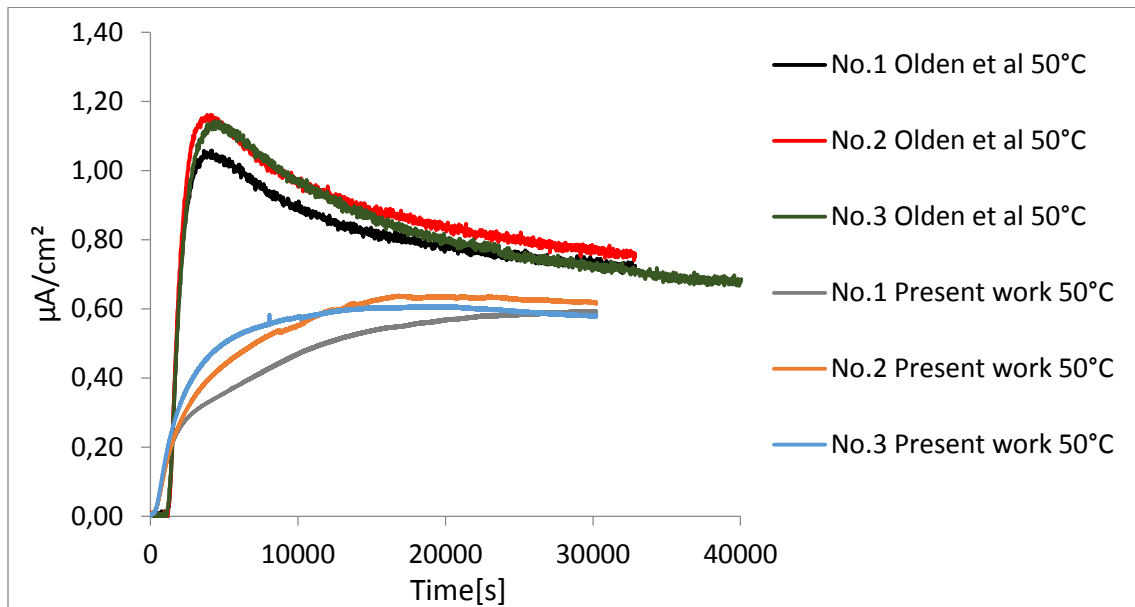
Figure B 17: Anodic current density vs. time for X70 HAZ1 at a temperature of 50°C. The results from present work are from X70 HAZ1 sample 1.
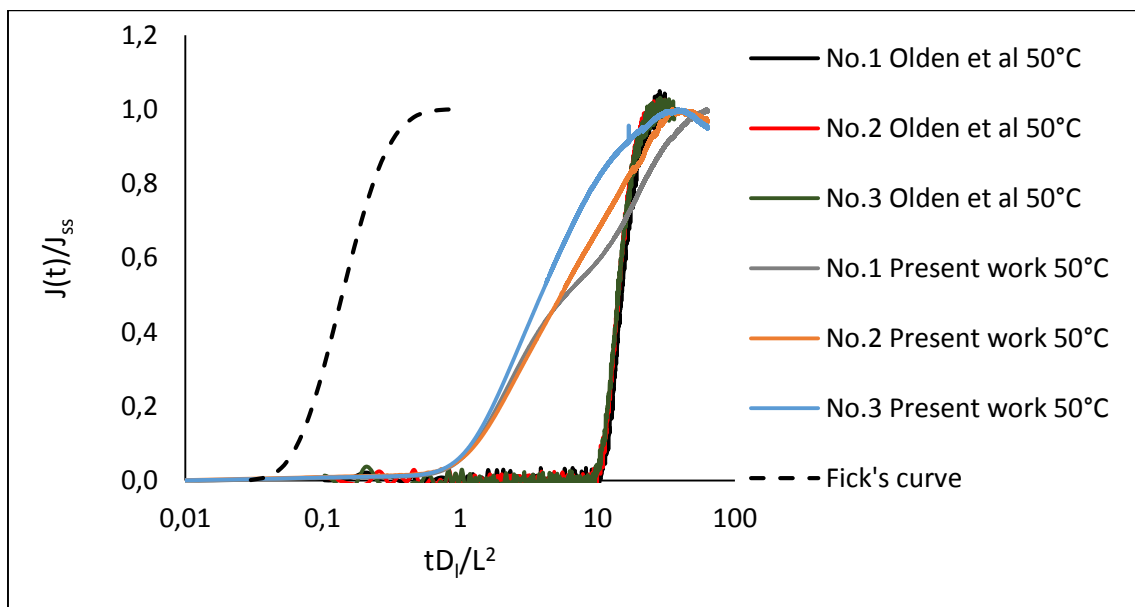
Figure B 18: Normalized permeation flux vs. dimensionless time for X70 HAZ1 at a temperature of 50°C. The results from present work are from X70 HAZ1 sample 1.
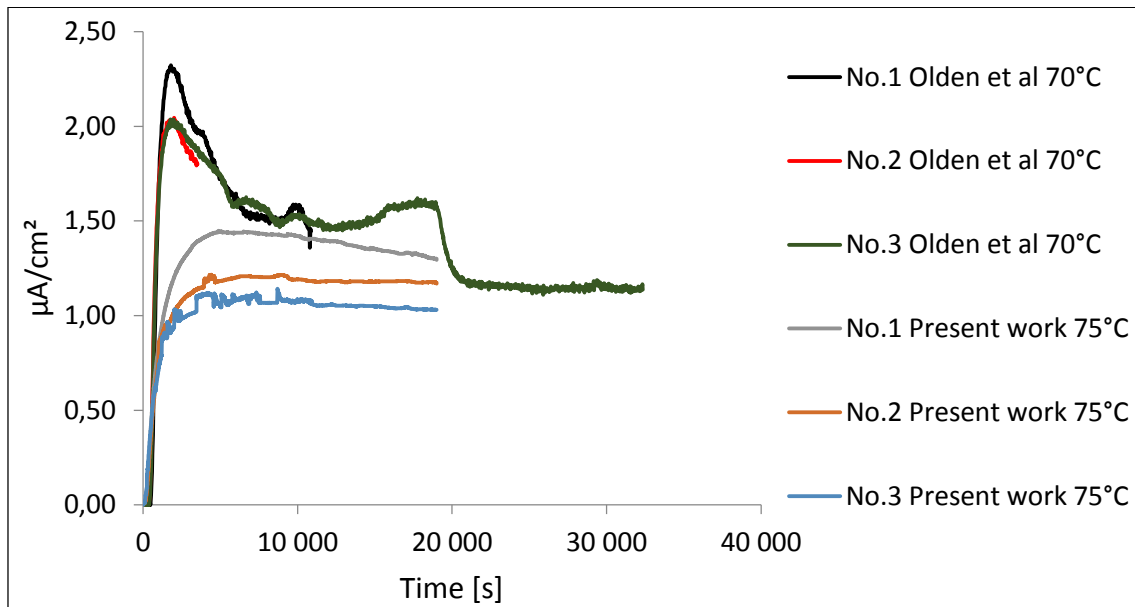
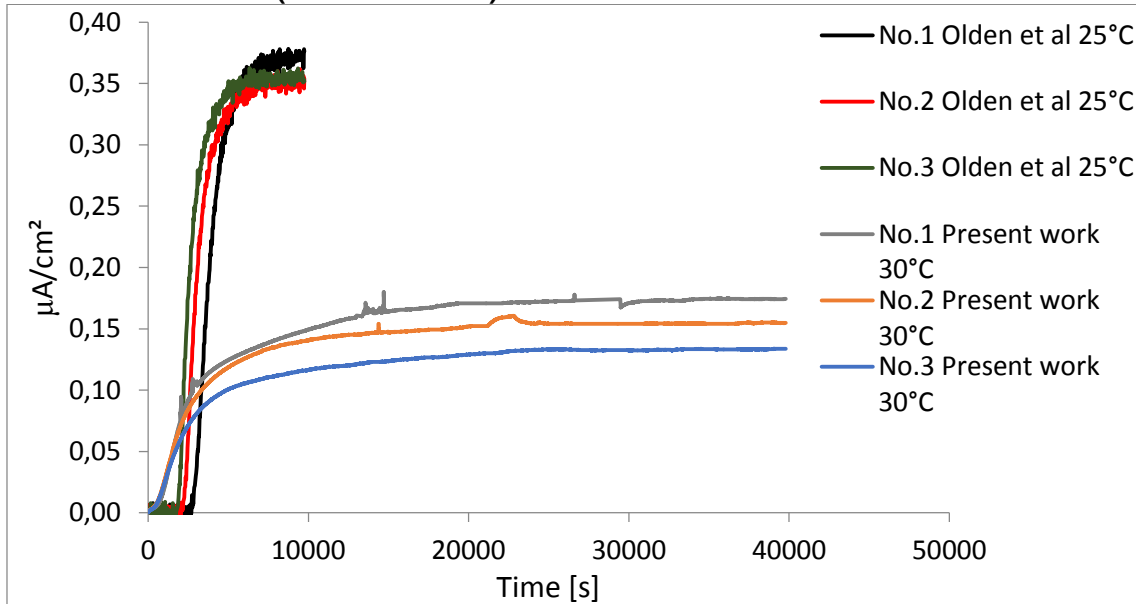Figure B 19: Anodic current density vs. time for X70 BM1 at a temperature of 70˚C-75˚C. The results from present work are from X70 HAZ1 sample.
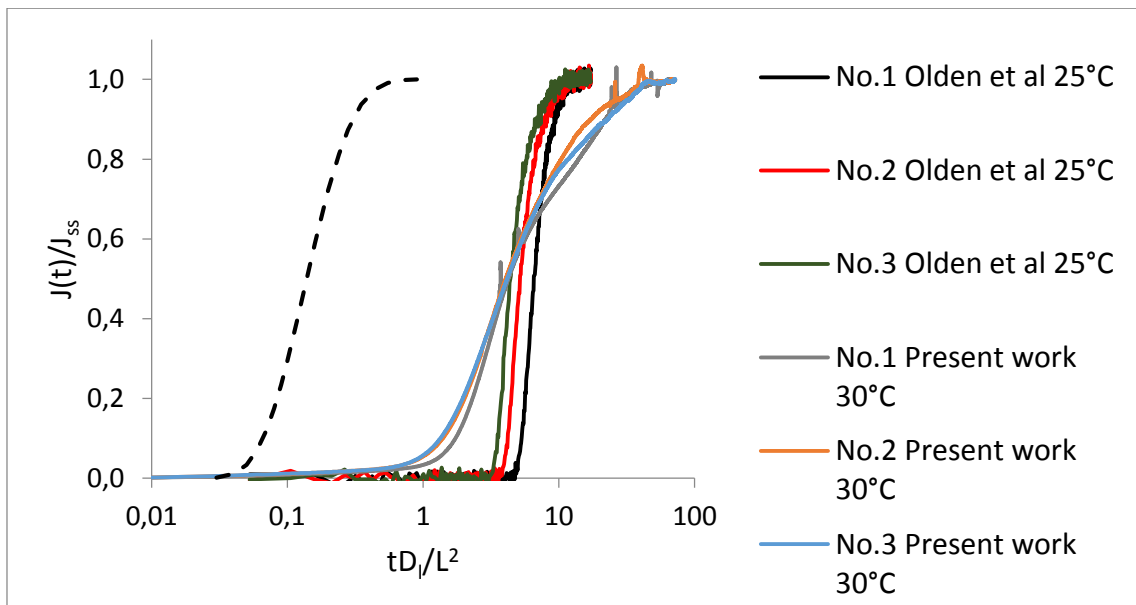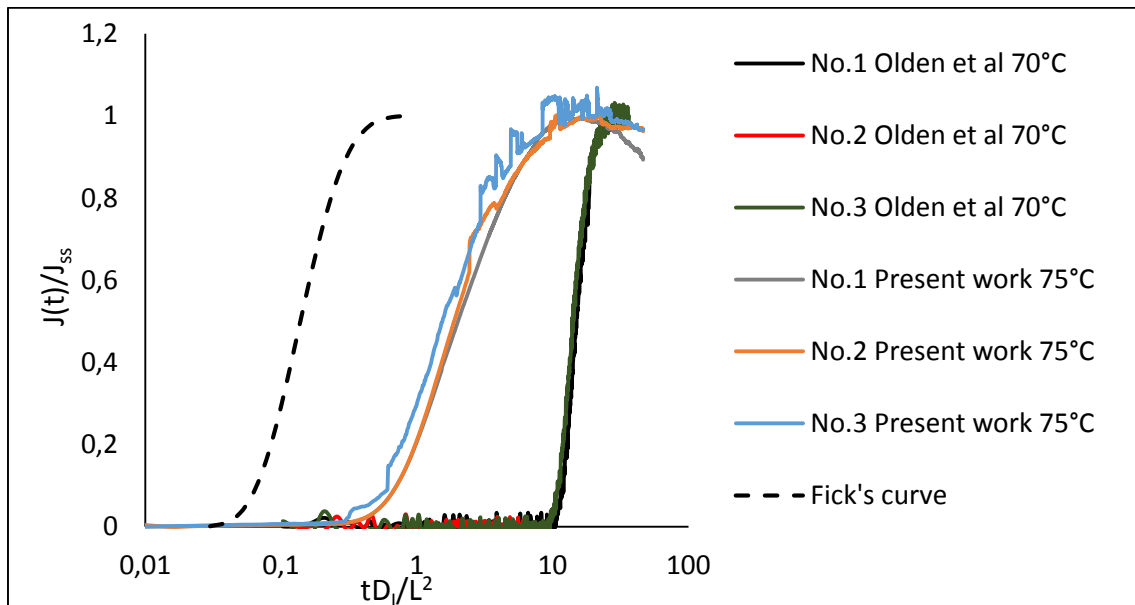

Figure B 20: Normalized permeation flux vs. dimensionless time for X70 HAZ1 at a temperature of 70˚C-75˚C. The results from present work are from X70 HAZ1 sample 1.

B.2.3   BM2 (1%strain)
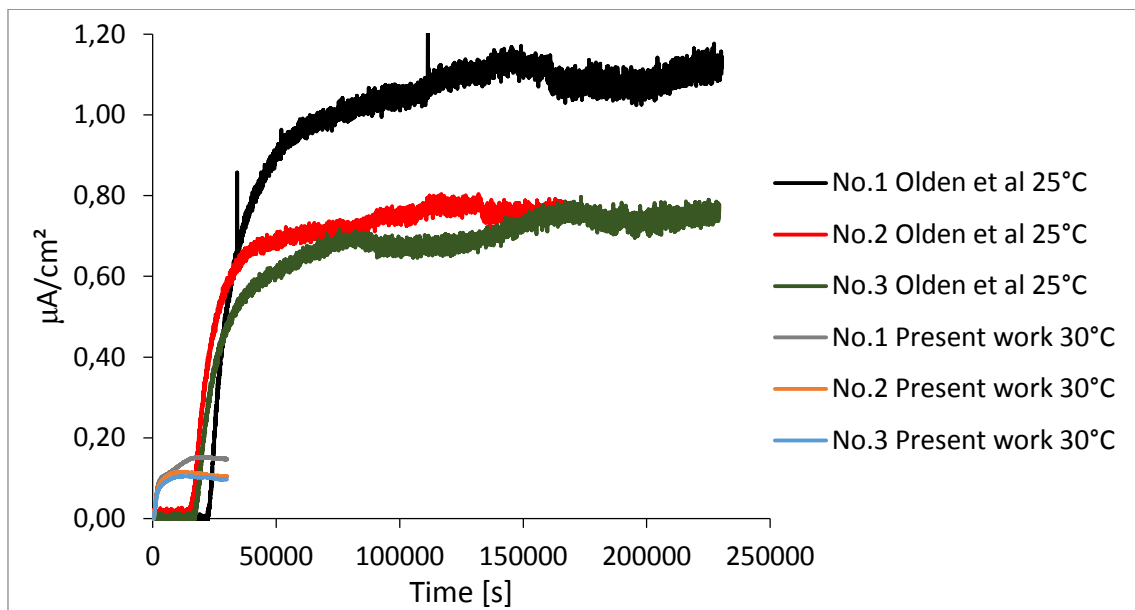
Figure B 21: Anodic current density vs. time for X70 BM2 at a temperature of 25˚C-30˚C.
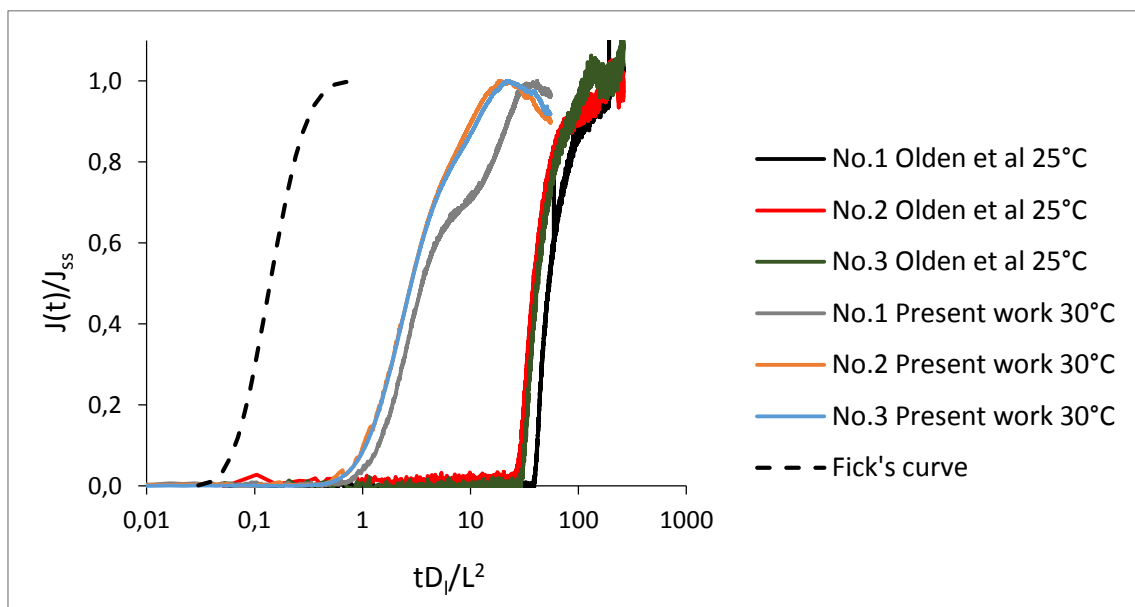
Figure B 22: Normalized permeation flux vs. dimensionless time for X70 BM2 at a temperature of 25˚C-30˚C.

Appendix C

Curve fitting – trapping model

C.1   Typically good fit
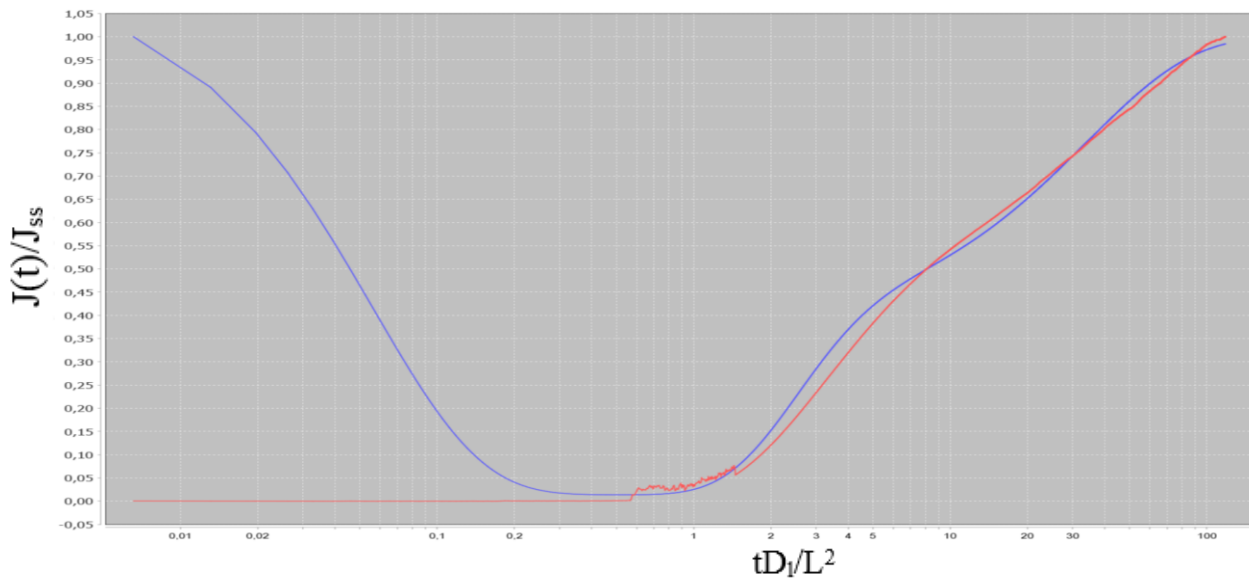
Figure C 1: Good fit of the trapping model to the experimental data. Red line represents the 3rd charging transient for X70 HAZ1, sample 2, at 50°C. The blue line represents the fit of the trapping model. Graph obtained from the software by Simonsen [6].

C.2 Typically poor fit
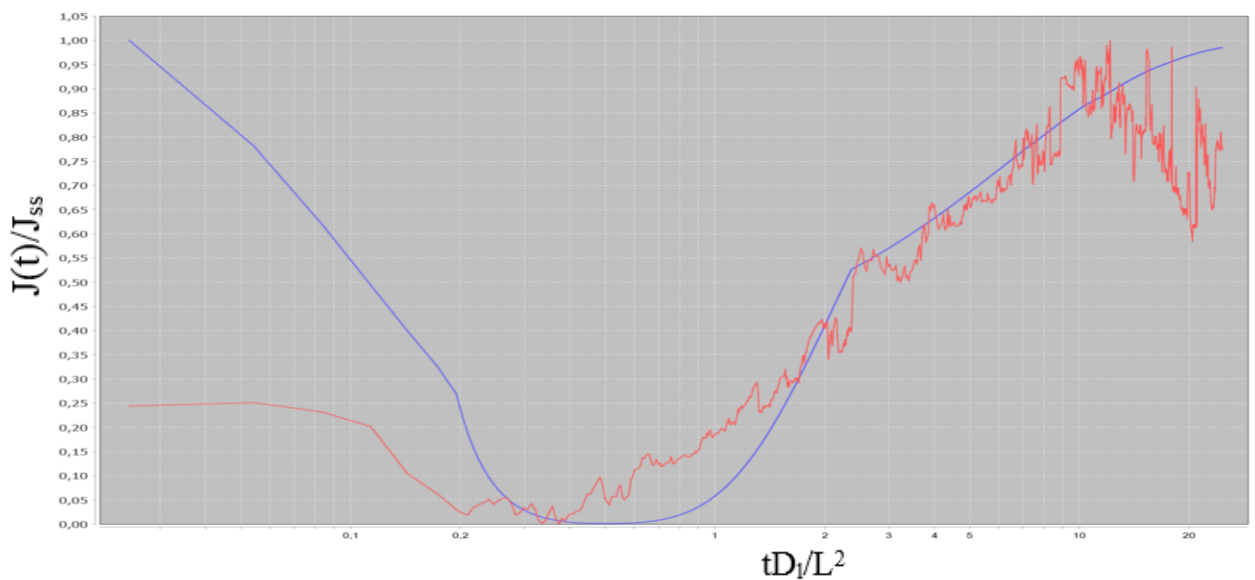
Figure C 2: Poor fit of the trapping model to the experimental data due to filtering away too many data points. Red line represents the 1st partial charging transient for X70 BM1 at 75°C. The blue line represents the fit of the trapping model. Graph obtained from the software by Simonsen [6].

Appendix D

Material certificate X70 high strength steel

DILLINGER HÜTTE

Erläuterungen siehe Rückseite/Explications voir au verso/See reverse for explanations (www.dillinger.de/certificate)

A02	INSPECTION CERTIFICATE 3.1 AS PER EN 10204:2004		A10 Advice of dispatch No./ Date of dispatch	A08/ Manufacturer's order/ A03 Certificate No.	Sheet
	INSPECTION CERTIFICATE 3.1.B AS PER EN 10204:1991+A1:1995 + AS PER ISO 10474:1991		277749-29.10.07	329020-002	1/...

MATERIAL TEST REPORT (MTR)

A05 Established Inspecting body	A06 Purchaser	A07.1 No. FE 4036	B01 Product
DH	EBK, KREUZTAL	A07.2 No. FE 4036	HOT ROLLED PLATES
	Final receiver EBK, KREUZTAL		

B02/ Steel design.	SAWL-485-I-FD
B03 Any suppl. requirements	DNV-OS-F101:00

B01-B99 Description of the product

B14 Item No.	B08 Number of pieces	B09 Thickness MM	B10 Width MM	B11 Length	B12 Theoretical mass KG	B04 Product delivery condition	B07.2 Heat No.	B07.1 Rolled plate No./ Test No.	A09 Purchaser article number
01	1	41,00	x 3761	x 12241	14817	TM	312448	92214-01	EBK-POS.1
01	1	41,00	x 3761	x 12241	14817	TM	312448	92214-02	EBK-POS.1
**	2				29634				
***	2				29634 Actual mass: 30400 KG				

B06 Marking of the product

ITEM NO.: 01
STEEL DESIGNATION SAWL 485 I FD
HEAT NO. / TRADEMARK / ROLLED PLATE NO.-TEST NO. / INSPECTOR'S STAMP
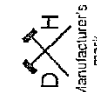
C10-C29 Tensile test

B14 Item No.	B07.2 Heat No.	B07.1 Rol.plate/ Test No.	B05 Reference (heat) treatment	C01	C02/ C01	C03 Temp. GR.C	C10	C11 MPA RT05	C12 RM MPA RT05	C13	A % Lo=5D	C14-C15 RT05/RM
01	312448	92214		K4 L	60	60		485	551		25,7	0,88
				K4 L	RT	RT		519	589		27,6	0,88
				K4 Q	RT	RT		528	606		25,4	0,87

C10-C29 Further information about tensile test

ITEM NO.: 01
HOT TENSILE TEST BY 60 GR. C INFORMATIVE.

A04	Z01/Z02/Z03 We hereby certify, that the above mentioned materials have been delivered in accordance with the terms of order.	AG der Dillinger Hüttenwerke Postfach 1580, D-66748 Dillingen/Saar	AC1
Manufacturer's mark	QM-System: Certification as per ISO 9001	Inspection department	
		B. MUELLER Test House Manager	Inspector's stamp Date 29.10.07 RD 1

Erläuterungen siehe Rückseite/Explications voir au verso/See reverse for explanations (www.dillinger.de/certificate)

⊕ DILLINGER HÜTTE

A02 INSPECTION CERTIFICATE 3.1 AS PER EN 10204:2004	A10 Advice of dispatch No./ Date of dispatch	A06/ Manufacturer's order/ A03 Certificate No.	Sheet
INSPECTION CERTIFICATE 3.1.B AS PER EN 10204:1991+A1:1995 + AS PER ISO 10474:1991	277749-29.10.07	329020-002	2/...
MATERIAL TEST REPORT (MTR)		B01 Product	

A05 Established Inspecting body DH	A06 Purchaser EBK,KREUZTAL	A07.1 No. FE 4036	HOT ROLLED PLATES
	Final receiver EBK,KREUZTAL	A07.2 No. FE 4036	

B02/ Steel design. SAWL-485-I-FD
B03 Any suppl. requirements DNV-OS-F101:00

C30-C39 Hardness test

B14 Item No.	B07.2 Heat No.	B07.1 Rol.plate/ Test No.	B05 Reference (heat) treatment	C01	C02/C01	CO1	C03 Temp. GR.C	C33 Testing method	C35	C31 individual values			C32 Mean value
01	312448	92214		K4	X	1,0	RT	HV10	HV	192	196	194	194
				K4	X	2,0	RT	HV10	HV	191	193	190	191
				K4	X	3,0	RT	HV10	HV	186	184	187	186
				K4	X	4,0	RT	HV10	HV	187	187	188	187
				K4	X	5,0	RT	HV10	HV	185	187	181	184
				K4	X	6,0	RT	HV10	HV	189	187	185	187
				K4	X	7,0	RT	HV10	HV	193	188	182	188
				K4	X	8,0	RT	HV10	HV	186	190	183	186
				K4	X	9,0	RT	HV10	HV	187	189	191	189
				K4	X	10,0	RT	HV10	HV	185	185	186	185
				K4	X	11,0	RT	HV10	HV	188	187	179	185
				K4	X	12,0	RT	HV10	HV	185	187	185	186
				K4	X	13,0	RT	HV10	HV	188	183	181	184
				K4	X	14,0	RT	HV10	HV	183	183	185	184
				K4	X	15,0	RT	HV10	HV	185	185	184	185
				K4	X	16,0	RT	HV10	HV	185	186	186	186
				K4	X	17,0	RT	HV10	HV	186	191	185	187
				K4	X	18,0	RT	HV10	HV	186	192	190	189
				K4	X	19,0	RT	HV10	HV	186	183	182	184
				K4	X	20,0	RT	HV10	HV	175	176	180	177
				K4	X	21,0	RT	HV10	HV	184	187	186	186
				K4	X	22,0	RT	HV10	HV	191	183	187	187
				K4	X	23,0	RT	HV10	HV	180	182	176	179
				K4	X	24,0	RT	HV10	HV	187	184	182	184

QM-System: Certification as per ISO 9001

B. MUELLER
Test House Manager

AG der Dillinger Hüttenwerke
Postfach 1580, D-66748 Dillingen/Saar
Inspection department

Inspector's stamp   Date 29.10.07

RD

A04

Manufacturer's mark

DILLINGER HÜTTE

A02 INSPECTION CERTIFICATE 3.1 AS PER EN 10204:2004	A10 Advice of dispatch No./ Date of dispatch	A08/ Manufacturer's order/ A03 Certificate No.	Sheet
INSPECTION CERTIFICATE 3.1.B AS PER EN 10204:1991+A1:1995 + AS PER ISO 10474:1991	277749-29.10.07	329020-002	3/...

MATERIAL TEST REPORT (MTR)

A05 Established inspecting body	A06 Purchaser		A07.1 No.		B01 Product
DH		EBK,KREUZTAL	FE 4036		HOT ROLLED PLATES
	Final receiver	EBK,KREUZTAL	A07.2 No. FE 4036		

B02/ Steel design. SAWL-485-I-FD
B03 Any suppl. DNV-OS-F101:00
requirements

C30-C39 Hardness test

B14 Item. No.	B07.1 Rol.plate/ Test No.	B07.2 Heat No.	B05 Reference (heat) treatment	C01	C02/C01	C03 Temp. GR.C	C33 Testing method	C35	C31 Individual values			C32 Mean value
01	92214	312448		K4	X	25,0	RT HV10	HV	183	186	187	185
				K4	X	26,0	RT HV10	HV	180	182	183	182
				K4	X	27,0	RT HV10	HV	179	183	184	182
				K4	X	28,0	RT HV10	HV	182	185	184	184
				K4	X	29,0	RT HV10	HV	185	189	183	186
				K4	X	30,0	RT HV10	HV	185	185	185	185
				K4	X	31,0	RT HV10	HV	190	188	187	188
				K4	X	32,0	RT HV10	HV	187	189	193	190
				K4	X	33,0	RT HV10	HV	192	193	193	193
				K4	X	34,0	RT HV10	HV	198	196	196	197
				K4	X	35,0	RT HV10	HV	199	194	191	195
				K4	X	36,0	RT HV10	HV	194	200	198	197
				K4	X	37,0	RT HV10	HV	199	200	201	200
				K4	X	38,0	RT HV10	HV	196	202	205	201
				K4	X	39,0	RT HV10	HV	209	207	209	208
				K4	X	40,0	RT HV10	HV	209	205	203	206
				K4	O		RT HV10	HV	213	206	210	210
				K4	U		RT HV10	HV	211	219	215	215

AG der Dillinger Hüttenwerke
Postfach 1580, D-66748 Dillingen/Saar
Inspection department

Date 29.10.07

B. MUELLER
Test House Manager

Inspector's stamp

A01
RD 1

Manufacturer's mark

DILLINGER HÜTTE

Erläuterungen siehe Rückseite/Explications voir au verso/See reverse for explanations (www.dillinger.de/certificate)

A02		
INSPECTION CERTIFICATE 3.1 AS PER EN 10204:2004		Sheet
INSPECTION CERTIFICATE 3.1.B AS PER EN 10204:1991+A1:1995 + AS PER ISO 10474:1991	A08/ Manufacturer's order/ A03 Certificate No.	4/...
MATERIAL TEST REPORT (MTR)	329020-002	

A10 Advice of dispatch No./ Date of dispatch: 277749-29.10.07

B01 Product: HOT ROLLED PLATES

A05 Established inspecting body	A06 Purchaser	EBK,KREUZTAL	A07.1 No. FE 4036
DH	Final receiver	EBK,KREUZTAL	A07.2 No. FE 4036

B02/ Steel design.: SAWL-485-I-FD

B03 Any suppl. requirements: DNV-OS-F101:00

C40-C49 Impact test

B14 Item No.	B07.2 Heat No.	B07.1 Rol.plate/ Test No.	B05 Reference (heat) treatment	C01	C02/ C01	C03 Temp. GR.C	C41 Width of test piece	C40 Type of test piece	C44 Testing method	C45	C42 Individual values AV=J,DU=%			C43 Mean value	C46 Energy Joule
01	312448	92214		K4	QM	-20		CHP-V		AV	425	426	419	423	600
				K4	QM	-20		CHP-V		DU	100	100	100	100	600
				K4	QM	-40		CHP-V		AV	395	396	356	382	600
				K4	QM	-40		CHP-V		DU	100	100	100	100	600
				K4	QO	-40		CHP-V		AV	366	364	373	368	600
				K4	QO	-40		CHP-V		DU	100	100	100	100	600
				K4	QU	-40		CHP-V		AV	347	351	348	349	600
				K4	QU	-40		CHP-V		DU	100	100	100	100	600
				K4	QM	-20		CHP-V	3,3%-250C-1H	AV	312	210	325	282	600
				K4	QM	-20		CHP-V	3,3%-250C-1H	DU	100	100	100	100	600

C60-C65 BDWT-Test

B14 Item No.	B07.2 Heat No.	B07.1 Rol.plate/ Test No.	B05 Reference (heat) treatment	C01	C02/ C01	C03 Temp. GR.C	C65	C61 Individual values DU=%	C62 Mean value
01	312448	92214		K4	Q	-37	DU	100	100

C66-C68 Supplementary tests on test samples

ITEM NO.: 01

CTOD-TEST CONDUCTED ACC.TO BS-EN-ISO-12737 AT TEMP.= -20 GR.C

B07.2	B07.1	C01/C02	C01	TESTING RESULTS MM:
312448	92214	F4	Q	3,03 2,34 2,10

Z01/Z02/Z03 We hereby certify, that the above mentioned materials have been delivered in accordance with the terms of order.

QM-System: Certification as per ISO 9001

A04 Manufacturer's mark: D×H

AG der Dillinger Hüttenwerke
Postfach 1580, D-66748 Dillingen/Saar
Inspection department

B. MUELLER
Test House Manager

Inspector's stamp

Date 29.10.07

RD 1

DILLINGER HÜTTE

Erläuterungen siehe Rückseite/Explications voir au verso/See reverse for explanations (www.dillinger.de/certificate)

		Sheet
A10 Advice of dispatch No./ Date of dispatch	A08/ Manufacturer's order/ A03 Certificate No.	6/...
277749-29.10.07	329020-002	
	B01 Product HOT ROLLED PLATES	

A02 INSPECTION CERTIFICATE 3.1 AS PER EN 10204:2004
INSPECTION CERTIFICATE 3.1.B AS PER EN 10204:1991+A1:1995 + AS PER ISO 10474:1991
MATERIAL TEST REPORT (MTR)

A05 Established inspecting body: DH
A06 Purchaser: EBK,KREUZTAL A07.1 No. FE 4036
Final receiver: EBK,KREUZTAL A07.2 No. FE 4036

B02/ Steel design.: SAWL-485-I-FD
B03 Any suppl. requirements: DNV-OS-F101:00

C70-C99 Chemical composition % - Product analysis

B07.2 Heat	Test No.		C	SI	MN	P	S	N	CU	MO	NI	CR	V	NB	AS	SN
312448	92213	K4	0,047	0,098	1,74	0,008	0,0007	0,0025	0,215	0,042	0,243	0,047	0,001	0,027	0,001	0,001
312448	92214	K4	0,047	0,108	1,74	0,010	0,0005	0,0027	0,210	0,048	0,234	0,062	0,000	0,027	0,002	0,000

B07.2 Heat	Test No.		TI	PB	B	SB	CA	BI	AL-T
312448	92213	K4	0,010	0,000	0,0000	0,0000	0,0010	0,0001	0,031
312448	92214	K4	0,009	0,000	0,0001	0,0000	0,0011	0,0001	0,036

C94 Product analysis Carbon equivalent / Alloying restrictions

B07.2 Heat	Test No.		FO-A1	FO-02	FO-20	FO-31	FO-52
312448	92213	K4	FO-A1= 12,4	FO-02= 0,39	FO-20= 0,40	FO-31= 0,16	FO-52= 0,04
312448	92214	K4	FO-A1= 13,3	FO-02= 0,39	FO-20= 0,40	FO-31= 0,16	FO-52= 0,04

C94 Carbon equivalent formula / Alloying restrictions

FO-A1 = AT/N
FO-02 = C+(MN/6)+(CR+MO+V)/5+(NI+CU)/15
FO-20 = C+(MN/5)
FO-31 = C+SI/30+(MN+CR+CU)/20+MO/15+V/10+NI/60+5B
FO-52 = V +NB+TI

D01 Marking and identification, surface appearance, shape and dimensional properties

ITEM NO.: 01
RESULT OF MARKING, SURFACE, SHAPE AND DIMENSIONS: NO REMARKS
SURFACE   AS PER EN-10163-B2
THICKNESS   AS PER CLIENT'S P.O.
LENGTH AND WIDTH   AS PER QST-VV141:REV.3-ROHR

Z01/Z02/Z03 We hereby certify, that the above mentioned materials have been delivered in accordance with the terms of order.

QM-System: Certification as per ISO 9001

B. MUELLER
Test House Manager
Inspector's stamp

AG der Dillinger Hüttenwerke
Postfach 1580, D-66748 Dillingen/Saar
Inspection department
Date 29.10.07

RD 1

120

DILLINGER HÜTTE

Erläuterungen siehe Rückseite/Explications voir au verso/See reverse for explanations (www.dillinger.de/certificate)

A02	INSPECTION CERTIFICATE 3.1 AS PER EN 10204:2004		A10 Advice of dispatch No./ Date of dispatch	A08/ Manufacturer's order/ A03 Certificate No	Sheet

INSPECTION CERTIFICATE 3.1.B AS PER EN 10204:1991+A1:1995 + AS PER ISO 10474:1991

MATERIAL TEST REPORT (MTR)

| | | | | 277749-29.10.07 | 329020-002 | 5/... |

A05 Established inspecting body	A06 Purchaser	EBK, KREUZTAL	A07.1 No.	FE 4036	B01 Product
DH	Final receiver	EBK, KREUZTAL	A07.2 No.	FE 4036	HOT ROLLED PLATES

B02/ Steel design. **SAWL-485-I-FD**

B03 Any suppl. requirements   DNV-OS-F101:00

──── C66-C68 Supplementary tests on test samples ────

ITEM NO.: 01

FERRITE GRAIN SIZE ASTM-E112:

B07.2	B07.1	C01/C02	FKG
310415	24036	K4 L	12
312448	92214	K4 L	11

──── C70-C99 Chemical composition % - Heat analysis ────

B07.2 Heat	C70	C	SI	MN	P	S	N	CU	MO	NI	CR	V	NB	AS	SN
312448	Y	0,048	0,101	1,74	0,009	0,0006	0,0033	0,216	0,042	0,245	0,049	0,000	0,029	0,001	0,000

B07.2 Heat	C70	TI	PB	B	SB	CA	BI	AL-T
312448	Y	0,010	0,000	0,0002	0,0000	0,0007	0,0001	0,032

──── C94 Heat analysis Carbon equivalent / Alloying restrictions ────

B07.2 Heat								
312448	FO-Al= 9,7	FO-02=	FO-20= 0,39	FO-02=	FO-31= 0,40	FO-20=	FO-52= 0,16	FO-52= 0,04

──── C95 Ladle treatment ────

ITEM NO.: 01

HEAT OF THE INDICATED ITEM: VACUUM DEGASSED

──── C95 Further information about ladle treatment ────

ITEM NO.: 01

FULLY KILLED AND MADE TO FINE GRAIN PRACTICE

A04	Z01/Z02/Z03 We hereby certify, that the above mentioned materials have been delivered in accordance with the terms of order.		AG der Dillinger Hüttenwerke Postfach 1580, D-66748 Dillingen/Saar	A01
Manufacturer's mark	QM-System: Certification as per ISO 9001		Inspection department	
		B. MUELLER Test House Manager	Inspector's stamp Date 29.10.07	RD 1

Appendix E

Risk assessment

NTNU | HMS

Kartlegging av risikofylt aktivitet

	Utarbeidet av	Nummer	Dato
	HMS-avd.	HMSRV2601	22.03.2011
	Godkjent av		Erstatter
	Rektor		01.12.2006

Enhet:

Linjeleder:

Deltakere ved kartleggingen (m/ funksjon): **Malin S.B. Hope, Afrooz Barnoush, Roy Johnsen, Vigdis Olden**
(Ansv. veileder, student, evt. medveiledere, evt. andre m. kompetanse)

Kort beskrivelse av hovedaktivitet/hovedprosess: Masteroppgave for Malin Sofie Berglund Hope – Effect of plastic deformation and microstructure on hydrogen diffusion in steel

Er oppgaven rent teoretisk? (JA/NEI): **NEI**   «JA» betyr at veileder innestår for at oppgaven ikke inneholder noen aktiviteter som krever risikovurdering. Dersom «JA»: Beskriv kort aktiviteten i kartleggingskjemaet under. Risikovurdering trenger ikke å fylles ut.

Signaturer: Ansvarlig veileder: Student:

Dato: 19.01.15

ID nr.	Aktivitet/prosess	Ansvarlig	Eksisterende dokumentasjon	Eksisterende sikringstiltak	Lov, forskrift o.l.	Kommentar
	Lage/blande elektrolytt (glycerin+borax+vann)			Verneutstyr Opplæring Avtrekksskap		
	Mekanisk sliping og polering			Verneutstyr Opplæring		
	Rigge testoppsett for diffusjonstest			Verneutstyr		
	Gjennomføre diffusjonstest i vannbad (varierer temperaturen i vannbadet for de ulike testene)			Verneutstyr		
	Rigge ned utstyr etter diffusjonstest			Verneutstyr		

NTNU

HMS

	Utarbeidet av	Nummer	Dato
	HMS-avd.	HMSRV2601	22.03.2011
	Godkjent av		Erstatter
	Rektor		01.12.2006

Risikovurdering

Enhet: **Dato: 19.01.15**

Linjeleder:

Deltakere ved kartleggingen (m/ funksjon): Malin S.B. Hope, Afrooz Barnoush, Roy Johnsen, Vigdis Olden
(Ansv. Veileder, student, evt. medveiledere, evt. andre m. kompetanse)

Risikovurderingen gjelder hovedaktivitet: Masteroppgave for Malin Sofie Berglund Hope – Effect of plastic deformation and microstructure on hydrogen diffusion in steel

Signaturer: *Ansvarlig veileder:*   *Student:*

ID nr	Aktivitet fra kartleggings-skjemaet	Mulig uønsket hendelse/ belastning	Vurdering av sannsyn-lighet (1-5)	Vurdering av konsekvens:				Risiko-Verdi (menn-eske)	Kommentarer/status Forslag til tiltak
				Menneske (A-E)	Ytre miljø (A-E)	Øk/ materiell (A-E)	Om-dømme (A-E)		
	Lage/blande elektrolytt (glycerin+borax+vann)								
	Mekanisk sliping og polering	Overflatesår på hendene	4	A				A4	Bruke verneutstyr, hansker spesielt viktig
	Rigge testoppsett for diffusjonstest	Overflatesår etter skarpe gjenstander etc	2	A				A2	Bruke verneutstyr
	Gjennomføre diffusjonstest i vannbad (varierer temperaturen i vannbadet for de ulike testene)	Brannskader pga høy temperatur i vannbad/elektrolytt (rett under elektrolyttens kokepunkt)	3	A				A3	Bruke verneutstyr
	Rigge ned utstyr etter diffusjonstest	Overflatesår etter skarpe gjenstander etc	2	A				A2	Bruke verneutstyr

NTNU	Risikovurdering	Utarbeidet av	Nummer	Dato
HMS		HMS-avd.	HMSRV2601	22.03.2011
		Godkjent av		Erstatter
		Rektor		01.12.2006

Sannsynlighet vurderes etter følgende kriterier:

Svært liten 1	Liten 2	Middels 3	Stor 4	Svært stor 5
1 gang pr 50 år eller sjeldnere	1 gang pr 10 år eller sjeldnere	1 gang pr år eller sjeldnere	1 gang pr måned eller sjeldnere	Skjer ukentlig

Konsekvens vurderes etter følgende kriterier:

Gradering	Menneske	Ytre miljø Vann, jord og luft	Øk/materiell	Omdømme
E Svært Alvorlig	Død	Svært langvarig og ikke reversibel skade	Drifts- eller aktivitetsstans >1 år.	Troverdighet og respekt betydelig og varig svekket
D Alvorlig	Alvorlig personskade. Mulig uførhet.	Langvarig skade. Lang restitusjonstid	Driftsstans > ½ år Aktivitetsstans i opp til 1 år	Troverdighet og respekt betydelig svekket
C Moderat	Alvorlig personskade.	Mindre skade og lang restitusjonstid	Drifts- eller aktivitetsstans < 1 mnd	Troverdighet og respekt svekket
B Liten	Skade som krever medisinsk behandling	Mindre skade og kort restitusjonstid	Drifts- eller aktivitetsstans < 1uke	Negativ påvirkning på troverdighet og respekt
A Svært liten	Skade som krever førstehjelp	Ubetydelig skade og kort restitusjonstid	Drifts- eller aktivitetsstans < 1dag	Liten påvirkning på troverdighet og respekt

Risikoverdi = Sannsynlighet x Konsekvens
Beregn risikoverdi for Menneske. Enheten vurderer selv om de i tillegg vil beregne risikoverdi for Ytre miljø, Økonomi/materiell og Omdømme. I så fall beregnes disse hver for seg.

Til kolonnen "Kommentarer/status, forslag til forebyggende og korrigerende tiltak":
Tiltak kan påvirke både sannsynlighet og konsekvens. Prioriter tiltak som kan forhindre at hendelsen inntreffer, dvs. sannsynlighetsreduserende tiltak foran skjerpet beredskap, dvs. konsekvensreduserende tiltak.

124

NTNU		utarbeidet av	Nummer	Dato	
	Risikomatrise	HMS-avd.	HMSRV2604	08.03.2010	
HMS/KS		godkjent av		Erstatter	
		Rektor		09.02.2010	

MATRISE FOR RISIKOVURDERINGER ved NTNU

KONSEKVENS						
Svært alvorlig	E1	E2	E3	E4	E5	
Alvorlig	D1	D2	D3	D4	D5	
Moderat	C1	C2	C3	C4	C5	
Liten	B1	B2	B3	B4	B5	
Svært liten	A1	A2	A3	A4	A5	
	Svært liten	Liten	Middels	Stor	Svært stor	
			SANNSYNLIGHET			

Prinsipp over akseptkriterium. Forklaring av fargene som er brukt i risikomatrisen.

Farge		Beskrivelse
Rød		Uakseptabel risiko. Tiltak skal gjennomføres for å redusere risikoen.
Gul		Vurderingsområde. Tiltak skal vurderes.
Grønn		Akseptabel risiko. Tiltak kan vurderes ut fra andre hensyn.